Computer simulations of two-dimensional colloidal crystals under confinement and shear

DISSERTATION

FACHBEREICH 08
(INSTITUT FÜR PHYSIK)
JOHANNES GUTENBERG–UNIVERSITÄT
MAINZ

Dorothea Wilms

Mainz, 2. Oktober 2012

Datum der mündlichen Prüfung: 09.01.2013

Computer simulation studies of two-dimensional colloidal crystals under confinement and shear

In this thesis we are presenting a broadly based computer simulation study of two-dimensional colloidal crystals under different external conditions. In order to fully understand the phenomena which occur when the system is being compressed or when the walls are being sheared, it proved necessary to study also the basic motion of the particles and the diffusion processes which occur in the case without these external forces.

In the first part of this thesis we investigate the structural transition in the number of rows which occurs when the crystal is being compressed by placing the structured walls closer together. Previous attempts to locate this transition were impeded by huge hysteresis effects. We were able to determine the transition point with higher precision by applying both the Schmid-Schilling thermodynamic integration method and the phase switch Monte Carlo method in order to determine the free energies. These simulations showed not only that the phase switch method can successfully be applied to systems with a few thousand particles and a soft crystalline structure with a superimposed pattern of defects, but also that this method is way more efficient than a thermodynamic integration when free energy differences are to be calculated. Additionally, the phase switch method enabled us to distinguish between several energetically very similar structures and to determine which one of them was actually stable. Another aspect considered in the first result chapter of this thesis is the ensemble inequivalence which can be observed when the structural transition is studied in the NpT and in the NVT ensemble.

The second part of this work deals with the basic motion occurring in colloidal crystals confined by structured walls. Several cases are compared where the walls are placed in different positions, thereby introducing an incommensurability into the crystalline structure. Also the movement of the solitons, which are created in the course of the structural transition, is investigated. Furthermore, we will present results showing that not only the well-known mechanism of vacancies and interstitial particles leads to diffusion in our model system, but that also cooperative ring rotation phenomena occur. In this part and the following we applied Langevin dynamics simulations.

In the last chapter of this work we will present results on the effect of shear on the colloidal crystal. The shear was implemented by moving the walls with constant velocity. We have observed shear banding and, depending on the shear velocity, that the inner part of the crystal breaks into several domains with different orientations. At very high shear velocities holes are created in the structure, which originate close to the walls, but also diffuse into the inner part of the crystal.

Computersimulationen eines zweidimensionalen Kolloidkristalls in beschränkter Geometrie und unter Scherung

In dieser Dissertation stellen wir die Ergebnisse von Computersimulationen zweidimensionaler Kolloidkristalle unter verschiedenen äusseren Bedingungen vor. Um die Phänomene voll und ganz zu verstehen, die auftreten, wenn dieses System komprimiert wird oder wenn die implementierten Wände geschert werden, ist es notwendig, zunächst die Teilchenbewegungen und Diffusionsprozesse zu untersuchen, die im Fall ohne solche äusseren Einflüsse auftreten.

Im ersten Teil dieser Doktorarbeit untersuchen wir den strukturellen Übergang in der Anzahl der Kristallreihen, der auftritt, wenn man den Kristall komprimiert, indem man die strukturierten Wände näher zusammen rückt. In früheren Untersuchungen an diesem Modellsystem konnte der Übergangspunkt aufgrund von ausgeprägten Hystereseeffekten nicht genau bestimmt werden. Uns war es möglich, ihn exakt zu bestimmen, indem wir sowohl die Schmid-Schilling-Methode der thermodynamischen Integration als auch die Phase-Switch-Monte-Carlo-Methode angewendet und mit ihnen die freien Energien bestimmt haben. Unsere Simulationen haben nicht nur gezeigt, dass die Phase-Switch-Methode erfolgreich auf Systeme aus mehreren tausend Teilchen mit einer weichen Kristallstruktur und einem damit überlagerten Defektmuster angewendet werden kann, sondern auch, dass diese Methode deutlich effizienter ist als eine thermodynamische Integration, wenn Differenzen in der freien Energie bestimmt werden sollen. Darüberhinaus kann man mit Hilfe der Phase-Switch-Methode mehrere energetisch nah beieinander liegende Strukturen unterscheiden und bestimmen, welche von ihnen stabil ist. Ein anderer Aspekt, der im ersten Ergebniskapitel dieser Dissertation behandelt wird, ist die Nicht-Gleichwertigkeit verschiedener Ensembles, die bei diesem strukturellen Übergang beobachtet werden kann.

Der zweite Teil dieser Arbeit beschäftigt sich mit den grundlegenden Teilchenbewegungen in Kolloidkristallen, die von strukturierten Wänden begrenzt werden. Mehrere Fälle werden verglichen, bei denen die Wände in verschiedenen Abständen voneinander eingesetzt sind und dadurch teilweise die Kristallstruktur komprimieren. Auch die Bewegung der Solitonen, die im Zuge des strukturellen Übergangs entstehen, wird untersucht. Darüberhinaus präsentieren wir Ergebnisse, die beweisen, dass nicht nur der bekannte Mechanismus, der auf dem Auftreten von Löchern und Teilchen an Zwischengitterplätzen beruht, zur Diffusion in unserem Modellsystem beiträgt, sondern dass auch kooperative Rotationsphänomene auftreten. In diesem und dem nachfolgenden Teil der Arbeit wurden Langevindynamiksimulationen durchgeführt.

Im letzten Teil dieser Arbeit untersuchen wir den Einfluss von Scherung auf Kolloidkristalle. Die Scherung wurde implementiert, indem die strukturierten Wände mit konstanter Geschwindigkeit bewegt wurden. Dies führt zum Auftreten von Scherungsbändern und, in Abhängigkeit von der Schergeschwindigkeit, dazu, dass der innere Teil des Kristalls in mehrere Domänen unterschiedlicher Ausrichtung zerbricht. Bei sehr hohen Schergeschwindigkeiten treten Löcher in der Struktur auf, die sich an den Wänden bilden und ins Innere des Kristalls diffundieren.

Contents

Introduction

In this thesis we are going to present results of computer simulation studies of a colloidal crystal. Colloids are omnipresent as the word "colloid" refers to any dispersion of small particles in a solvent. Typically, these small particles are of a size between several nanometres and several micrometers, while the solvent particles are significantly smaller. Well-known examples of colloidal dispersions include milk, ketchup and blood, where the solvent is in a liquid state. But in addition, dispersions of solid particles or liquid drops in a gas (like hairsprays) and dispersions of a liquid within a solid (gels) can also be referred to as colloids.

Colloidal crystals are usually composed of solid particles in a liquid solution. These solid particles form a crystalline lattice with long-ranged order analogous to atoms or molecules in regular crystals. A prominent example of such a solid is the gem opal which forms in highly siliceous pools by sedimentation of silicon dioxide SiO_2 and under the influence of hydrostatic pressure. But also electrically charged macromolecules in water suspensions can form colloidal crystals due to their repulsive interaction. In experiments, however, usually monodisperse spherical (or differently shaped) particles are used which are tailored to the needs of the planned investigation. These particles can, for example, contain iron-oxide which leads to a magnetic repulsion between these particles once an external magnetic field is switched on. These repulsive particles can then form a colloidal crystal.

"Real" colloidal crystals (as opposed to the idealized ones used in computer simulations) are interesting as they often form areas of interstitials between purely crystalline areas which leads to periodically repeating areas of high and low dielectric constant, thus forming a photonic crystal. This repetition of different areas allows only certain wavelengths of electromagnetic waves to propagate through them, while other wavelengths are reflected as they cannot enter the crystal. These "forbidden" wavelengths are termed "photonic band gap" by analogy with the electronic band gap observed in semiconductors. This leads to interesting phenomena like the inhibition of spontaneous emission and also makes them useful for highly reflective mirrors and low-loss-waveguiding.

But colloidal dispersions and crystals are also very interesting as model systems with which phenomena like self-assembly, (structural) phase transitions, kinetics of crystallization and other condensed matter topics can be investigated, because the structures formed by colloidal particles resemble "real" liquids and solids. Thus they play an important role in the thriving field of material science.

Another feature which makes colloids interesting for physicists and chemists is the fact that colloids are easily accessible in experiments. They can be manufactured from both polymers and minerals by either dissolving larger particles in an appropriate solution until the particle size reaches the proper size of colloidal particles or by aggregation of smaller molecules into properly-sized colloids. Depending on the size of the colloidal particles, confocal miscroscopy provides a resolution which can be high enough to track single particles inside the colloidal dispersion. Due to the many possibilities of producing colloidal particles out of different materials, the possible interaction potential of these particles are also manyfold and can be taylored to the needs of the experiment.

Tracking particles in colloidal dispersions or crystals is especially easily feasible if only two-dimensional layers of particles are studied. In this thesis we will also focus on studies of a two-dimensional colloidal crystal. Of course, in principle there are no crystals in two dimensions as long-wave thermal fluctuations destroy the translational order. This is not the case for three-dimensional crystals, because due to the higher dimensionality the energy required to destroy the long-range order inside of the crystal increases with the size of the crystal, while it remains finite in the case of two-dimensional crystals. Nevertheless, the disorder due to long-wave thermal fluctuations only plays a role for very large two-dimensional crystals which we are not going to study here. Additionally, the crystalline structure is stabilized in our simulations by walls in one direction which consist of frozen particles arranged in a crystalline order.

Although colloids have been extensively studied over the past decades, there are still many interesting aspects even in the area of fundamental research that have not yet been investigated. This PhD thesis was carried out in the framework of the Sonderforschungsbereich Transregio (SFB TR6) "Colloidal dispersions in external fields" (CODEF), which was founded by the Universities of Utrecht, Düsseldorf, Konstanz and Mainz and the Forschungszentrum Jülich in 2005, funded by the Deutsche Forschungsgemeinschaft (DFG). It aims at a widespread investigation of phenomena occurring when colloids are exposed to all kinds of external conditions like for example laser fields, shearing or restrictions of the particles' movement imposed by walls. It has been prolonged twice, which shows not only the great success of the efforts undertaken in this SFB, but also reflects on the importance of studying colloidal particles.

This thesis consists of three parts, all of them dealing with computer simulations of a two-dimensional colloidal crystal under confinement. Over the past decades, computer simulations have gained more and more importance not only in physics, but everywhere in science, industry and finance. They are an essential addition to experiment and theory, especially in areas where experiments are impossible (finance) or very expensive, dangerous and/or time-consuming (science and industry) and where theories exist only for simplified cases or even not at all (industry, e.g. invention of novel materials).

In classical statistical physics, two general methods of computer simulations have been developed. The Molecular Dynamics (MD) method aims at simulating systems by calculating the forces acting between particles (or, in coarse-grained simulations, between groups of atoms represented by one effective particle) and solving Newton's equation of motion in order to obtain the velocities of the particles. Thus, the trajectories of the particles through the system can be simulated.

A different approach is taken by the Monte Carlo (MC) simulation method. This technique does not aim at calculating the realistic path which particles would take in a given system, but instead tries to sample the most important configurations of the particles in a given system by making random attempts at placing particles in the system (or moving them around) and accepting or rejecting the hereby created configurations according to their statistical weight. Due to the ergodic hypothesis, the two simulation methods yield the same results for the statistical averages calculated for observables. While MC simulations are necessary for calculating high-dimensional integrals and can also be used to model Brownian motion, MD simulations are indispensable when the dynamics of a system are being studied. Different variants of the two methods have been used in this thesis. One version of MD simulations which we have used for the present studies is described in Sec. 1.3, two different versions of MC simulations are described in Sec. 2.1 and 2.3.

An advantage of the simulation of colloidal systems is the fact that the colloidal particles are several orders of magnitude larger than the solvent particles, which allows us to simulate only the larger colloidal particles explicitly and to reduce the effect of the solvent to stochastic kicks as is done in Langevin dynamic simulations, which are one variant of MD simulations. Of course, this is a very simplified approach and might dampen or enhance some effects. But it is also impossible to simulate the solvent particles explicitly by simply adding them to the standard molecular dynamics simulation as additional particles interacting with each other and with the colloidal particles as this would exceed the amount of CPU time available to us. Therefore, the only alternative to implicit solvent are more sophisticated methods which integrate the motion of the solvent particles approximately and model their effect on the colloidal particles. But as we are rather interested in the qualitative behaviour of the system

and the phenomena occurring here, we leave such more complicated approaches for future work.

The first part of this thesis investigates the static properties of a two-dimensional colloidal crystal, which is compressed between structured walls in one direction. These confining walls consist of frozen particles. The second part deals with dynamic properties of the particle motion and diffusion inside the crystal, while in the last part shear is introduced into the system.

As a first step, the structured walls confining the system have been placed at various distances apart from each other, thereby becoming incommensurate with the crystalline structure and compressing the crystal. This incommensurability is termed "misfit" here. Earlier work by Chui et al [1–3] on this system has already shown that at a certain value of the misfit a structural transition (reducing the number of rows in the crystal) takes place and a defect pattern –which is superimposed onto the crystalline lattice structure– is created, but with the methods used there, the value of this transition point could not be determined accurately. Therefore, we will present results of two different methods with which we have determined this value with high precision and additionally the value of another structural transition occurring at even higher values of the misfit. These two methods, the Schmid-Schilling-method [4, 5] and the phase switch method [6–12], are both based on MC simulations. The phase switch method has been extended to larger and more complex systems here. The results of these two methods show a good agreement with each other, but the phase switch method proved to be considerably better suited for our problem. With this method, we were able to compare several metastable states of the colloidal crystal with different defect superstructures and determine which of them is stable and which are only metastable. We are hoping that our, albeit very basic, studies might be useful for the invention of novel materials, where a prediction of the stability of structures in question might lead to more successful experiments.

Our simulations with the phase switch method have also yielded another result which is interesting in the context of fundamental statistical physics: we discovered that for this particular system the ensemble equivalence between simulations carried out at constant pressure (NPT ensemble) and simulations carried out at constant volume (NVT ensemble) is violated. This is due to the specific nature of the structural phase transition which alters the number of rows: in this particular system, at every given volume only one phase is stable, either the one with n crystalline rows or the one with $n - 1$ rows and a superimposed defect pattern. There is no two-phase region where it is energetically preferrable for the system to exhibit partly one and partly the other phase and an interface between them. This is the case because at every value of the wall distance, one of the two possible particle arrangements is energetically favourable and it does not get any better if in other parts of the crystal the

other arrangement is taken on. This is fundamentally different from, for example, the liquid-vapour transition where at a density between the equilibrium densities of the liquid and the vapour it is energetically preferrable for the system to exhibit partly a vapour and partly a liquid, each at its own equilibrium (or almost equilibrium) densities, so that the combination of the two fulfills the constraints of the given volume and the given overall number of particles.

If one investigates the structural transition in this particular system in the NVT ensemble, increasing the misfit between the walls leads to an increasing pressure at first. As there is no two-phase region, there will not be any transition pressure which remains constant during a scan through this two-phase region, but instead, at the transition point the pressure will instantaneously drop to a smaller value when the system rearranges itself into $n-1$ rows. Increasing the misfit between the walls even more will lead to a further increase in the pressure, which is the "usual" behaviour again.

If one studies the same transition in the NpT ensemble, the simulation can jump back and forth between the two phases with different volumes at each given value of the pressure. At small values of the pressure, only the phase with n rows will be stable, but close to the transition pressure, which is well defined in this ensemble, both phases will exist with different (or exactly at the transition pressure: equal) statistical weights. This situation corresponds to a two-phase region in the NVT ensemble, which does not exist for this system. Further increase of the pressure will lead to a further reduction of the volume again, of course.

Such ensemble inequivalences are very interesting from the point of view of general statistical physics as they contradict intuition. Neither of the two ensembles is "incorrect" in this context, they simply correspond to different physical situations. We have mostly concentrated on the NVT ensemble as we were interested in the case where the walls are fixed (as is feasible, for example, by applying laser fields). The NpT ensemble corresponds to situations where the pressure is controlled, like for example in a surface force apparatus.

In the context of computer simulations it has become popular recently to use graphic cards instead of CPUs as processing units. Their advantage is that they can carry out the same arithmetic operation on many different data points (i.e. on all particle coordinates) in parallel, which can lead to a huge speed up of simulations. One drawback, however, is the fact that consumer graphic cards typically use single precision for their calculations. We therefore used a molecular dynamic simulations programme package called "HooMD-blue" [13, 14] for the investigation of the dynamic properties of the system which are described in the second and third part of this thesis. This programme package has the ability to run on graphic cards, but we

had to carry out most of our simulations on regular CPUs due to the lack of precision on GPUs. There are programme packages available which carry out simulations on graphic cards with higher precision by using the memory of two single precision numbers in order to build larger memory units that are similar to double precision [15, 16], but unfortunately these programme packages do not provide those particular options yet which we need for our simulations. Additionally, new graphic cards often support double precision calculations already, but these graphic cards are still rather expensive.

The second part of this thesis comprises a thorough investigation of the particle motion and diffusion processes occurring inside of two-dimensional colloidal crystals and was carried out using HooMD-blue. Although colloidal crystals in confinement have been extensively studied over the past years, a systematic study of the movement of the particles (and the solitons) in dependency of the confining walls was still missing. We are trying to fill in this gap. Same applies to the diffusion processes inside of colloidal crystals, where our findings were even more surprising: While the well-known theory of diffusion in crystals states that diffusion takes place via the formation of a hole and a corresponding interstitial particle, which both diffuse through the crystal before recombining again, we found that additionally cooperative ring rotation movements of groups of particles appeared, which contribute to the diffusion as well.

Interestingly, in the beginning of the research on diffusion in the 1930s and 1940s different diffusion mechanisms were discussed [17, 18] and the idea of diffusion being carried out by groups of particles making cooperative rotations and even direct exchange between two particles was very popular. However, the Kirkendall experiment showed that when a block of a pure metal and a block of an alloy containing this metal are placed next to each other and heated to temperatures where diffusion can easily take place, the interface between the blocks moves into the region where formerly the pure metal was [19]. After much discussion at that time, this was generally accepted as a proof for a diffusion mechanism which involves holes and/or interstitial particles and which exist in a greater number in one of the two blocks, leading to the moving interface. If diffusion had taken place mostly by rotation processes, the interface would not have moved in such an asymmetric way. Since there has been no experimental evidence for other diffusion mechanisms, the general belief is that cooperative rotation processes play no important role (or do not even exist) in diffusion processes in three-dimensional crystals [20–22].

It is known that cooperative diffusion processes occur in glassy materials [23]. They have also been reported for two-dimensional interfaces [24] and in a layer of crystalline atoms in a periodic potential [25]. However, both of these studies report that the cooperative ring rotation processes were rare events in those simulations. In

contrast to this, in our simulations of a two-dimensional colloidal crystal these cooperative diffusion processes were not rare at all. They occured significantly more often than diffusion events mediated by holes and interstitials. In spite of this, they contributed less to the diffusion constant as there were only a few particles involved in each of the ring rotation processes, while between a few hundred and a few thousand particles were involved in the diffusion processes with holes and interstitials. Due to this, such diffusion processes involving cooperative movements of groups of particles might easily have been overlooked elsewhere. We are going to present results showing the contribution of this process to the diffusion inside of the crystal, the timescale on which these processes take place and how they vary with temperature. These simulations were carried out using Langevin dynamics.

In the last part of this thesis we will discuss simulations, where in addition to the misfit shear has been introduced. The shear is implemented by moving the walls with constant velocity in opposite directions. As the walls consist of frozen particles which interact with the mobile particles inside of the crystal, this leads to shear stress. We have observed several different phenomena resulting from this shear, depending on the shear velocity, the temperature and the value of the misfit, including the formation of shear bands, the fragmentation into several domains with different orientations and the creation of holes inside of the crystal. These simulations were also carried out with the programme package HooMD-blue using a Langevin thermostat.

Note to the reader: The main contents of the three result chapters of this thesis (including the description of the phase switch Monte Carlo method in comparison to the thermodynamic integration method) have already been published, or the publication is at least in preparation, in three papers [26–28]. In order to avoid unnecessary rephrasing, the text of these papers closely follows the wording of the following chapters in large parts, as indicated in the respective chapters in more detail.

Chapter 1

Model system and methods

In the first sections of this chapter we will describe our model system and its most important features. We will include references to previous studies on the same system by Ricci et al, Chui et al and Medina et al. In the following sections we will briefly introduce the main ideas of Monte Carlo computer simulations and of Molecular Dynamics, specifically of Langevin Dynamics. Advanced Monte Carlo techniques such as the phase switch method in combination with the transition matrix method and the thermodynamic integration will be introduced in the next chapter. The description of the model system is similar to the one we are going to publish in Ref. [26], which is based on the present chapters.

1.1 Model system and important parameters

In this thesis we will investigate a colloidal crystal. As we have already mentioned in the introduction, colloids are suspensions of micro- or nanometre sized particles in solvent. They are a very popular model system when fundamental properties of condensed matter are studied, such as phase transitions, order-disorder-transitions, crystal nucleation, elastic properties or crack formation [29–40].

Experimentally, colloidal particles can be produced out of different materials and their interactions are tunable in many ways. For instance, when a solution of charged colloidal particles is considered, adding salt can modify the strength and range of the effective Yukawa potential acting between the particles. If the colloids are not charged and interact only via hard core repulsion, polymers can be added and introduce an attractive depletion interaction between the colloids, which can be controlled by varying

the concentration of the non-adsorbing polymers. The well-known Asakura-Oosawa model is a simple model which already incorporates all of these features.

Another example for an experimentally realizable colloidal system are polystyrene spheres containing a superparamagnetic core. If these particles are trapped at an air-water-interface, a two-dimensional layer can be obtained. Applying a magnetic field perpendicular to this interface leads to a purely repulsive dipole-dipole interaction between the particles with an r^{-3}-dependency on the interparticle distance [29, 33–37, 41–46], while the magnitude of the interaction strength can be controlled via the magnetic field [47, 48]. A lateral confinement similar to the one we are using in our computer simulations can be experimentally realized either in a mechanical way or by applying laser fields [43, 46, 49].

In our simulations we will consider a two-dimensional system comprised of purely repulsive monodisperse particles similar to the superparamagnetic polystyrene spheres. But as there are at present no experiments available for direct comparison of results and the r^{-3}-dependence of the dipole-dipole interaction is long ranged and thus computationally very inefficient, we will use an r^{-12}-potential with a cutoff (to make it strictly short-ranged) and shift (so that it ends at zero) instead. We added a smoothing factor in order to make it differentiable, which is important for the computation of the stress tensor. Thus, the resulting potential reads:

$$V(r) = \varepsilon\Big[(\sigma/r)^{12} - (\sigma/r_c)^{12}\Big]\Big[\frac{(r-r_c)^4}{h^4+(r-r_c)^4}\Big] \quad , \tag{1.1}$$

with parameters $r_c = 2.5\sigma$ and $h = 0.01\sigma$. Thus the particle diameter $\sigma = 1$ is our unit of length, and $\epsilon = 1$ sets the scale for the temperature. Note that in qualitative respects Eq. 1.1 can be taken as a generic model for a broad class of colloidal particles with short-range repulsive interactions (due to screened Coulomb interactions or due to polymer brush coating, etc).

We chose a density of $\rho = 1.05$ for the simulations in the commensurable case. Assuming the physical effect of truncating the potential can be neglected, only the choice of the combination $X = \rho(\varepsilon/k_BT)^{1/6}$ controls the phase behavior [50]. Thus, it suffices to choose a single density when the temperature variation is considered [1, 51]. For the particular choice $\rho = 1.05$, the melting transition occurs at about $T_m = 1.35$ [34, 51, 52] in the bulk. All of our simulations were carried out clearly below this temperature (we used $T \leq 1.0$), where the colloidal particles are arranged in a basically defect-free hexagonal lattice structure. This crystallization is possible due to the repulsive nature of their interaction. The lattice structure is stabilized by walls which were implemented in the y-direction. In this direction, the system is only a few rows of particle wide. The walls consist of two rows of frozen particles each, which interact with the mobile particles via the same purely repulsive potential with

which the mobile particles interact with each other. Particles cannot jump "into" or even beyond the walls, but the second row of wall particles is necessary nevertheless as the particles in the first "mobile" row still feel its effect due to the finite length of the cutoff. The system was strongly elongated in the x-direction, where we have also applied periodic boundary conditions in order to rule out any effects of the finite system length in this direction. A sketch of the system geometry is shown in Fig. 1.1

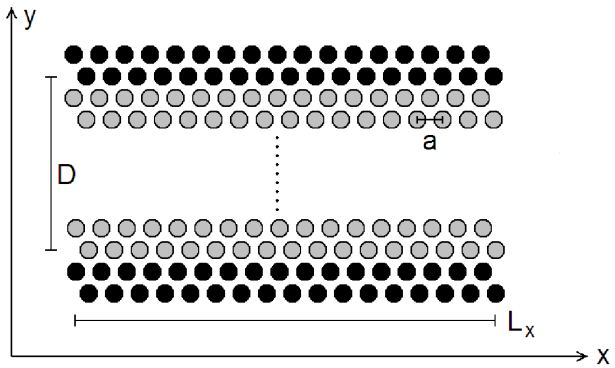

Figure 1.1: Sketch of the system geometry, showing the fixed wall particles (black spheres) and the mobile particles (gray spheres). The orientation of the coordinate axes is indicated, as well as the lattice spacing of the triangular lattice (a) and the linear dimensions L_x, D of the system.

We have used different system sizes depending on the computational possibilities: For simulations using the thermodynamic integration method and the phase switch Monte Carlo method, we had to use a relatively small system comprised of $N = 3672$ particles (including wall particles; thus 3240 mobile particles), which were originally arranged in 30 rows with 108 particles per row. The simulations carried out using Langevin dynamics utilized the program package hooMD-blue [13, 14], which is originally desinged to run on graphic cards. If graphic cards are used, there is a huge speed-up and we were able to make the system twenty times as large as before by placing 2160 particles in each of the 30 rows, yielding a total number of $N = 73440$ particles (again including walls; thus 64800 mobile particles). Unfortunately we realized that the single precision used on graphic cards is not sufficient for our crystalline system at temperatures lower than $T = 1.0$ (see Appendix C). Thus, we had to run all simulations at lower temperatures on regular CPUs. As this took considerably more time, we reduced the system size to the initial 3672 particles again for these runs wherever possible. In those simulations where the walls were sheared against the crystal, we had to carry out all simulations on CPUs due to the necessity for high accuracy (and due to the low temperatures we considered there), but we still used the larger system size as we needed the statistics and did not want to risk experiencing problems with effects of the finite system size in the x-direction.

Strictly speaking there are no crystals in two dimensional systems due to the lack of positional long-ranged order, but the colloids in our model system do arrange themselves into an ordered structure which can be classified as crystalline according to the Lindemann-criterion or the pair-distribution function. The Lindemann-criterion states

that a system can be regarded as crystalline as long as the Lindemann-parameter δ_{Lind}, which is esentially the width of the distribution of the nearest-neighbour distances in the crystal, is below a threshhold of $\delta_{Lind} \leq 0.1$. The definition of the Lindemann-parameter reads:

$$\delta_{Lind} = \frac{1}{a}\sqrt{\frac{1}{N}\sum_{i=1}^{N}(\vec{u}_i)^2} \quad , \tag{1.2}$$

a being the lattice constant, which is $a = 1.04867$ at the chosen density in our system. $\vec{u}_i$ denotes the displacement of particle i from its reference site:

$$\vec{u}_i(t) = \vec{R}_i(t) + \vec{R}_i(0) \quad . \tag{1.3}$$

As we are going to place the walls at various distances D apart from each other in the following studies (therby introducing an incommensurability into the crystalline structure), it is necessary to define a misfit parameter Δ. We define this misfit between the actual distance D between the walls and their distance $D_0 = n_y a\sqrt{3}/2$ in the commensurate case as

$$D = (n_y - \Delta)a\sqrt{3}/2 \quad , \tag{1.4}$$

where a is again the lattice constant in the commensurate case and n_y denotes the number of rows (of mobile particles) parallel to the walls.

In order to investigate the behaviour of the system which occurs when the walls are placed at distances D apart from each other which are incommensurate with the crystalline structure, it proved useful to compute the anisotropy of the stress tensor given by

$$\delta\sigma = \sigma_{yy} - \sigma_{xx} \tag{1.5}$$

where σ_{ij} are the Cartesian components of the pressure tensor, derived by applying the virial formula, which yields [53–55]:

$$\sigma_{ij} = \frac{1}{V}\left[\sum_{a\neq b} U'(R^{ab})\frac{R_i^{ab}R_j^{ab}}{R^{ab}} - n_x n_y k_B T\delta_{ij}\right] \quad , \tag{1.6}$$

V being the two-dimensional "volume" of the stripe, $U'(R) = \frac{dU}{dR}$, $\vec{R}^{ab} = \vec{R}^b - \vec{R}^a$ and $n_x \cdot n_y = N$ being the number of particles.

In these studies, we will use two different definitions of the mean square displacement (MSD) of the particles: With $\text{MSD}_{\text{start-conf}}$ we refer to the MSD with respect to the starting configuration, defined as $\text{MSD}_{\text{start-conf}}(t) = \langle(x(t) - x(0))^2\rangle_N$, where $\langle ...\rangle_N$ denotes the average taken over all (mobile) particles in the system, while $\text{MSD}_{time-diff}$ refers to the MSD with respect to the time difference between the configurations defined as $\text{MSD}_{\text{time-diff}}(\Delta t) = \langle(x(t) - x(t+\Delta t))^2\rangle_{N,t}$, where now $\langle ...\rangle_{N,t}$

denotes the average taken over all (mobile) particles in the system *and* over all configurations which are a time interval Δt apart from each other.

In order to avoid confusion, we will refer to the rows directly adjacent to the walls as row 1 respectively row 30, and to the inner rows as row 2-29 in the following chapters.

1.2 Properties of the chosen model system

In order to test whether our chosen model system exhibits a crystalline structure at the temperatures and densities we used in our simulations, we calculated the next neighbour distances. In Fig. 1.2 we have plotted the distribution of the distance of each particle to its six nearest neighbors for several temperatures T, which yields a peak with a squared width $w^2(T)$ which is clearly below 0.01, so that the Lindemann-criterion (see Eq. 1.2) is met for all temperatures that we have used. Therefore we do not have to worry about the peculiarities of melting in two dimensions [51].

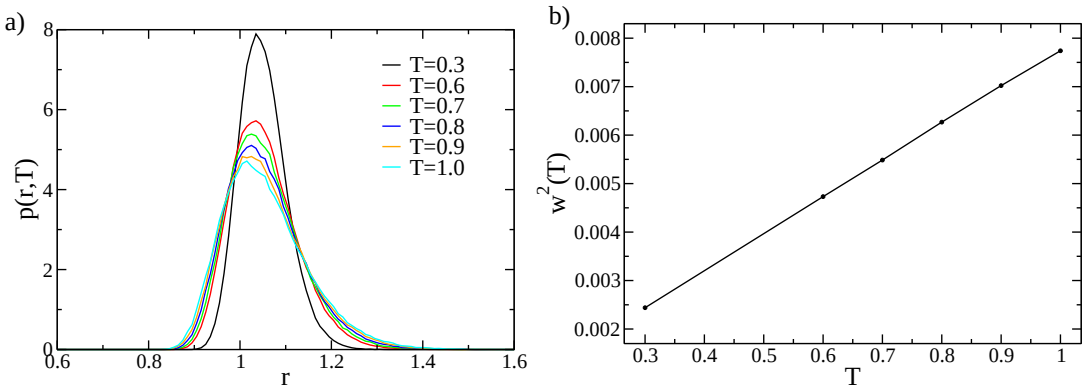

Figure 1.2: a) The distribution of the distance r between nearest neighbor particles in the crystal: For each particle, the distance to its six nearest neighbors was used. Different temperatures T as indicated. Distributions normalized to area=1. b) Squared width of the distribution, defined as $w^2(T) = \frac{\langle r^2(T)\rangle - \langle r(T)\rangle^2}{\langle r(T)\rangle^2}$. Simulations in the fully commensurate case with 30 crystalline rows.

Placing the walls closer together, so that they are not commensurate with the crystalline structure of the mobile particles any more, leads to a structural transition. In the course of this transition, the number of rows parallel to the walls is reduced.

In order to investigate this structural transition, Chui et al [1–3] have computed the anisotropy of the stress tensor σ_{ij} (see Eq. 1.5). Fig. 1.3 shows that this stress

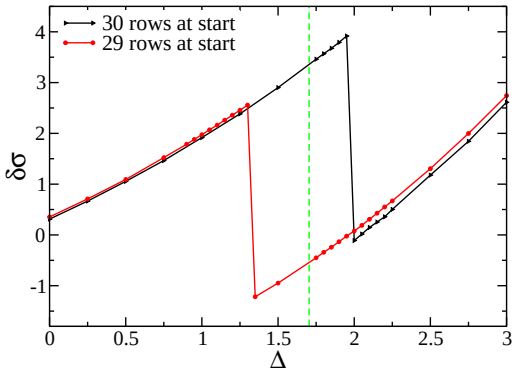

Figure 1.3: Stress curve showing at which values of the misfit Δ the structural transition occurs which reduces the number of rows parallel to the walls. The broken line shows the exact location of this transition in equilibrium, which was obtained using the phase switch Monte Carlo method [27].

anisotropy is already nonzero for zero misfit due to the confining effect of the walls in the y-direction, which somewhat hinders the vibrations of the mobile particles in their potential wells, but this effect is of no importance here. Increasing misfit at first increases the stress anisotropy for a system that started out with 30 crystalline rows of particles. But at a misfit of $\Delta \approx 2.0$, the stress suddenly decreases and then slowly increases again. This behaviour can be explained by the fact that the system spontaneously rearranges itself into 29 rows of crystalline particles at $\Delta \approx 2.0$. As the number of particles remains constant in these NVT ensemble simulations, the particles which used to sit in the row which has disappeared in the transition therefore have to distribute themselves in the remaining rows. Chui et al have found evidence that the ideal distribution of these "extra" particles is given by putting four extra particles in each of the 27 inner rows and leaving the rows directly adjacent to the walls free of extra particles (as these rows are stabilized by the lattice structure of the walls). Thus, in the inner part of the crystal a new crystalline structure emerges with smaller lattice spacing in the x-direction (due to the increased number of particles) which is no longer commensurate with the lattice spacing between the particles in the row directly adjacent to the walls. Because of this incommensurability, there are areas in the crystalline structure where the particles of the rows directly next to the walls and the particles of the inner rows are in energetically unfavourable proximity to each other. These regions of higher energy (and also increased particle mobility as we will show in the next chapter) are called solitons. Fig. 1.4 illustrates such "soliton staircases" [56, 57].

If a simulation starts off with just 29 rows of crystalline particles and the appropriate number of extra particles distributed into them, the stress curve looks different (Fig. 1.3). At small misfits the structure still rearranges itself into 30 rows, but already from a misfit of $\Delta \approx 1.3$ onwards the 29 rows remain at least metastable. The exact location of the transition was therefore obviously obscured by a large hysteresis. We therefore applied two different methods of computing the free energy difference between the two structures in order to locate this transition more precisely. The results

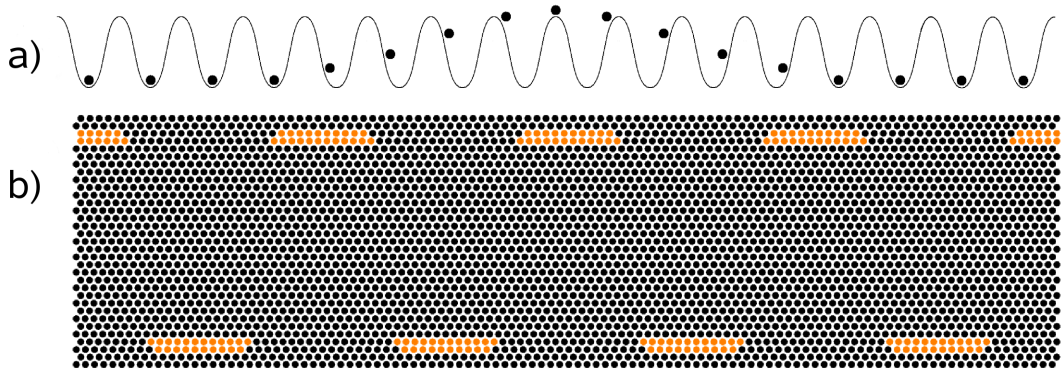

Figure 1.4: a) Putting $n + 1$ particles in a periodic potential with n minima creates a soliton configuration, i.e. over a range of several lattice spacings particles are displaced from the potential minima (schematic). b) Soliton configuration in a lattice of $N = 3672$ particles (including walls) when the particles are arranged into 29 rows. Particles which are part of the solitons have been marked in orange. "Ideal" configuration for $T = 0$ is shown.

of these simulations are shown in Chapter 2.

1.3 Langevin Dynamics Simulations

There are two general approaches to classical computer simulations of condensed matter systems: If one is merely interested in statistical averages, Monte Carlo simulations [54, 58] are a good option as they aim at sampling the possible configurations of the system under consideration. As it is usually not an option to list every possible state of the system, importance sampling is typically applied, which ensures that states with a higher probability are sampled more frequently. Many different Monte Carlo methods have been developed over the past decades, two of which will be discussed in detail in Sec. 2.1 and 2.3.

However, sometimes it is necessary to obtain information about the trajectories of the particles or to let the system evolve in a physically more realistic way. In such cases Molecular Dynamics simulations have to be carried out, which aim at integrating the equations of motion of the particles. As this approach to computer simulations might be more intuitive than Monte Carlo simulations, we will outline the main ideas of Molecular Dynamics first and briefly discuss Monte Carlo simulations in the following section.

The starting point for Molecular Dynamics are Newton's equations of motion, which read

$$m_i \frac{d^2 \vec{r_i}}{dt^2} = -\sum_{j \neq i} \nabla_i V(|\vec{r_i} - \vec{r_j}|) \equiv \sum_{j \neq i} \vec{F_{ij}} \tag{1.7}$$

for every particle i of the system, i.e. one needs to know all forces acting on this particle from all other particles in order to compute its acceleration. This system of $3N$ coupled differential equations can be solved approximately by making Taylor expansions in terms of Δt. The well-known Velocity Verlet algorithm [59–61], which one obtains when developing up to the second order in Δt, then yields:

$$\vec{r}(t + \Delta t) = \vec{r}(t) + \vec{v}(t)\Delta t + \frac{1}{2}\frac{\vec{f}(t)}{m}\Delta t^2 \tag{1.8}$$

$$\vec{v}(t + \Delta t) = \vec{v}(t) + \frac{\vec{f}(t + \Delta t) + \vec{f}(t)}{2m}\Delta t \tag{1.9}$$

This Velocity Verlet integrator is very useful, as it shares the most important properties with Newton's equations of motion: it conserves energy on long time scales, it conserves the momentum of the system as a whole, it is time reversible and phase space is conserved, as well [58]. In contrast to Monte Carlo simulations, molecular dynamics simulations using only the Velocity Verlet scheme are strictly deterministic. They do not yield exact trajectories, however, as the time steps are finite. But exact trajectories are usually not needed anyway, as we do not want to calculate the exact route of any specific particle, but only averaged proporties of the system. In fact, the Lyapunov instability states that two configurations which are only slightly different diverge exponentially with time anyway.

As energy is conserved, the Velocity Verlet scheme corresponds to experiments in an NVE ensemble. As most real experiments are carried out at constant temperature (or pressure) rather than at constant energy, a thermostat is necessary in order to run simulations in the NVT ensemble. There are several options for thermostats, both deterministic and stochastic, which adjust the velocities in order to ensure that they follow the correct Boltzmann-distribution of the given temperature T. One such thermostat is the Langevin thermostat which introduces a dissipative force slowing the particles down as well as a stochastic force accelerating the particles by "kicking" them around in arbitrary directions, thus creating the desired velocity distribution. This is achieved by adding two new forces to the equations:

$$m_i \frac{d^2 \vec{r_i}}{dt^2} = \vec{F_i^C} + \vec{F_i^D} + \vec{F_i^R} = \sum_{j \neq i} \vec{F_{ij}} - \gamma \vec{v_i} + \vec{f_i} \ . \tag{1.10}$$

$\vec{F^C}$ is the conservative force and $\vec{F^D}$ is the dissipative force due to friction, which slows down the particles and is proportional to their velocities, thus ensuring that

particles which are too fast are being slowed down. $\vec{F^R}$ is a random force which "kicks" the particles around. In order to satisfy the Fluctuation-Dissipation theorem, this random force has to satisfy the following equation [63]:

$$\langle f_i^\alpha(t) f_i^\beta(t') \rangle = 2\gamma k_B T \delta_{ij} \delta_{\alpha\beta} \delta(t - t') \tag{1.11}$$

where α and β refer to the cartesian components of the vector $\vec{f}$ and i and j are indices of the particles.

As the direction of the kicks is arbitrary, the overall momentum of the system is no longer conserved, but slightly fluctuates. This is not a problem here as the system we have studied in the present thesis is a colloidal crystal, i.e. it is comprised of colloidal particles and solvent. As we have only explicitly simulated the colloidal particles, their momentum does not have to be conserved as the not explicitly simulated solvent particles can take away and add momentum to the movement of the larger particles. But at the same time, this leads to the disadvantage that Langevin Dynamics do not account for hydrodynamic interactions.

Using only implicit solvent particles can also alter the results of simulations of colloidal crystals, especially in the case where shear is present. Therefore, the very simple nature of the model system we used certainly affects our results. For example, the strongly non-newtonian flow profiles described in Chapter 4 might have been less pronounced if solvent particles had been explicitly simulated. There are several approaches to include solvent and hydrodynamic interactions into Molecular Dynamics simulations: particle based methods such as Multiparticle Collision Dynamics [152, 153], and lattice methods such as the Lattice Boltzmann method [65]. But as all of these approaches increase the necessary computer time for the simulations by at least a factor of 10, it was decided that this project would solely deal with the simple model with only implicit solvent. Thus we chose to use Langevin Dynamics, which is –alongside other thermostats and algorithms– included in the HooMD-blue program [13, 14].

There are also thermostats like the Dissipative Particle Dynamics [63, 64], which introduce hydrodynamic interactions into the simulations by conserving the momentum, and yet do not necessarily increase the CPU time by a large amount. But unlike Multiparticle Collision Dynamics or Lattice Boltzmann Simulations, the Dissipative Particle Dynamics thermostat would have introduced hydrodynamic correlations directly between the colloidal particles. This would not have yielded a realistic behaviour, because in a real system these colloidal particles interact via solvent particles with which they exchange momentum. The Langevin thermostat which does not conserve the momentum of the colloidal particles, is therefore better suited to this problem: In Langevin Dynamics simulations, the interactions of the colloidal particles with the solvent particles are represented by the random "kicks". Of course,

in a real system the solvent particles do not move around randomly. Momentum is strictly conserved while they collide with the much larger colloidal particles and with other solvent particles. But as the time intervals between collisions of the solvent particles with colloidal particles are much larger than the time between collisions of solvent particles with other solvent particles, the solvent particles change the direction of their movement and their velocity several times before colliding with the next colloidal particle. Therefore it is a valid approximation to model the interaction of the solvent and colloidal particles as random "kicks" as we have done it here by using the Langevin thermostat.

In all simulations, our particles have mass $m = 1$, and the time t is measured in the standard molecular dynamics time unit $\tau = t\sqrt{\frac{\epsilon}{m\sigma^2}}$.

1.4 Monte Carlo Simulations

As it is in many cases not necessary to know the exact trajectory of every particle in the system, but only statistical averages, Monte Carlo simulations can save a lot of time and effort. The basic idea behind Monte Carlo simulations [54, 58, 66] is to sample the phase space by randomly creating new configurations and accepting them according to their propability. Thus the correct probability distribution is sampled and averages of observables can be obtained by simply averaging over all sampled configurations without further reweighting. As we are going to carry out simulations in the NVT ensemble with fixed particle number, volume and temperature, the probability of a configuration depends on its internal energy E (which again depends on the particle positions $\{\vec{R}\}$) and is given via the Boltzmann weight

$$p(\{\vec{R}\})_{NVT} \propto e^{-\beta E(\{\vec{R}\})} \quad , \tag{1.12}$$

where $\beta = \frac{1}{k_B T}$.

So when setting up a Monte Carlo simulation, a start configuration is chosen, for example by distributing the particles randomly in the given volume. If no advanced method is used, the only Monte Carlo steps are then local moves, where a new position $\vec{r_i'}$ is suggested for a randomly chosen particle i. The energy change $\Delta E = E(\{\vec{r_1}, \vec{r_2}, ..., \vec{r_i'}, , ...\vec{r_N}\}) - E(\{\vec{r_1}, \vec{r_2}, ..., \vec{r_i}, , ...\vec{r_N}\})$ associated with this local move has to calculated. Of course, this new configuration is not completely independent from the previous configuration as one local move can only introduce a small change in the particle positions. However, this change should be independent from earlier configurations. Thus, the succession of configurations can be described by a Markow chain, in which each state of the system only depends on the preceding one.

In order to model a system at equilibrium, the "flow" into one such state should equal the flow out of it, where the flow from state i into state j is given by the product of the probability p_i for the system being in the particular state i and the transition probability w_{ij} for the system to jump from state i to state j. The "Master Equation" describing an equilibrium system therefore reads (in the time-independent case)

$$\sum_i p_i w_{ij} = \sum_j p_j w_{ji} \ . \tag{1.13}$$

This requirement is always met if the stricter condition

$$p_i w_{ij} = p_j w_{ji} \tag{1.14}$$

is fulfilled, which is called "Detailed Balance".

Detailed Balance can be enforced (and thus the correct sampling of the probability distribution can be obtained) in simulations by applying the Metropolis Criterion: The transition rates w_{ij} are chosen as [66]:

$$w_{ij} = \begin{cases} e^{-\beta \Delta E} & if \ \ \Delta E > 0 \\ 1 & else \end{cases} \tag{1.15}$$

This ensures that configurations with lower internal energies are always accepted, while higher energies are only accepted with a certain probability. This can cause problems if the phase space consists of two or more disjunct regions of high probability, which are separated by an area of low probability. An example of such a situation would be two phases, separated by a two-phase region with higher free energy. In order to ensure that the simulation crosses the valley of low probability and samples both phases correctly, simulations often have to be reweighted. In the simplest case, this can be done by modifying the Hamiltonian of the system in such a way that the probability becomes more or less equal for all states [67, 68]. This is especially easy if the expected probability distribution is known approximately, for example by extrapolating the probability distributions obtained by preceding runs to the desired temperature. In this case, the acceptance criterion incorporates not only the energy difference between the old and new configuration, but also their weight difference, thus ensuring that all states are sampled with approximately the same probability. In the end, the used weights have to be taken into account when averages are computed or when the real, non-reweighted probability distribution is needed.

As the probability distribution of the system is usually not known beforehand and also because this method of sampling regions of low probability is not always the most efficient one, many different advanced simulation techniques have been developed over the past decades [6, 69, 70], two of which will be introduced in detail in the next chapter.

Chapter 2

Introducing a Misfit

The results presented in this chapter have already been published in Ref. [27], which is fully based on the work done for the present chapter. The wording of this publication is almost identical to the present chapter with the exception of a few sentences in the introduction to the present chapter, the description of the details of the simulation, the first paragraphs in the description of the phase switch method, parts of the description of the thermodynamic integration method, a few sentences in the results section and the addendum.

Periodically ordered arrays of nanoparticles, colloidal crystals, crystalline mesophases formed from surfactant molecules or block copolymers, etc. are all examples of complex periodic structures that can occur in soft matter systems. Since often the interactions between the constituent particles of these structures are to a large degree tunable, one has the possibility of producing materials with "tailored" properties which have potential applications in nanotechnological devices [71–75]. When seeking to provide theoretical guidance for understanding structure-property relations in such complex soft matter systems, a basic issue is how to judge the relative stability of competing candidate structures, i.e. to distinguish the stable structure (having the lowest free energy) from the metastable ones. For standard crystals formed from atoms or small molecules, this question can be answered by comparing ground state energies of the competing structures (and –if necessary– also taking entropic contributions from lattice vibrations into account, within the framework of the harmonic approximation). In soft matter systems, disorder in the structure and thermally driven entropic effects rule out such an approach, and hence there is a need for computer simulation methods that compute the free energy of the various complex structures. However, as is well known, the free energy of a model system is not a direct output of

either Molecular Dynamics or Monte Carlo simulations, and special techniques have to be used [54, 58, 76–79].

In principle, one can obtain the absolute free energy of a structure by linking it to some reference state of known free energy by means of thermodynamic integration (TI) [4, 5, 54, 58, 76–82]. The strengths of TI are that it is both conceptually simple and often straightforward to implement. Its principal drawback is that the quantity of interest, namely the free energy *difference* between candidate structures is typically orders of magnitude smaller than the absolute free energies of the individual structures which TI measures. Essentially, therefore, TI estimates a small number by taking the difference of two large ones. As a consequence, the precision of the method is limited and an enormous (even sometimes wasteful) investment of computer resources may be needed to resolve free energy difference accurately [77].

A much more elegant approach, albeit one which is not quite so easy to implement as TI, is the "phase switch Monte Carlo" [6–12] technique. This method is potentially more powerful than TI because it focuses directly on the small free energy difference between the structures to be compared, rather than their absolute free energies. In previous work, the precision of the method was demonstrated in the context of measurements of the free energy difference between fcc and hcp structures of hard spheres [9], the phase behaviour of Lennard-Jones crystals [9] and as a means of studying liquid-solid phase transitions [7]. In the latter case, simple model systems containing only a few hundred particles could be studied, while for the study of the fcc-hcp free energy difference [6, 10] larger systems of up to 1728 particles could be studied by virtue of the fact that these crystals only differ in their packing sequence of close-packed triangular defect-free lattice planes. However, it is an open question as to what system sizes one can attain with the phase switch method for more general crystalline systems, including – as in the present work – ones which exhibit considerable structural disorder ("soliton staircases", see below). Furthermore, there have hitherto been no like-for-like comparisons of the TI and phase switch methods on the same system, so whilst there are good reasons for *presuming* the superiority of phase switch (in terms of precision delivered for a given computational investment), this has never actually been quantified.

In this chapter, we address these matters, considering as a generic example a two-dimensional colloidal crystal in varying geometrical confinement [1–3, 83, 84]. As we have already described in Sec. 1.1, an experimentally realizable example of such a colloidal crystal is a layer of polystyrene spheres with superparamagnetic cores trapped at an air-water-interface and influenced by a magnetic field. Lateral confinement could in this case be implemented either mechanically or by laser fields.

Of course, there exist many related problems in rather different physical contexts

("dusty plasmas" [85, 86], i.e. negatively charged SiO_2 fine particles with $10\mu m$ diameter in weakly ionized rf discharges; lattices of confined spherical block copolymer micelles [87]; vortex matter in slit channels [88], etc.). However, we will not address a specific experimentally realizable system, rather we focus on the methodological aspects of how one can study such problems by computer simulation.

The outline of this chapter is as follows. In Sec. 2.1 we will describe the phase switch Monte Carlo method on which the main emphasis of this part of the study lies. Sec. 2.2 deals with the transition matrix method which we used in order to create a weight function. In Sec. 2.3 we will introduce the thermodynamic integration method of Schmid and Schilling [4, 5] which was used for comparison and to verify our results.

In Sec. 2.4 we will summarize the key results for the chosen model system: like in chapter 3 we are considering strips of two-dimensional crystals confined between two walls. When the distance between the (corrugated) rigid boundaries is varied, structural phase transitions may occur [1–3, 84, 89–91] Here, a succession of transitions in the number of crystalline rows n parallel to the walls occurs, $n \to n-1 \to n-2$, with increasing compression, accompanied by the formation of a "soliton staircase" at the walls [1–3, 84]. In Sec. 2.5 we show that phase switch Monte Carlo [7–9] can accurately locate these phase transitions despite the need to deal with thousands of particles, and is orders of magnitude more efficient than thermodynamic integration. Sec. 2.6 sheds some light on the ensemble inequivalence observed for this particular model system. Sec. 2.7 shows how the phase switch method is able to distinguish between different metastable candidate structures and to determine which one of them is the stable one. Sec. 2.8 summarizes some conclusions.

The addendum describes an application of the Schmid-Schilling thermodynamic integration method, where the interfacial free energy between a colloidal crystal and a flat wall is calculated.

2.1 The Phase Switch Method

The "Phase Switch Monte Carlo method" was originally introduced by A.D. Bruce, N.B. Wilding and G.J. Ackland in 1997 [6, 8] in order to calculate the free energy difference between the fcc crystal phase and the hcp crystal phase of a hard sphere system. Using this method, they were able to establish which of the two phases represents the ground state under certain conditions. As this free energy difference is quite small, preceding attempts using thermodynamic integration and thus calculating the absolute free energies of each phase seperately instead of calculating the energy

difference between them had led to results that were contradicting each other as the errors were too large.

As the only difference between an hcp and an fcc phase is that an fcc structure can be represented by a repetition of three layers of particles shifted against each other, while the hcp phase consists of only two different layers shifted against each other, all of these layers displaying the same lattice structure, the idea came up to introduce a Monte Carlo move that would shift every third layer of the system by the lattice constant and thus take the system from the fcc to the hcp phase and vice versa. These moves were combined with the standard local Monte Carlo moves in an NVT ensemble (and later on, in an NPT ensemble, too). By simply measuring how much simulation time was spent in each of the two phases, it was possible to accurately determine the difference in the free energies and therefore also to see which of the phases represented the ground state, as $\Delta F = \ln(A^{(1)}/A^{(2)})$, $A^{(1)}$ and $A^{(2)}$ being the times spent in the respective phases which are proportional to the statistical weight of each phase [77]; $T = k_B = 1$.

This method was later generalized to the computation of energy differences between a solid and a fluid phase of hard spheres [7] and additionally to systems with soft potentials [9–12].

In order to calculate the free energy difference between two phases in a single simulation run, the two phases have to be linked by a sampling path. In many popular approaches, a direct path between the two phases is constructed in the form of a continuous set of macrostates associated with the values of some order parameter which distinguishes one phase from the other (common examples are the total energy or density of a fluid). This path traverses mixed phase (interfacial) states [92] and is negotiated using some form of extended sampling to overcome the free energy (surface tension) barrier associated with the interfacial states. One way to do this is the multicanonical method [67]. Alternatively one can directly measure free energy differences between successive points along the path as is the case in the successive umbrella sampling technique [70].

In many cases utilizing an inter-phase path that encompasses interfacial states works well, particularly for fluid-fluid transitions or lattice models of magnets. However, in other cases such a path can be problematic [77]. For example in the case of solid-liquid coexistence, a connecting path will typically run from a crystalline phase through several different distinct states including droplets of liquid in a crystal, a slab configuration and crystalline droplets in a liquid before finally reaching the pure liquid phase [93]. In such cases the identification of a suitable order parameter to guide the system smoothly from one pure phase to the other can be difficult, and as a result the system may experience kinetic trapping (e.g. in defective crystalline states).

Thus it is highly desirable to have a method which can directly "leap" between the two pure phases (which we shall label α, with $\alpha = 1, 2$), avoiding the problematic mixed phase states. If the system jumps back and forth between these phases a sufficient number of times within one simulation run, the relative probability with which the system is found in each of them directly yields the free energy difference between these phases via $\Delta F = -\ln\left(\frac{P^{(\alpha=1)}}{P^{(\alpha=2)}}\right)$. The phase switch method achieves this by supplementing standard local particle displacement moves (and in the case of a simulation in the NpT ensemble, moves which scale the volume of the simulation box), with moves that switch the system from one phase directly into the other phase. This switch is facilitated by the *representation* of particle configurations in the two phases. Specifically we associate a fixed reference configuration $\{\vec{R}^{(\alpha)}\}$ with each phase. The reference configuration is an arbitary configuration drawn from the set of configurations that are identifiable as 'belonging' to phase α. We then associate each particle with a unique site of the reference configuration, allowing us to write its position $\vec{r}_i^{(\alpha)}$ in terms of the displacement $\vec{u}_i$ from its reference site:

$$\vec{r}_i^{(\alpha)} = \vec{R}_i^{(\alpha)} + \vec{u}_i \tag{2.1}$$

Note that whilst there are two reference configurations (one for each phase), the phase switch method only considers one set of displacement vectors which are regarded as common to both phases.

Suppose we are currently in phase $\alpha = 1$, so that the particle coordinates are $\vec{r}_i^{(1)} = \vec{R}_i^{(1)} + \vec{u}_i$. For local moves in this phase we update particle coordinates (in the manner to be described) which, owing to reference sites being fixed, is equivalent to updating the displacement vectors. For a phase switch to phase $\alpha = 2$, we propose a new configuration which is simply formed by substituting the reference sites of phase $\alpha = 1$ with those of phase $\alpha = 2$. Thus the proposed configuration is $\{\vec{r}_i^{(2)}\} = \{\vec{R}_i^{(2)}\} + \{\vec{u}_i\}$. If this switch is accepted, i.e. if the resulting configuration of phase $\alpha = 2$ is energetically acceptable, the simulation will continue to run in phase $\alpha = 2$, again recording the displacements of all of the particles from the reference sites of phase $\alpha = 2$, and proposing switches back to phase $\alpha = 1$. In this way the system switches repeatedly back and forth between the phases, allowing one to record the relative probability of finding the system in each phase.

The switch operation leaves open how one chooses the lattice-to-lattice mapping between reference sites in the two phases ie. the relationship between the pairs of sites $\vec{R}_i^{(0)}$ and $\vec{R}_i^{(1)}$. In fact it turns out to be beneficial in terms of the efficiency of the method to choose this mapping such as to maintain any local structural similarities that may exist in the two phases. Thus having specified the reference sites for one

phase by labelling all the lattice sites with the index i, one should consider how each lattice site transforms under the structural phase transition, and assign the same index to the corresponding lattice site in the other phase. In the present model some particles (those not near the wall or the solitons) do not see a significant change to their local environment under the phase transition and so the mapping is straightforward. Only the particles redistributed from near the walls to the solitons see a significantly new environment and for pairs of these particles it is essentially arbitrary which index they receive.

Now generally speaking the displacement vectors that characterise phase $\alpha = 1$ are not typical of phase $\alpha = 2$ and thus it will not be energetically acceptable to perform the switch from typical configurations of phase $\alpha = 1$. As a consequence, in a naive implementation such a global move will almost always be rejected by the Monte Carlo lottery. This problem is circumvented by employing extended sampling methods [77, 78, 94] that introduce a bias in the accept/reject probabilities for local moves that enhances the probability of displacements being generated in phase $\alpha = 1$ for which the phase switch to $\alpha = 2$ *is* energetically acceptable. We have used the transition matrix Monte Carlo method [94–96] in order to create a suitable weight function for this biasing, which will be described in detail in sec. 2.2.

The obvious observable to which the bias should be administered is a quantity related to the instantaneous energy cost of the switch, since this measures how likely it is to be accepted. We have employed the switch energy order parameter M described in Ref. [11], which for switches from phase $\alpha = 1$ to $\alpha = 2$ is defined as follows:

$$M^{(1)\to(2)}(\{\vec{u}\}) = \mathrm{sgn}(\Delta \mathrm{E}^{(1)\to(2)}) \cdot \ln(1 + |\Delta \mathrm{E}^{(1)\to(2)}|) \tag{2.2}$$

where

$$\Delta E^{(1)\to(2)} = (E^{(2)}(\{\vec{u}\}) - E^{(2)}_{ref}) - (E^{(1)}(\{\vec{u}\}) - E^{(1)}_{ref}) \tag{2.3}$$

where $E^{(\alpha)}_{ref}$ is the energy of the reference configuration in phase α, and $E^{(\alpha)}(\{\vec{u}\})$ is the energy in phase α, found by applying the displacement vectors $\{\vec{u}\}$ to the reference configuration $\{\vec{R}^{(\alpha)}\}$. An obvious substitution gives the order parameter for the switch from $\alpha = 2$ to $\alpha = 1$. Note that an important feature of this definition of this order parameter is the logarithm which ensures that the binning of the weight function is finer for small values of the energy difference and thus serves to ensure that the simulation can cover the entire range of M smoothly.

Now, when implementing local moves for particles, we consider not just the energy cost of the move within the current phase, but also the change in M associated

with the local move via a weight function $\eta(M)$. The acceptance criterion for the local move is therefore given by:

$$p^{(\alpha)}(\{\vec{u}\} \rightarrow \{\vec{u'}\}) = \min(1, \mathrm{e}^{-\beta(\mathrm{E}^{(\alpha)}(\{\tilde{\mathrm{u}}'\})-\mathrm{E}^{(\alpha)}(\{\tilde{\mathrm{u}}\}))+\eta(\mathrm{M}')-\eta(\mathrm{M})}). \tag{2.4}$$

Note that $E^{(\alpha)}(\{\vec{u'}\})) - E^{(\alpha}(\{\vec{u}\})$ is the energy difference due to the move in the phase α that is currently being simulated. The energy difference in the other phase is only needed for the computation of the new order parameter M' and therefore for the weights $\eta(M')$ associated with the move.

Phase switches are generally only accepted from states in which M is small – the so called gateway states. One instance in which M becomes small is if the displacement vectors are themselves small, i.e. if all particles are sitting close to their reference positions in both phases. Another instance is if there is a high degree of structural similarity among the phases, so that the displacements of many of the particles in one phase are typical of the displacements in the other phase. Note that one does not need to know or specify the gateway states to use the method. They are sought out automatically when one biases to small values of M.

The acceptance criterion for a phase switch from $\alpha = 1$ to $\alpha = 2$ itself reads:

$$p^{(1)\rightarrow(2)}(\{\vec{u}\}) = \min(1, e^{-\beta(E^{(2)}(\{\vec{u}\})-E^{(1)}(\{\vec{u}\})+\omega^{(2)}-\omega^{(1)}}) \,, \tag{2.5}$$

and similarly for the reverse switch. This phase switch also includes a weight ω to ensure that it occurs with a sufficiently high probability in both directions. Note that since the phase switch move alters the absolute particle coordinates, the associated energy change enters the switch acceptance criterion. We therefore chose the weights ω in such a way that $\omega^{(2)} - \omega^{(1)} = E^{(1)}_{ref} - E^{(2)}_{ref}$, ensuring that a phase switch is always accepted if all particles are sitting on their reference positions despite the fact that the energies of the two phases might differ significantly. In the case of phase switch simulations in the NpT ensemble, an additional volume scaling must also be taken into account, see below.

Once suitable weights have been determined (see Sec. 2.2), one samples the statistics of the two phases by accumulating a histogram of the biased order parameter distribution $\tilde{P}(M)$. At the end of the simulation, the effects of the weights is unfolded from this distribution in the standard manner for extended sampling [77] to find the equilibrium distribution $P(M)$. Close to a phase transition, this distribution will exhibit two well separated peaks, whose areas yield the free energy difference as described above. An example is shown in Fig. 2.1 (a). Also show in

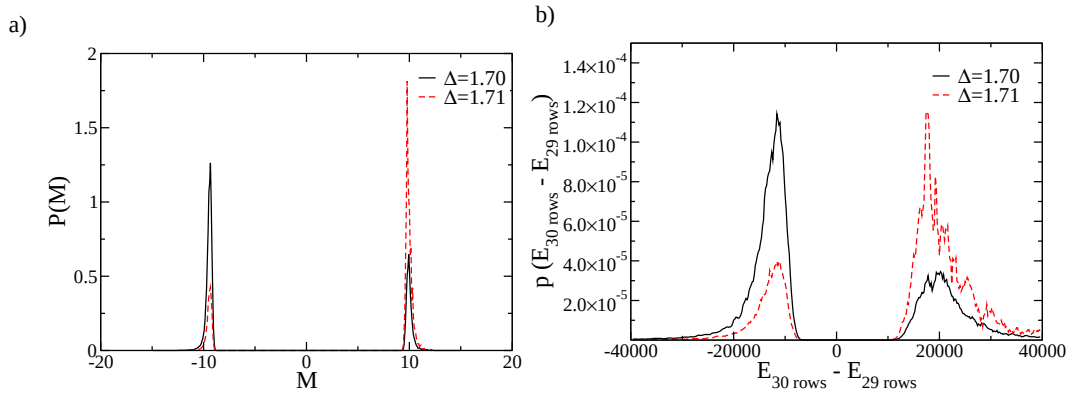

Figure 2.1: a) The order parameter distribution $p(M)$ for simulations at $\Delta = 1.70$ and $\Delta = 1.71$ carried out in the NVT ensemble. b) For comparison the same distribution is plotted against the internal energy difference between the two phases for fixed $\{\vec{u}\}$. The order parameter M is deduced from this energy difference $E_{29rows} - E_{30rows}$ via the definition given in eq. 2.2.

Fig. 2.1 (b) is the distribution of the instantaneous energy change under the switch $E^{(\alpha')}(\{\vec{u}\}) - E^{(\alpha)}(\{\vec{u}\})$ which similarly shows two peaks, one for each phase.

With regard to the choice of reference configuration in each phase, in principle this can be an arbitrary configuration belonging to that phase. In practice, however, for crystalline systems one finds that the degree of weighting required to access the gateway states can be reduced by choosing a reference configuration which is a perfect lattice. For more general system, e.g. those with crystalline disorder, or for fluids it may be advantageous to try to ensure that the particles are not sitting too close to each other (e.g. by energy minimization of the configuration [10]), since particles which are in close proximity reduce the number of gateway states significantly. (We note in passing that for fluid systems [11] one requires special approaches to guide particles to the gateway states that we will not discuss here as they were not necessary for our system.)

When we applied the phase switch method to the present model of 2d colloids in confinement, we discovered the phenomenon of cooperative ring rotation processes, which we subsequently investigated in detail. The findings of these studies are described in Chapter 3, where we present mostly simulations carried out with Langevin dynamics. However, the first time we saw these rotation processes was in the context of phase switch Monte Carlo simulations. Here, the ring rotation processes cause problems with the simulations –albeit rarely as the rotation processes are a priori rare and also, because the compression of the system reduces the movement of the particles further– as the ring rotation processes involve sets of particles on neighbouring

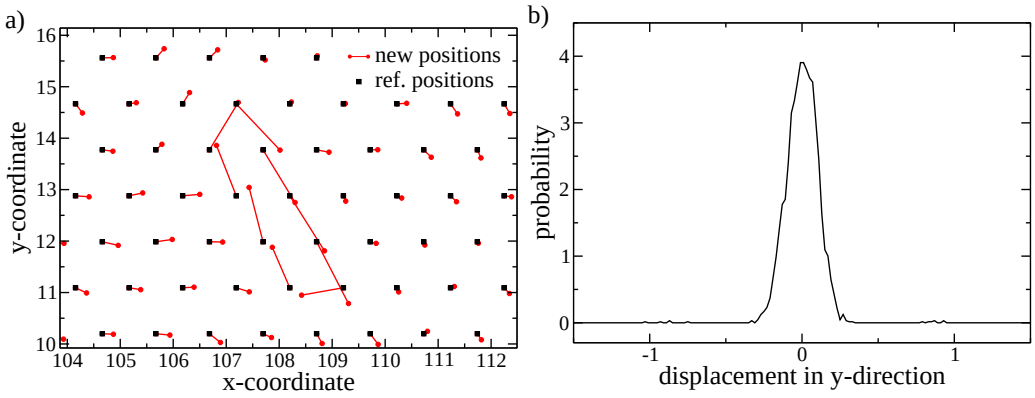

Figure 2.2: a) A section of a configuration that includes particles which have swapped positions in the phase with 29 rows. Black squares denote the reference configuration, red (grey) lines are the displacement vectors associated with the reference positions and red (grey) dots are the new positions. This simulation was carried out with 3240 particles at a misfit of $\Delta = 1.70$ in an NVT simulation with 1280 bins for the weight function. b) Typical histograms of the particle displacements in y-direction. The (almost completely invisible) very small peaks at about $+1$ and -1 correspond to particles which have swapped their positions.

lattice sites in adjacent rows jumping between rows during the simulation, creating in the process a ring of particles which occupy each others positions (cf. Fig. 2.2 (a)) and remain there. When this occurs it interferes with the operation of the phase switch method because the weight function is not designed to deal with it, so one is prevented from reaching the gateway states. Although one can envisage methods for solving this problem along the lines of those used in fluids [11], our solution to the problem was to simply suppress it. Measurements of the distribution of displacements in the y-direction is shown in Fig. 2.2 (b) and show that preventing particles from fluctuating any further in y-direction than $\Delta y = 0.5$ introduces a negligible constraint with regard to their natural fluctuations (and hence on free energy measurements). Doing so made ring rotations impossible and thus cured the problems associated with it. Of course, strictly speaking a constraint of the movement of the particles in the y-direction destroys the ergodicity of the simulations as some configurations are no longer possible. But these configurations did not contribute significantly to our measurements here.

Finally, we outline briefly how to apply the phase switch method in the NpT ensemble. The advantage of the NpT ensemble is that the results obtained at one pressure can easily be extrapolated to other values of the pressure by standard histogram reweighting methods. The difference between the NVT and the NpT ensemble in this case is that additional volume moves have to be carried out in the NpT ensemble. In such moves, all particle coordinates are scaled (along with the box) in both phases

in the standard way [11, 58]. Additionally, it can prove useful to combine the phase switch move itself with a volume scaling move if the equilibrium densities of the two phases differ from each other as it was the case for our system. For details on the underlying statistical dynamics, and acceptance probabilities, see Ref. [11]. The problem of particles switching their positions and thus creating configurations which prevented any further phase switches from being accepted did not occur in the case of simulations in the NpT ensemble for our system. However, this might simply be due to the rarety of these ring rotation events and not a general feature of the simulations in the NpT ensemble. We obtained (within the error bars) the same free energies whether or not we restricted the movement of the particles in the y-direction in the way we had to restrict them in the NVT ensemble.

2.2 The transition matrix method

There are many different methods of obtaining a weight function $\eta(M)$ for a Monte Carlo simulation. One quite popular method is the Wang-Landau-Sampling [69]. When using this method, the range of the order parameter M used in the simulation is divided into several bins. Each time one of these bins is visited, a histogram $H(M)$ of this bin is increased by one and the weight associated with the same bin is increased by a certain value $\Delta\eta$. As the weights change after every step, this simulation is obviously biased, but it also builds up a weight function rather quickly. Once the histogram H is sufficiently flat, which means that a rough estimate for the weight function has been obtained, all of the histograms are set back to zero and the increment for the weight function $\Delta\eta$ is decreased to a smaller value. This procedure is repeated several times until a sufficiently good weight function has been obtained.

One drawback of this method is that the simulations are biased throughout the whole time and therefore also the weight function belongs to a biased simulation. Of course, this bias becomes smaller as the updates of the weight function $\Delta\eta$ decrease. And even more importantly, this method is quite easy to implement and works sufficiently well for most problems, which leads to its high popularity.

A simpler approach is the multicanonical reweighting, where an estimated weight function has to be known beforehand and is used to reweight the simulation in a way that all states are visited with approximately the same probability. Such estimates for the weight function can be obtained by extrapolating preceding simulations at different parameters, e.g. at a higher temperature where no weight function might have been necessary. But as such a weight function is in many cases not known beforehand, the multicanonical reweighting has been extended to more sophisticated

methods. One such method for reweighting a simulation in order to overcome the typical free energy barriers (associated for example with interfaces) is the successive umbrella sampling [70]. In this method, the simulation range is also divided into a number of bins (similar to Wang-Landau sampling), but the simulation is restricted to just two of these bins at every time, sampling each pair of neighbouring bins one after the other. Thus it is possible to calculate the ratio of probabilities $\frac{P_{i+1}}{P_i}$ for each pair of neighbouring bins in the whole range, from which one can calculate the overall probability distribution, and therefore also the weight function, by simply multiplying these ratios, starting from the first pair of bins, up to the desired pair of bins, and thus getting the ratio of the probabilities of any bin in relation to the first bin: $\frac{P_i}{P_0} = \frac{P_1}{P_0} \cdot \frac{P_2}{P_1} \cdot \frac{P_3}{P_2} \cdot \ldots \cdot \frac{P_i}{P_{i-1}}$. As P_0 is determined by the normalization, one can calculate the probabilities of every bin in this way. In order to make this method work, it is crucial that the bins are not too large, so that the simulation fully explores both bins which are allowed to the simulation at each time. If necessary, one can additionally use an extrapolation of the ratios of probabilities of the previous bins as a weight function for the current bins. In this way, one should be able to simulate the full range of the order parameter.

This method introduces less bias into the simulation than the Wang-Landau-Sampling, but it can be a bit tedious to increase the accuracy of the weight function obtained with successive umbrella sampling, because that would imply increasing the statistics for every single pair of bins or alternatively choosing by hand which bins need more statistics, while a method like the Wang-Landau-Sampling simply has to be restarted with the already existing weights and will automatically increase its accuracy further and further.

Here, we will use the transition matrix method for our simulations, as this method combines the advantages of being (almost) unbiased like the successive umbrella sampling and at the same time as convenient to handle as the Wang-Landau method. The following description of the transition matrix method is taken from [27]. The details of the implementation can also be found in [10, 11, 94] and the references given therein.

The general idea of the transition matrix method for determining weight functions is to record the acceptance probabilities of all attempted transitions and extract the ratio of the states' probabilities from it. As all attempted transitions contribute to the weight function, including those that were rejected, the weight function can be built up rather quickly.

In the transition matrix method the weights are updated "on the fly" throughout the simulation (as in Wang-Landau sampling), allowing the simulation to explore an ever wider range of values of the order parameter M as the weight function evolves, until

it eventually encompasses the gateway states of low M. But in contrast to Wang-Landau sampling, the weight functions which are actually used in the simulation runs are only updated every few thousand steps, thus ensuring that detailed balance is observed at any given time (expect the rare moment where the weight function is updated), while in Wang-Landau sampling every Monte Carlo step changes the weight function. Therefore the transition matrix method collects equilibrium data from the outset of the simulation. Once a sufficiently smooth weight function has been obtained, one can cease updating the weight function and perform a simulation run with a constant weight function.

To implement the transition matrix method, the range of the order parameter M, for which a weight function is desired, is divided into a number of bins. In our case this range corresponds to the values of M that lie between the peaks in $P(M)$ which correspond to the two phases (cf. Fig. 2.1a). A good choice for the binning of the order parameter is to choose the bins in such a way, that the weight difference between adjacent bins satisfies [11] $|\eta(M_{i+1}) - \eta(M_i)| < 2$. Then, for every attempted move the acceptance probability p, (which is calculated anyway for use in the Metropolis criterion) is stored in a collection matrix C:

$$C(M \to M') \Rightarrow C(M \to M') + p \tag{2.6}$$

At the same time, the probability for rejecting the move and thereby keeping the current value of the order parameter is also stored:

$$C(M \to M) \Rightarrow C(M \to M) + (1 - p) \tag{2.7}$$

It is important to note that these probabilities p are the "bare" acceptance probabilities and do not include any weights.

The transition probabilities are then simply calculated by a normalization of the values in the collection matrix, with the sum on the right hand side including all possible states to which the system can jump from a given state:

$$T(M \to M') = \frac{C(M \to M')}{\sum_k C(M \to M_k)} \tag{2.8}$$

In the most general case, this method would create an $N \times N$ matrix, N being the number of bins or values of the order parameter M. In order to derive the correct probability distribution from such an $N \times N$ transition matrix, it is necessary to compute the eigenvector to the largest eigenvalue of this matrix. Appendix B explains why this yields the correct probability distribution. However, it is not necessarily required to know the exact probability distribution in order to create a weight function that will

work sufficiently well. Therefore it is possible to take only those transitions occuring between neighbouring bins of the order parameter into account when computing the weight function. In terms of the transition matrix, this means that only the diagonal elements - corresponding to transitions from a state to itself - and the first off-diagonal elements - corresponding to transitions from one state to the adjacent ones - are taken into account. Using this approach the weight function can be calculated quite easily without the need to compute eigenvalues or eigenvectors of the transition matrix. In this case, the ratio of the probabilities of two adjacent states can be read off directly from the transition matrix via

$$\frac{P(M_{i+1})}{P(M_i)} = \frac{T(M_i \to M_{i+1})}{T(M_{i+1} \to M_i)} \tag{2.9}$$

yielding the weight difference

$$\begin{aligned} \eta(M_{i+1}) - \eta(M_i) = -\ln\left(\frac{P(M_{i+1})}{P(M_i)}\right) = \\ -\ln\left(\frac{T(M_i \to M_{i+1})}{T(M_{i+1} \to M_i)}\right). \end{aligned} \tag{2.10}$$

Of course, when running the simulation, the system is still free to perform transitions between any values of M. But these transitions are not registered in the transition matrix and thus are also not taken into account when calculating the weights. In the present study this was found to produce accurate and useful weight functions as transitions between distant values of M were rare and the entries in the second off-diagonal elements of the transition matrix were already considerably smaller than the ones we used for the calculation of the weights.

By accumulating the transition matrix in the course of a simulation, one obtains an estimate for $P(M)$ which can be used to update $\eta(M)$, thereby allowing the simulation to explore a wide range of M. Repeated updates of $\eta(M)$ thus extend systematically the range of M over which one accumulates statistics for the weight function, until ultimately one reaches the gateway states. However since updating the weight function during a simulation violates detailed balance, we chose to do this at rather infrequent intervals of 20000 sweeps. Once the weight function extends to the gateway states, we stop updating the transition matrix and perform a long phase switch simulation with a fixed weight function in order to accumulate equilibrium free energy data.

An example of a weight function created for the system with $N = 3240$ particles (plus 432 fixed wall particles) at a misfit of $\Delta = 1.7$ is given in fig. 2.3, also illustrating how the definition of the energy order parameter M given in eq. 2.2, which

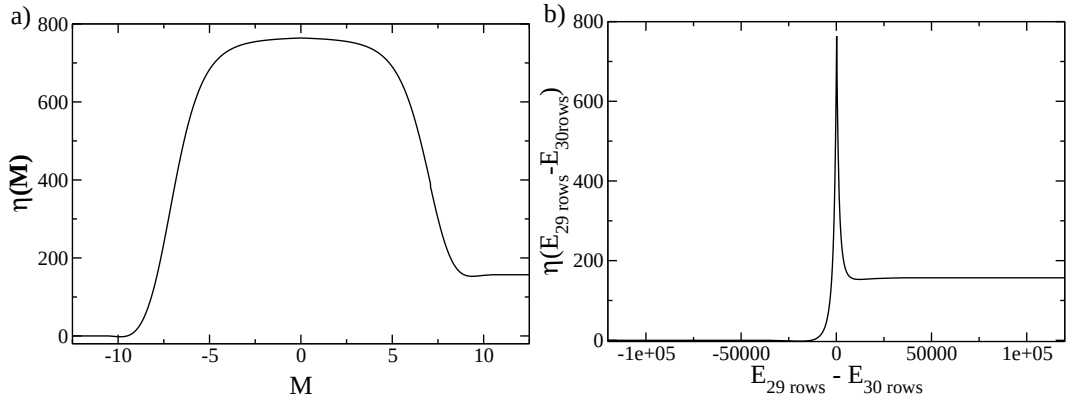

Figure 2.3: Weight functions for the two-dimensional colloidal crystal with $N = 3240$ particles and structured walls at a misfit of $\Delta = 1.7$. The left minimum corresponds to states where the system was simulating the phase with 29 rows, the right minimum corresponds to 30 rows. Note that the weights have an exponential influence on the acceptance criterion. Part a) shows the weights plotted against the order parameter M as defined in eq. 2.2, b) shows the same weight function plotted against the energy difference between the two phases in order to illustrate how the definition of the order parameter in the logarithm of the energy difference stretches the part around $M = 0$, where phase switches are most likely to happen.

includes a logarithm of the energy difference, leads to a finer binning in the part closer to $M = 0$, where the phase switches are most likely to happen. In fact to ensure that the transition matrix estimate of the weight function was sufficiently smooth and reliable in this region we reduced the number of bins in this region somewhat.

2.3 The Schmid-Schilling thermodynamic integration method

The description of the general approach of the Schmid-Schilling method – which is one variant of thermodynamic integration – is taken from [27]. After this outline of the method, we will discuss details of the implementation that were specific to our model system.

The general strategy of thermodynamic integration is to consider a Hamiltonian $\mathcal{H}(\lambda)$ that depends on a parameter λ that can be varied from a reference state (characterized by λ_0) whose free energy is known, to the state of interest (λ_1), without encountering phase transitions. The free energy difference ΔF can then be written as

$$\Delta F_1 = F(\lambda_1) - F(\lambda_0) = \int_{\lambda_0}^{\lambda_1} d\lambda' \langle \partial \mathcal{H}(\lambda')/\partial \lambda' \rangle_{\lambda'} \quad . \tag{2.11}$$

For a dense disordered system (fluid or a solid containing defects), Schilling and Schmid [4, 5] proposed to take as a reference state a configuration chosen at random from a well equilibrated simulation of the structure of interest, at values of the external control parameters for which one wishes to determine the free energy. Particles can be held rigidly in the reference configuration $\{\vec{r}_i^{\,\mathrm{ref}}\}$ by means of suitable external potentials. (We recall that a somewhat related thermodynamic integration scheme for disordered systems known as the "Tethered spheres method" has already been proposed by Speedy [97].) When these external potentials act, the internal interactions can be switched off. In practice, we used the following pinning potential $U_{\mathrm{ref}}(\lambda)$ to create the reference state, where r_{cut} is the cutoff range.

$$U_{\mathrm{ref}}(\lambda) = \lambda \sum_i \phi(|\vec{r}_i - \vec{r}_i^{\,\mathrm{ref}}|/r_{\mathrm{cut}}) \quad \text{with}\, \phi\,(x) = \begin{cases} x-1 & \text{if } \; x < 1 \\ 0 & \text{else} \end{cases} \tag{2.12}$$

Instead of the linear pinning potential $\phi\,(x)$ it is also possible to use other shapes of the pinning potential, of course. In fact, using a steeper potential might have helped to decrease the necessary CPU time of our simulations, as a steeper potential might help to ensure that particles are sitting closer to the center of their potential wells, thus reducing the energy barrier of switching the interparticle potentials on and off.

Here it is to be understood that particle i is only pinned by well i at $\vec{r}_i^{\,\mathrm{ref}}$, and not by other wells. However, identity swaps need to be carried out to ensure the indistinguishability of particles. The free energy of this non-interacting reference system then is

$$F_{\mathrm{ref}}(\lambda) = \ln(N/V) - \ln[1 + (V_0/V) g_\phi(\beta\lambda)] \,, \tag{2.13}$$

where $\beta = (k_B T)^{-1}$, V_0 (in $d = 2$ dimensions) is $V_0 = \pi r_{\mathrm{cut}}^2$ and

$$g_\phi(a) = \frac{2}{a^2}[e^a - \sum_{k=0}^{2} a^k/k!] \,, \tag{2.14}$$

for the choice of $\phi(x)$ written in Eq. (2.12) and again for $d = 2$ dimensions. Note that there is a typing mistake in Ref. [5] in Eq. 5, which leads to incorrect results for the case of $d = 3$ dimensions, where the formula has to read: $g_\phi(a) = \frac{d!}{a^d}$....

Then intermediate models $\mathcal{H}(\lambda)$ to be used in Eq. (2.11) are chosen as

$$\mathcal{H}'(\lambda) = \mathcal{H}_{\rm int} + U_{\rm ref}(\lambda) \quad , \tag{2.15}$$

where $\mathcal{H}_{\rm int}$ describes interactions in the system, which then are switched on (if necessary, in several steps). The free energy contribution of switching on these interactions can easily be determined by a Monte Carlo simulation which includes a move that switches the interactions on and off. The logarithm of the ratio of how many times the states with and without interactions were visited gives the free energy contribution: $\Delta F_2 = -k_b T \ln(P_{off}/P_{on})$. The free energy difference between the intermediate model where particle interactions are turned on and potential wells are also turned on, and the target system with particle interactions but without potential wells, then is computed by thermodynamic integration, for which

$$\langle \partial \mathcal{H}_{\rm ref}(\lambda)/\partial\lambda \rangle = \langle \sum_i \phi(|\vec{r}_i - \vec{r}_i^{\ \rm ref}|/r_{\rm cut}) \rangle \tag{2.16}$$

needs to be sampled [4, 5].

Before applying this method to the colloidal model system we were aiming at, we implemented it for the one-dimensional Ising model as shown in Appendix A in order to fully understand the method and to reproduce some analytically known results.

As we will show in Sec. 2.5 that the phase switch method has outperformed the thermodynamic integration method in terms of efficiency and accuracy when computing free energy differences between two crystalline phases of our colloidal model system, we have also included simulations where the Schmid-Schilling-method was applied to this two-dimensional system as well as to a three-dimensional hard sphere system, both of them confined by walls, and where wall excess free energies were sampled [98]. These results are shown in Section 2.9. In this case, the phase switch method could not have been used at all and the thermodynamic integration method proved to be useful.

When applying the Schmid-Schilling method to the soft two-dimensional colloidal crystal we are studying here, a few things have to be taken into account. A first question that arises when implementing the method is which choice of λ_1 is most efficient. As λ_1 describes the strength of the potential wells in the intermediate model, where the interaction between the particles *and* the pinning potential are acting on the particles, a large value of λ_1 means that the particles hardly move. This is advanta-

geous for that part of the Schmid-Schilling method where the particle interactions are turned on and off several times during one simulation run in order to estimate the free energy difference between the intermediate state and the reference state. Switching these interactions on would be very difficult if the particles were sitting very close together as the potential which is attempted to be switched on is purely repulsive. It is therefore better if the particles are sitting very close to their reference positions where they are distributed with larger distances between each other.

On the other hand, a large value of λ_1 means that the thermodynamic integration connecting this intermediate model to the target state whose free energy we are trying to compute will have to cover a large range as it integrates from $\lambda' = \lambda_1$ to $\lambda' = 0$, switching off the potential wells until only the particle-particle-interactions are left.

For our present model we chose a value of $\lambda_1 = 100$ as this rather large value ensures that the particles hardly move. It was still rather complicated to switch on the interparticle interactions as the potential is strongly repulsive. We therefore had to use the trick suggested in [5] and divide the process of switching the particle interactions on and off into several steps. For this particular model we used 100 steps of increasing/decreasing the interaction parameter η from $\eta_0 = 0$ (no particle-particle interactions, only potential wells) to $\eta_{100} = 1$ (particle interactions fully implemented). We used a scheme similar to successive umbrella sampling [70] here: As we can write

$$\begin{aligned} \Delta F_2 &= F(\eta_{100} = 1,\ \lambda_1) - F(\eta_0 = 0,\ \lambda_1) \\ &= -k_b T \ln(P(\eta_{100} = 1)/P(\eta_0 = 0)) \\ &= \sum_{i=0}^{99} -k_b T \ln(P(\eta_{i+1})/P(\eta_i)) \end{aligned} \tag{2.17}$$

we only had to sample the probabilities $(P(\eta_{i+1})/P(\eta_i)$ by restricting the simulation to each pair of successive values η_i and η_{i+1}. Although switching the particle interactions further on always led to an increase of the internal energy (as the potential is purely repulsive), these steps were small enough to be accepted via the usual Metropolis criterion.

Another question that might occur is how to choose the reference state of the system. As the main feature of the Schmid-Schilling method is that this reference configuration can be an arbitrary disordered configuration, any state belonging to the desired phase of the system is valid. Nevertheless, the simulations are more efficient if the particles in the reference configurations are distributed in a way that maximizes their distances to each other, as this makes it easier to switch the particle potential on. It is therefore preferable, for example, to use a perfect crystalline lattice instead of an equilibrated one which belongs to the same crystalline phase. In our specific case, however, we did not deal with perfect crystalline structures, but with defectuous ones

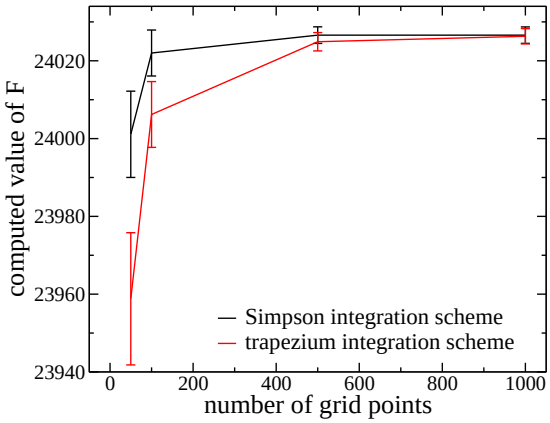

Figure 2.4: The impact of the number of grid points chosen for the thermodynamic integration on the computed value of F. Simulations were carried out at $\Delta = 2.0$ for a system starting off with 29 rows.

which were put between walls that were a distance D apart which was incommensurate with the crystalline structure. Therefore, we let the structure relax into the given misfit by equilibrating it. We used 10 independently equilibrated reference configurations (and made 5 simulation runs with each of them) for each value of the misfit, and averaged over the results (see Sec 2.5).

Turning to the thermodynamic integration part of the Schmid-Schilling method, it is important to ensure that the system does not undergo a phase transition on the path connecting the chosen reference state with the target state. But as we created our reference state by equilibrating the target structure, such a phase transition could hardly occur.

A possible problem in thermodynamic integration is, however, to ensure that enough grid points are chosen and that the system is equilibrated long enough in each of these points for the simulation to yield the correct value. Fig. 2.4 illustrates how the number of grid points influences the result. Additionally, we have compared two integration schemes, the "trapezium" integration where the data points are simply connected by lines in order to integrate the area below them, and the "simpson" integration method where quadratic curves are fitted to the values computed at the grid points in order to integrate the area under a smoother (and thus more realistic) curve. As the result does not differ significantly any more (within the range of the errors) for 500 or 1000 grid points, and not even for the two integration methods at 1000 grid points, we choose to use 1000 steps for the variable λ in the thermodynamic integration.

But just as important as the choice of enough grid points is checking that the simulation is equilibrated on each grid point of the thermodynamic integration long enough. One way of ensuring this is to compare curves in which λ has been gradually switched on with curves in which it has gradually been switched off. If there is no hysteresis visible any more (and these two integration directions therefore yield the

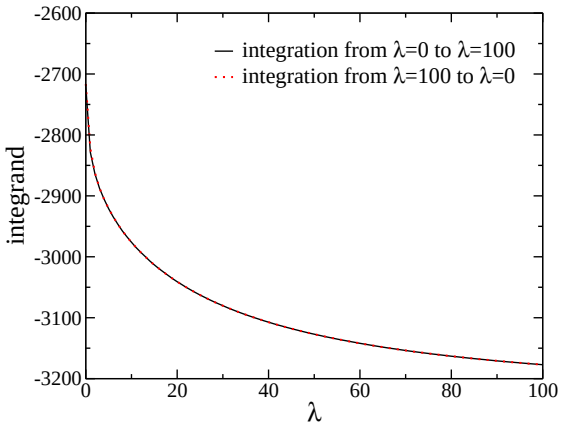

Figure 2.5: Comparison between different directions of the thermodynamic integration in order to ensure that the system has been equilibrated well enough at each grid point and that therefore the direction of the integration does not effect the resulting curve. Simulations were carried out at $\Delta = 2.0$ for a system starting off with 29 rows.

same result), the simulation has run long enough as was the case for our simulations as we show in Fig. 2.5. A thorough equilibration is especially important for simulations at those values of Δ where structural transitions occur.

An implementation of the "smart moves" suggested in [4] was fortunately not necessary for our particular system. These "smart moves" aim – similar to the special moves for liquid systems in the phase switch method – at bringing particles closer to their reference sites when they have left their potential well. As our system is not in a liquid state, but is "only" a soft crystal and we chose a cutoff radius of $r_{cutoff} = 0.5$ for the potential wells, the particles almost never left these wells in the course of our simulations, and if, then they stayed very close by and drifted back into them (as the potential wells are attractive) without the need of additional Monte Carlo moves promoting this.

But of course, we had to implement identity swap moves as it would interfere with the indistinguishability of the particles not to do so. As a side effect, these identity swaps also extinguished the problems we encountered with the phase switch method when rings of particles made a coordinated movement, each of them jumping onto its neighbour's lattice site.

As a last comment, we would like to stress that the Schmid-Schilling method produces results with an astonishing accuracy even if it is outperformed by the phase switch method in our particular case by several orders of magnitude. Yet, taking into account that both contributions to the calculated free energy ΔF_1 and ΔF_2 were of the order of 10^5 (with different preceding signs) and also the contribution F_{ref} is of the order of 10^4 (but does of course not contribute to the error bars as it is exact), the fact that the free energy $F = F_{\mathrm{ref}} + \Delta F_1 + \Delta F_2$ of each of the phases (with 29 resp. 30 rows) was accurate enough for the free energy difference between these phases (which is of the order of 10) to exhibit the slope which we will show in Sec. 2.5, is a proof of the really high accuracy of this method. Additionally, it might have

been possible to increase the accuracy (or alternatively reduce the necessary amount of CPU time) by choosing a steeper pinning potential $\phi(x)$, which would have pushed the particles closer to the center of their pinning sites and thus would have reduced the energy barrier between switching the interparticle potentials on and off.

2.4 Details of the simulation

The model system used in this chapter is the one described in Sec. 1.1. We again consider monodisperse colloidal particles in a strictly two-dimensional geometry, which then are treated like point particles in a plane interacting with a purely repulsive effective potential $V(r)$. Structured walls are confining the crystalline system in the y-direction, while periodic boundary conditions are applied in the x-direction.

In this chapter we will focus on the effect of placing the walls closer together and thus introducing a misfit Δ into the crystalline structure. As we have described at length in Sec. 1.1, introducing a misfit leads to a structural transition in the number of rows and the creation of solitons. The transition from the initial $n_y = 30$ rows to $n_y - 1 = 29$ rows was investigated by Chui et al [1–3] by computing the stress anisotropy. In this case, the $n_x = 108$ particles of the row that has disappeared (for the system comprised of $N = 3672$ particles which we are considering in this chapter) have to distribute themselves in the remaining rows and preferrably create a soliton staircase where 4 solitons are created next to each wall.

We have extended this investigation to stronger misfits, where another structural transition occurs and the system rearranged itself into $n_y - 2 = 28$ rows, see Fig. 2.6. Albeit, the stress anisotropy exhibits a large hysteresis which obscures the exact location of the transition. We have therefore applied the two methods for calculating free energies respectively free energy differences which have been described in the previous sections. But these methods require reference configurations which represent the phases for which the free energy is to be determined. In our case, this means that typical configurations with $n_y - 1 = 29$ and $n_y - 2 = 28$ rows and appropriate soliton patterns had to be created. One method of obtaining these configurations is by running a simulation at a misfit where the structure will spontaneously rearrange itself into the desired number of rows.

In practice, the actual structure having $n_y - 1 = 29$ rows that is formed in the simulations on increasing the misfit Δ beyond the critical value $\Delta_c \approx 2.0$, is generally less regular than the 'idealized' one suggested by Chui et al (shown in Fig. 1.4). Specifically, the relative distance between neighboring solitons showed a considerable variation. This comes about because (i) the solitons are formed from the stressed

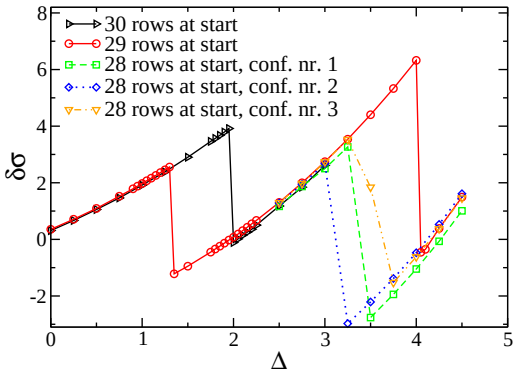

Figure 2.6: Stress anisotropy $\delta\sigma$ plotted vs. misfit Δ, for a system of $N = 3240$ particles, and using different starting configurations having $n_y = 30$, $n_y = 29$, and $n_y = 28$, as indicated in the figure. Note the huge hysteresis of the $n_y = 30 \rightarrow n_y = 29$ and $n_y = 29 \rightarrow n_y = 28$ transitions. For further explanations see the main text.

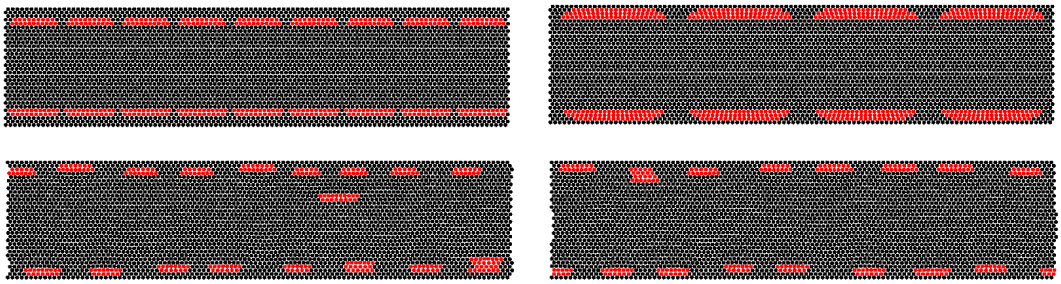

Figure 2.7: Configurations with $N = 3240$ particles and $n_y - 2 = 28$ rows, but different configurations of the solitons. In the text, they are referenced as "configuration nr. 1, 2, 3, 4" from top to bottom. For a clear identification of the positions of the solitons, the method described in [3] was used.

crystal with $n_y = 30$ rows via random defect nucleation events [2], and (ii) the mutual interaction between neighboring solitons, which is the thermodynamic driving force towards a regular soliton arrangement, is very small [3]. It is therefore reasonable to construct "by hand" the expected regular structure of 4 solitons near each wall as a starting configuration for a system with 29 rows, which can subsequently be equilibrated [1]. Of course, there is no guarantee that this guessed structure actually is the one with the lowest free energy; but it does exhibit slightly less stress than all other structures that had been tested, for misfits in the range $1.5 \leq \Delta \leq 3$, and hence has been used as a starting point for studies in which Δ was varied in this range.

A similar picture arises if one starts out from the 29 row structure but increases the misfit beyond $\Delta = 3$. As Fig. 2.6 shows, a transition occurs to structures with $n_y - 2 = 28$ rows (at about $\Delta \approx 4.1$). Unfortunately, there seem to be no unique candidates for stable structures having $n_y - 2 = 28$. Fig. 2.7 displays four candidate structures that we have identified, each of which is at least metastable on simulation timescales. Depending on which of these 28 row candidates one takes, the transition

from 28 to 29 rows on reducing the misfit occurs at anything between $\Delta = 3.2$ and 3.75. As regards the nature of the candidate structures, in each case $2n_x = 216$ extra particles have to be distributed across the system. If we again keep the rows adjacent to the walls free of extra particles, the particle number per inner row becomes $n'_x = n_x + 2n_x/(n_y - 4) \approx n_x + 8.3$, i.e. is non-integer. If we kept two rows adjacent to the wall rows free of extra particles, we would have 9 extra particles per row, and thus this structure has been tried (this is configuration number 1 in Fig. 2.7). Another structure was obtained if we place 4 extra particles in the rows directly adjacent to the walls and 8 extra particles in each of the 26 inner rows (configuration number 2). By energy minimization of a somewhat disordered structure resulting from a transition from 29 to 28 rows a structure was obtained which had 9 solitons on one wall but only 8 on the other wall (configuration number 3). Finally another configuration with 8 solitons on each wall (configuration number 4) was found. Note that the configurations shown in Fig. 2.7 are not the actual structures at $T = 1.0$ but the corresponding "inherent structures" found from the actual structures by cooling to $T = 0$, to clearly display where the solitons occur. Clearly, it again is a problem to (i) identify which of these 4 configurations with 28 rows is the stable one (at $T = 1.0$), and (ii) determine at which misfit the transition to the structure with 29 rows occurs. As we shall demonstrate below, both problems can be elegantly dealt with by employing the phase switch Monte Carlo method.

2.5 Free energy differences and computational efficiency

Fig. 2.8a shows the absolute free energies in the NVT ensemble for the phase with 30 rows (and no defects) and the phase with 29 rows and the "soliton staircases" (Fig. 1.4) as a function of the misfit Δ, as obtained from the thermodynamic integration method (Sec. III.1). One sees that these free energies are very large (note the ordinate scale) and vary rather strongly with Δ. However, the free energy curves with these two structures are barely distinct from each other, and hence a very substantial computational effort is needed to locate, with meaningful accuracy, the intersection point marking the equilibrium transition between $n = 30$ and $n = 29$ rows.

Fig. 2.8b plots the free energy difference ΔF versus the misfit, comparing the results from the thermodynamic integration method (points with error bars) with the results from the phase switch method, and focusing on the region near the transition. One can see that within the errors the results of both methods agree very well with each other, although for the thermodynamic integration method the error is at least

an order of magnitude larger than that of the phase switch method. We note that the predicted equilibrium value of the misfit at the transition point ($\Delta_t \approx 1.7$) falls well within the hysteresis loop of Fig. 2.6.

Since the absolute free energies are of the order of 20000 (for our system with $N = 3240$ particles) but, in the region of interest, free energy differences are only of order ± 40, the relative error $\delta F/F$ is of order $1/500$. Thus for thermodynamic integration, it would be difficult to bring the error bars down further in Fig. 2.8b. The error bars for the phase switch simulation were computed from the results of four independent runs for each value of the misfit, and are hardly visible on the scale of Fig. 2.8b.

In addition to this significant difference with respect to the size of the statistical errors, phase switch Monte Carlo also outperformed the thermodynamic integration method with respect to the necessary investment of computer resources. In order to obtain a suitable weight function for our system, at a certain value of the misfit, we let the simulation run for about 15 million steps (each step consisting of one sweep of local moves and one attempt to switch the phases). On the ZDV cluster of the University of Mainz, this takes about 4.5 days on a single core (though in hindsight we could have got away with a less smooth weight function, further reducing the computing time of this step). Having determined the weight function, we initiated four production runs for every value of the misfit. These runs needed again 10 million steps each (i.e. about 3 days each) in order to perform a sufficient number of phase switches to yield results of the desired precision. Overall, then, computing each point of the free energy difference curve of Fig. 2.8b by phase switch took about 16.5 days of CPU time.

In contrast to this, the thermodynamic integration method required a calculation not only of the free energy difference in which we are interested, but of the free energy difference along the path of the thermodynamic integration, gradually switching off the wells of attraction used there, and of the free energy difference between the state where the particle interactions were turned on and the state where they were turned off. This needs to be done for both phases separately. It is therefore not surprising, that considerably more CPU time was needed: roughly 250 days of CPU time were invested for each phase and for each value of the misfit to obtain the absolute free energy (again converting units to a single core). Thus, each of the 12 values of free energy differences needed for Fig. 2.8b required 500 days (rather than 16.5 days), i.e. a factor of 30 more computational effort! However, if we were to bring the statistical errors of the thermodynamic integration method a factor of 10 down (to make it comparable to the phase switch method), we would need another factor of 100 in computer time; the benefit of using the (clearly much more powerful) phase switch approach hence amounts to a gain of the order of 10^3 in computational resources!

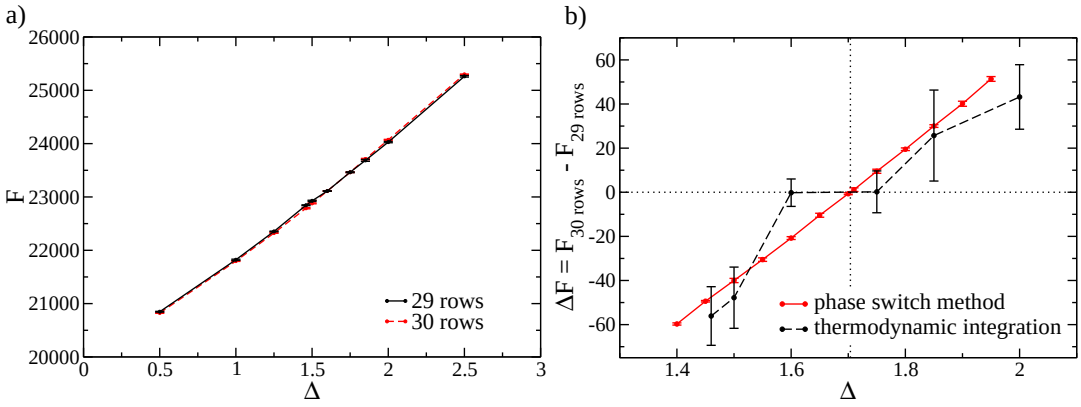

Figure 2.8: a) Absolute free energy F of systems of $N = 3240$ particles interacting with the potential given in Eq. (1.1) in $L \times D$ geometry with $L = 108a$, a being the lattice spacing, and periodic boundaries in x-direction, confined by two rows of fixed particles on either side in y-direction (Fig. 1.1, as a function of the misfit Δ (Eq. (1.4)). Two structures are compared: (i) a (compressed) triangular lattice with $n_y = 30$ rows containing $n_x = 108$ particles per row; (ii) a lattice with $n_y = 29$ rows and corresponding soliton staircases (Fig. 1.4).
b) Free energy differences between structures with 29 and 30 rows plotted versus the misfit Δ. Both results obtained from thermodynamic integration and from the phase switch method are shown, as indicated.

Of course, this is no surprise when we remember that the free energy differences of interest are only of the order of (1/500) of the total free energies for the present model system.

2.6 Ensemble inequivalence

We turn now to a discussion of a puzzling aspect of the physics, namely the fact that we treat here a first-order structural phase transition obtained by variation of the distance D between the walls formed by the rigidly fixed particles, i.e. an *extensive* rather than an *intensive* thermodynamic variable. If we were concerned with the study of a vapor to liquid transition of a fluid in such a geometry, the proper way to locate a discontinuous transition is the variation of the intensive variable thermodynamically conjugate to D, which is the normal pressure p_N (force per area acting on the walls; in the following the index N will be omitted. Of course, at fixed lateral dimensions L a variation of D is equivalent to a variation of the volume V).

To fix ideas, we remind the reader about this classical vapor-liquid problem in Fig. 2.9a: In the NpT ensemble, we would have a jump in volume $V = LD$ from $V_v = LD_v$ (density of the vapor $\rho_v = N/V_v$) to $V_\ell = LD_\ell$ (density of the liquid $\rho_\ell = N/V_\ell$) at the transition pressure p_t. If we work in the conjugate NVT ensemble, of course, the behavior simply follows from a Legendre transform, the volume jump from V_v to V_ℓ translates into a horizontal plateau at $p = p_t$, and any state of this plateau is a situation of two-phase coexistence, as schematically indicated in Fig. 2.9a.

Of course, it is also possible to consider the present transition between a state of n rows to $n-1$ rows in the NpT ensemble (Fig. 2.9b and Fig. 2.10c). Then it is clear that the transition will show up as a jump in the thickness D from $D_n(= na_n)$ to $D_{n-1}\,(= (n-1)a_{n-1})$, where a_n, a_{n-1} are the (average) distances between the lattice rows (or lattice planes, in three dimensional films, respectively). The corresponding phases of the n-layer state and $(n-1)$ layer state are indicated below the isotherm in the $(p-D)$ plane schematically.

However, one simply cannot construct a state of two-phase coexistence out of these two "pure phases" at a value of D intermediate between D_{n-1} and D_n: locally the n-layer state requires a thickness D_n, the $(n-1)$ layer state a thickness D_{n-1}, so one would have to "break" the walls. Of course, it is not just sufficient to have a state with n layers separated by a grain boundary from a state with $(n-1)$ layers at the same value of D: these domains are *not* the coexisting pure phases in the NpT ensemble!

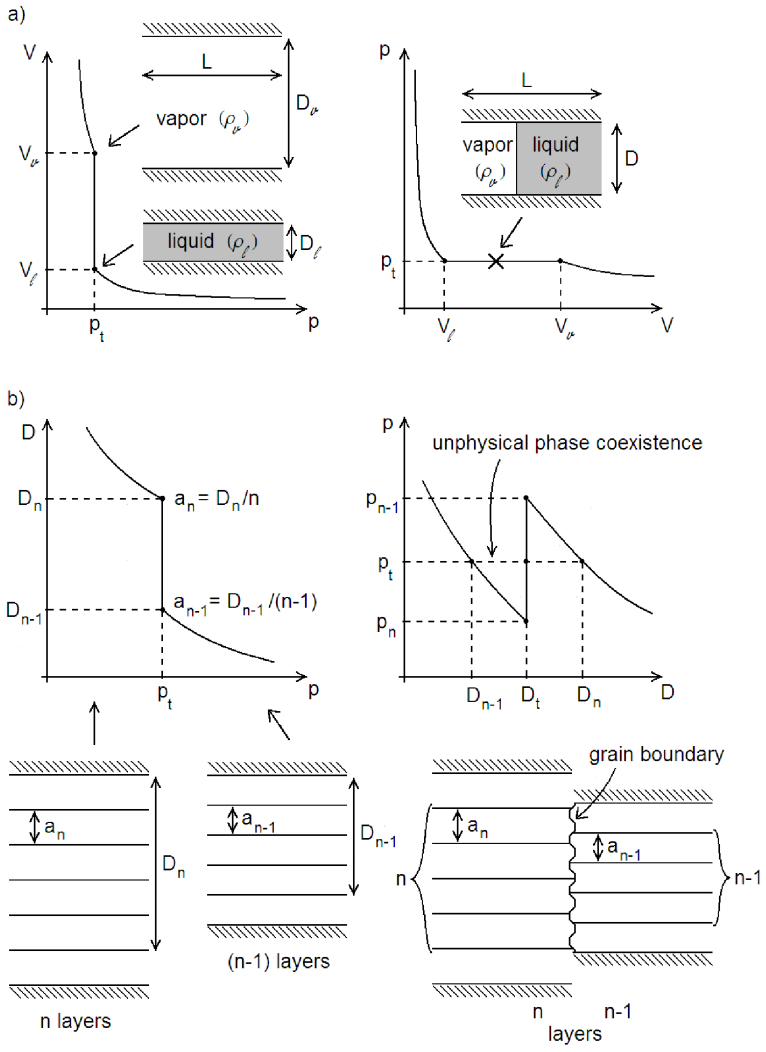

Figure 2.9: Schematic description of phase transitions in thin films of thickness D in the conjugate NpT (left) and NVT (right) ensembles, for the case of a vapor to liquid transition (a) and the present transition where the number of rows is reduced $(n \rightarrow n-1)$ when either the (normal) pressure p increases (left) or the thickness decreases (right). Note that in the latter case two-phase coexistence is possible for the vapor-liquid transition, but not for the transition where the number of rows parallel to the boundaries change. For further explanations cf text.

So the phase coexistence drawn (horizontal broken curve) in Fig. 2.9b is unphysical, it requires a state where the constraining walls were broken. Requesting the integrity of the walls is a global constraint which makes phase coexistence in the standard sense impossible for the present transitions! Thus, the rule that the different ensembles of statistical mechanics yield equivalent results in the thermodynamic limit is not true for the present system; in the transition region $D_{n-1} < D < D_n$ the NVT ensemble and the NpT ensemble are *not equivalent*.

Actually this is not the first time that such an ensemble inequivalence has been pointed out. A case much discussed in the literature is the "escape transition" of a single polymer chain of N beads grafted at a planar surface underneath a piston held at a distance D above the surface to compress the polymer [99–105]. For pressures $p < p_t$ (where the piston is at distance $D_{t,1}$) the chain is completely confined underneath the piston (which has the cross section of a circle in the directions parallel to the surface) while for $p > p_t$ the chain is (partially) escaped into the region outside of where the piston acts (the piston distance at p_t jumps to a smaller value $D_{t,2}$). When we use instead D as the control variable, again a sharp transition occurs (for $N \to \infty$) at some intermediate value D_t ($D_{t,2} < D_t < D_{t,1}$), since obviously it is simply inconceivable to have within a single chain phase coexistence between states "partially escaped" and "fully confined", since these states are only defined via a global description of the whole polymer chain.

Another case where transitions of the number n of layers in layered structures in thin films occurs is the confinement of symmetric block copolymer melts (which may form a lamellar mesophase of period λ_0 in the bulk) in thin films between identical walls [106–109]. When then the thickness D of such films is varied, one observes experimentally discontinuous transitions in the number n of lamellae parallel to the film [107, 108]. However, when one considers block copolymer films on a substrate and does not impose the constraint of a uniform thickness but rather allows the upper surface to be free, then indeed mixed phase configurations of a region where $n-1$ layers occur (and take a thickness D_{n-1}) and of a region where n layers occur (and take a thickness D_n) are conceivable [109] and have been observed, see e.g. [110]. In summary of these remarks, we note that it is not uncommon that global geometric constraints may destroy the possibility of phase coexistence.

In view of the above discussion, it is of interest also in the present case to investigate the use of the (normal) pressure p (instead of the strip width D) as the control variable. Taking, in the spirit of the general remarks on the phase switch method, the appropriate phase switch energy cost as an order parameter M, we can sample the probability distribution function $p(M)$ which exhibits two well separated peaks of generally different weights. These peaks are even more clearly visible in the distribution of the energy difference $p(E_{30rows} - E_{29rows})$ at fixed $\{\vec{u}\}$ as the or-

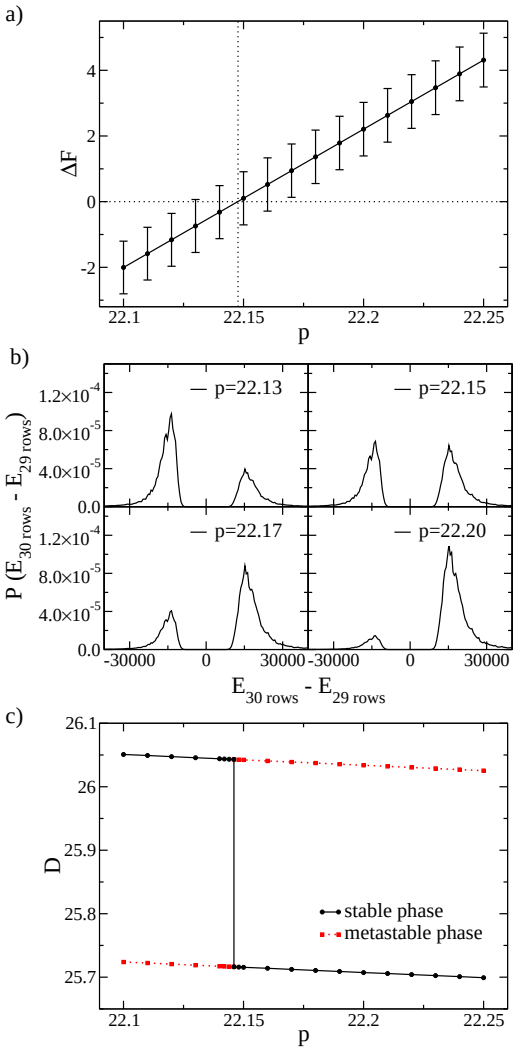

Figure 2.10: a) Free energy difference ΔF for the transition from $n = 30$ to $n = 29$ rows as a function of pressure. (b) The distribution of the internal energy difference between the two phases $p(E_{30rows} - E_{29rows})$ at fixed $\{\vec{u}\}$. Curves for 4 pressures near and at the transition pressure $p_t = 22.146 \pm 0.015$ are shown, as generated via histogram reweighting. The simulation was run at a pressure of $p = 22.13$. (c) System length D as a function of pressure. Clearly, the curve for the stable phase exhibits a jump at the transition pressure. Statistical errors are smaller than the symbol sizes.

der parameter M is related to this energy difference via a logarithmic function (cf. eq. 2.2). The transition pressure p_t is that for which the peaks have equal weight (Fig. 2.10) and can be determined accurately via histogram reweighting. From this we estimate that $p_t = 22.146 \pm 0.015$. At the transition, the measured misfit Δ jumps from $\Delta_1 = 1.684 \pm 0.044$ (for $n = 30$) to $\Delta_2 = 1.323 \pm 0.046$ (for $n = 29$). Please note that there was an error in the values given in Ref. [27]: the misfit where the transition in the NVT ensemble occurs ($\Delta_t \approx 1.71$) is (using the correct values) *n*ot the average of these two values.

2.7 Comparison of competing stable candidate structures

Returning again to the NVT ensemble, we now consider the transition from states with 29 layers to states with 28 layers. We recall (Fig. 2.7) that several different candidate structures do exist, and it is not at all clear *a-priori*, which of them should be favored. Again, the phase switch Monte Carlo is a convenient tool to solve such a problem: we utilize reference states from all four of the candidate structures having $n = 28$ (as shown in Fig. 2.7) and calculate the free energy difference ΔF between the (unique) structure with $n = 29$ and these four candidates.

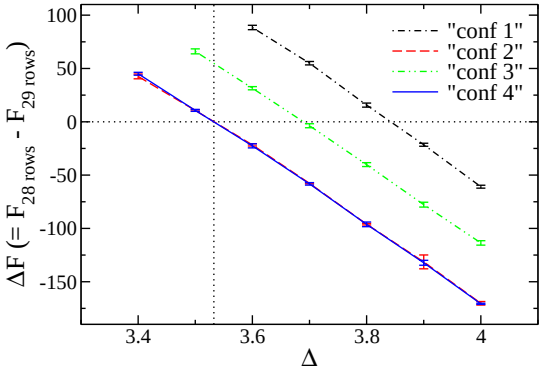

Figure 2.11: Free energy differences between various structures with $n = 28$ rows and the structure with $n = 29$ plotted vs. the misfit Δ. As configurations number 2 and number 4 turned out to be the same, their free energy curves fall on top of each other.

The results (Fig. 2.11) clearly show that configurations number 1 and number 3 are metastable, because they have distinctly higher free energy differences throughout the range of Δ than configurations number 2 and 4 which practically coincide. In fact, this coincidence between the free energies of configurations nr. 2 and 4 is not accidental: a closer evaluation of their time evolution shows that they transform into each other via sequences of "easy" local moves, and although the instantaneous snapshot pictures reproduced in Fig. 2.7 were different, they do not belong to different phases in a thermodynamic sense.

It is also interesting to note that the conclusion that structure number 2 is the stable one would not have been obtained by a simply comparison of the internal energies of the four structures: indeed configuration number 2 has the highest energy of all four structures.

Thus, entropy matters in soft crystals, such as those studied here.

2.8 Concluding remarks

The principle findings of our study are two-fold: (i) We have performed a thorough test of the suitability of the phase switch Monte Carlo method for the task of determining the relative stability of imperfectly ordered structures of typical soft-matter systems, where one must deal with systems which have at least one very large linear dimension. For such a test, it is crucial to provide full information on the model that is studied, and to give a careful description of the method and its implementation. Moreover we have studied precisely the same model system by a thermodynamic integration method thereby allowing the first like-for-like comparison between the two approaches. We find that the results from both methods are compatible, but the accuracy that can be achieved using phase switch MC is at least an order of magnitude better (Fig. 2.8b), despite requiring a factor of 30 less computational time.

The reasons for this efficiency gain can be appreciated from a glance at Fig. 2.8a: the absolute free energies of our system of 3240 particles vary from about 22000 to 24000 (in suitably scaled units), for a misfit parameter Δ varying from 1 to 2, while the free energy difference between the two states that we wish to compare vary only from -60 to $+60$ in the same range. These numbers illustrate vividly the basic concept of phase switch Monte Carlo: one does better in focusing directly on the small free energy difference between the states that one wishes to compare, rather than extracting them indirectly by subtracting two measurements of large absolute free energies. Thus (in the present context at least) phase switch Monte Carlo seems a much more powerful approach than thermodynamic integration. In fact, if one were to try to bring the errors of the thermodynamic integration method down by an order of magnitude – to make the error bars of both methods in Fig. 2.8b comparable – one would have to invest a factor of 3000 more computational time. We feel that the case of relatively small free energy differences between competing phases and/or structures is rather typical for soft matter systems. Indeed for many soft matter systems, such as block copolymer mesophases, the relative magnitude of free energy differences is much less than the factor of about $1/500$ encountered here, and hence such problems could never be tackled successfully with thermodynamic integration methods since

the computational effort to reach the requisite accuracy would be prohibitive.

The first problem to which phase switch Monte Carlo was applied (in the form of the "Lattice-switch" method), evaluated the free energy difference of perfectly ordered face-centered cubic and hexagonal close packed crystals. Such an application might be regarded as a somewhat special case due to the perfect long-range order in these defect-free crystals. However, the present work shows that the method can equally be applied to imperfectly ordered crystals. Here, due to the confinement by structured walls together with a misfit between the distance between the walls and the appropriate multiple of the distance between the lattice rows, somewhat irregular long range defect structures form along the walls ("soliton staircase"). Additionally several similarly ill-crystallized structures can present themselves as candidates for the optimal structure (Fig. 2.7). It would be absolutely impossible to identify which is the equilibrium structure and which structures are only metastable without the phase switch Monte Carlo method (Fig. 2.11).

(ii) Our second main finding is that this type of system has an interesting physical property, namely the inequivalence between conjugate ensembles of statistical mechanics. When we fix the distance D between the confining "walls", the total particle number N and the total (two-dimensional) "volume" V of the system, we realize the NVT ensemble. When one studies first order transitions in the bulk using such an ensemble containing two extensive variables (N, V), a first order transition normally shows up as a two-phase coexistence region (e.g., at fixed N the two-phase coexistence extends from V_I to V_{II}). However, here such a two-phase coexistence is not possible (Fig. 2.9), and thus one has the unusual behaviour that at the equilibrium in the "constant D"-ensemble the conjugate intensive variable (the normal pressure p_N, as well as the stress anisotropy $\delta\sigma$, cf. Fig. 2.6) exhibit jumps (in Fig. 2.6, we display the hysteresis loops, but the positions of the jumps in equilibrium can be inferred from $\Delta F = 0$ in Figs. 2.8b and 2.11, respectively). When we use a "constant p"-ensemble (which is physically reasonable if the confinement of the crystal is effected mechanically in a Surface Force Apparatus), it is the "volume" (i.e., the distance between the walls D) which jumps from D_I to D_{II} at a well-defined transition pressure, cf. Figs. 2.9, 2.10.

One should not confuse this ensemble inequivalence with the well-known ensemble inequivalence between NVT and NpT ensembles in systems where N is finite: in the latter case, the ensemble inequivalence is dominated by interfacial contributions (in the NVT-ensemble, when $V_I < V < V_{II}$, the system is in a two-phase configuration, as suggested for $V \to \infty$ by the "lever rule", but for finite V the relative contribution due to the interface between the coexisting phases dominate the finite size effects). But for $V \to \infty$ these interfacial effects become negligible, the properties in the two conjugate ensembles are just related by the appropriate Legendre

transformation. This equivalence between the ensembles holds also for liquid-vapor or liquid-liquid unmixing under confinement in a thin film geometry: when D is finite and the particle number $N \to \infty$, i.e. the lateral linear dimensions become macroscopic, we still have ordinary two-phase coexistence in the thin films (cf. Fig. 2.9). The ensemble inequivalence in the present system arises from the lack of commensurability between the thickness D of the slit and the appropriate multiple of the lattice distance. At a transition pressure p_t in the NpT ensemble we inevitably have different distances D_I, D_{II} between the walls for the two phases I, II. Thus, they cannot coexist for any uniform value of D. Similar phenomena (where the number of layers of a layered lamellar structure confined between walls exhibits jump discontinuities when D is varied) are already known, both experimentally and theoretically, for block copolymer mesophases, but the aspect of ensemble inequivalence has not been addressed, to our knowledge, in these systems studied here.

2.9 Addendum: Determining interfacial tension using the Schmid-Schilling method

While we have demonstrated in the previous sections that the phase switch method is more suitable for the determination of free energy differences between various crystalline structures, there are –of course– also cases where the absolute free energy needs to be known and the thermodynamic integration method by Schmid and Schilling [4, 5] can be used. One such example is the computation of surface or interface free energies, which we will describe in this section.

The basic idea is here to consider crystals of different sizes, but with the same interface area. For example, in the case of a two-dimensional colloidal crystal, one might use walls in the y-direction (which create an interface with the crystalline structure) and consider crystals of different numbers of rows N_R in the y-direction, but with a constant length L_x of the walls (see Fig. 2.12). All of these crystals thus have the same interface free energy. Additionally, there is a contribution to the free energy which scales with the number of particles respectively with the thickness of the crystal (we only consider ideal lattice structures with constant densities here). Thus, the free energy can be written as

$$F = F_{bulk} + 2 \cdot \gamma \cdot L_x \tag{2.18}$$

where γ is the interfacial tension between the colloidal particles and the wall and the factor 2 is due to the fact there there are two walls. F_{bulk} is proportional to the number of particles N and thus to the number of rows N_R as $N = N_R \cdot N_x$. Therefore we can write:

$$\frac{F}{N} = \frac{F_{bulk}}{N} + \frac{2 \cdot \gamma \cdot L_x}{N_x \cdot N_R} \tag{2.19}$$

and plotting $\frac{F}{N}$ versus $1/N_R$ yields a straight line where $\frac{F_{bulk}}{N}$ can be read off as the intersection of the curve with the y-axis as it is independent of the system size, while $\frac{2\gamma L_x}{N_x}$ is given by the slope. From the latter, γ can be determined. Calculating the absolute free energy of these crystals therefore yields an estimate of the interfacial free energy.

In this case we do not use structured walls consisting of frozen particles, because the interfacial tension between such walls and the commensurate crystalline structure of the same hexagonal lattice geometry is extremely small. Instead, we are using planar walls with a Lennard-Jones potential

$$V(r) = 4\epsilon \left[\left(\frac{\sigma}{r}\right)^{12} - \left(\frac{\sigma}{r}\right)^{6} \right] \tag{2.20}$$

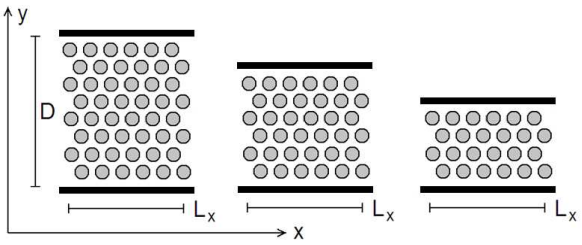

Figure 2.12: Sketch of differently sized crystals with the same interface "area" $2 \cdot L_x$ and planar walls.

with $\sigma = 1$. The ϵ-parameter was optimized in such a way that at a given density $\rho = N/(L_x \cdot D)$ –$D = N_R \cdot \frac{\sqrt{3}}{2}a$ being the distance between the walls– the distance between the walls and the first crystalline row was as large as the distances between the crystalline rows $\frac{\sqrt{3}}{2}a$ in order to ensure that the crystal was not compressed.

As planar walls cannot stabilize the crystalline structure in the way structured walls do, we had to increase the density in order to remain in the crystalline regime: Instead of $\rho = 1.05$ which we used in the rest of this thesis for the uncompressed case, we used $\rho = 1.30$ in order to obtain a Lindemann parameter of $p_{Lind} = 0.09$, which is below the threshhold for crystallinity defined as $p_{Lind} = 0.1$.

The results for the two-dimensional crystal with planar walls are shown in Fig. 2.13. As expected, the absolute free energy of the system as a whole increases with increasing number of rows (and therefore also proportionally increasing number of particles), but the free energy per particle decreases. The fit shown in Fig. 2.13 yielded $y = 11.9065 + 3.61236x$, i.e. $F_{bulk}/N = 11.9065$ and $\gamma = 1.9165$.

Of course, one can also determine the contribution of the walls to the free energy by carrying out a simulation of a crystal in the bulk and comparing it directly to the free energy of the same crystal when walls are implemented. This might lead to some finite size effects as the free energy difference between bulk systems and systems with walls might not only stem from the interfacial free energies, but the crystal might also be slightly compressed by the walls and its structure might become more disordered in the case without them. All of these additional effects will only vanish for large enough system sizes. And indeed we encountered some trouble for the smaller system sizes as these crystals proved to be rather instable without the walls (i.e. the Lindemann parameter was not below $p_{Lind} = 0.1$ any more for the system with 12 rows). Therefore we only used the bulk system with 30 rows for these simulations, where p_{Lind} was on average below 0.1 and the pair distribution function showed clear peaks (see Fig. 2.14). Here, we obtained a value for the bulk free energy of $F_{bulk}/N = 11.9048$ and for the interfacial tension of $\gamma = 1.9531$, which agrees very well with the values calculated above.

In order to compare this method of determining the interfacial tension with other

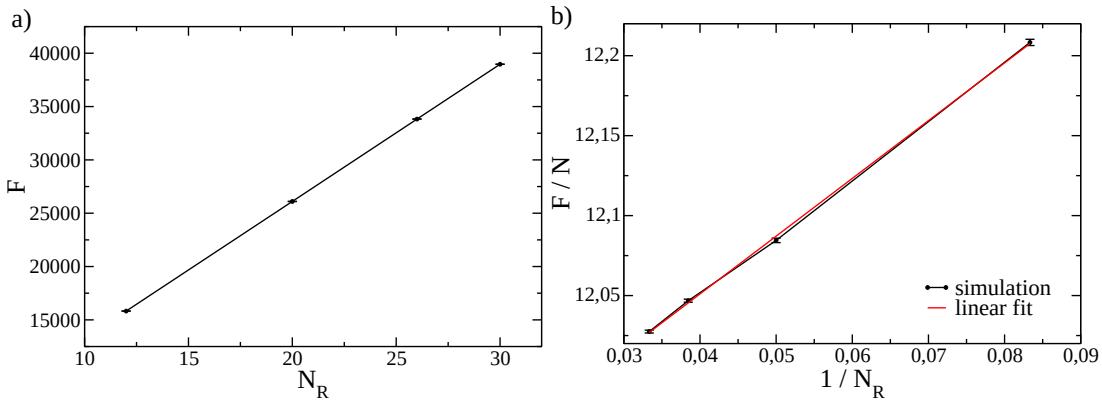

Figure 2.13: a) Absolute free energies F for crystals with the indicated number of rows N_R and planar walls. b) Free energy per particle F/N plotted against $1/N_R$ for the same systems. All simulations were carried out at $T = 1.0$ and $\rho = 1.30$.

methods, we have also implemented it for a three-dimensional system of hard spheres in a box confined by walls in one direction which interact with the spheres via a Weeks-Chandler-Andersen potential [165] of the form:

$$V_{WCA}(z) = 4\epsilon \left[\left(\frac{\sigma_w}{z}\right)^{12} - \left(\frac{\sigma_w}{z}\right)^{6} + 1/4 \right], \qquad 0 \leq z \leq (\sigma_w \cdot 2^{1/6}) \tag{2.21}$$

with parameters $\epsilon = 1$ and $\sigma_w = 1$. One has to note, however, that the wall potential is a soft potential, which means that the spheres can in principle approach the walls until the centers of the spheres touch the walls. We oriented the crystal in such a direction that the 111-layer was next to the walls.

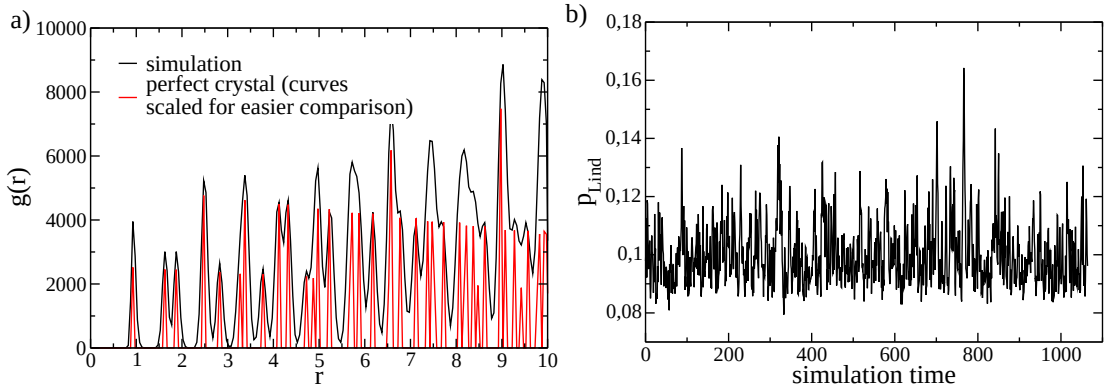

Figure 2.14: a) Pair distribution function $g(r)$ versus particle distance r and b) Lindemann parameter for a crystal with 30 rows in the bulk at $T = 1.0$ and $\rho = 1.30$.

When using the Schmid-Schilling method to compute the absolute free energy of such a hard sphere system of a certain thickness D, D being the distance between the walls, one has to use the equations given in Ref. [5] for the three-dimensional case (note the error in the formula given in Eq. (5) of Ref. [5]: the correct equation reads in this case $g_{linear}(a) = \frac{d!}{a^d}\left(e^a - \sum_{k=0}^{d}\frac{a^k}{k!}\right)$ where all parameters are defined as in Ref. [5]).

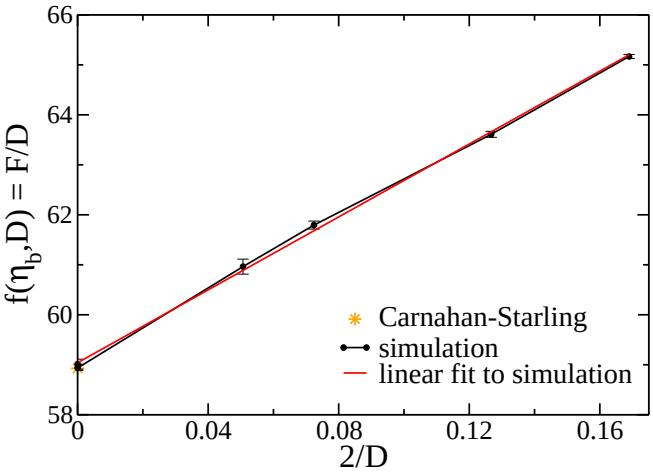

Figure 2.15: Absolute free energy F/D for a hard sphere fluid confined by WCA walls, which were placed a distance D apart from each other. Density $\eta = 0.3868$. The intercept at the ordinate is known exactly from the Carnahan-Starling equation.

When the contribution of switching the particle interactions on and off in the case of the intermediate system is being computed, one has to deal with the fact that the particles interact as hard spheres. Switching a hard sphere interaction on is a severe problem when the particles have moved for several steps without feeling any interactions, as the chances are high that at least some particles will at least slightly overlap, which would lead to a rejection of the switch-on-move. Thus, again one has to divide the process of switching the interaction on into several steps (we chose 100 steps), in which overlaps between particles are fined with an increasing energy barrier, until there are no overlaps any more and the hard sphere potential can finally be switched on in a last step.

We were able to reproduce the value given by the Carnahan-Starling equation of state for hard spheres by simulating a system in the bulk, which corresponds to the case of $D \to \infty$, where the walls would be placed infinitely far apart from each other. Running simulations with walls which were placed only a finite distance D apart from each other yielded the results shown in Fig. 2.15. The straight line can be fitted to the data points with high accuracy and the resulting value of $\gamma = 1.01 \pm 0.01$ is fully compatible with results obtained with different methods: In Ref. [111, 112] we have compared this method of obtaining the interfacial tension via thermodynamic integration with the "ensemble mixing method" where one gradually switches the walls on and of and with simulations where the interfacial tension is extracted from

the anisotropy of the pressure tensor. But as our simulations showed that the results of all three methods agree, but that especially the ensemble mixing method produces results of the same (or much better) accuracy in considerably less CPU time, we did not follow this particular approach much further. The reasons for this difference in accuracy respectively necessary CPU time are the same ones we observed before when comparing the thermodynamic integration method to the phase switch method: Again, the thermodynamic integration method yields the absolute free energies, while the ensemble mixing method is similar to the phase switch method in that it directly computes the free energy differences which we needed here. Thus, it is better suited to this particular problem.

Chapter 3

Motion and Diffusion mechanisms in colloidal crystals

We are currently preparing a publication on the basis of this chapter (Ref. [26]). The wording of this paper is probably going to be at least in parts similar to the one of this chapter.

In this chapter we will investigate the motion and diffusion of particles and solitons in colloidal crystals under confinement; in contrast to the previous chapter we will now study the dynamics of the system. Such colloidal systems have been extensively studied, as they are a very useful model system not only for statistical physics, but also for modelling nanotechnological devices and self-assembly processes. As we have described in Chapter 1, the great advantage of using colloids lies in the fact that they can be produced with tunable interactions, in different shapes and sizes, and that convenient techniques are available to observe their structure and dynamics [52, 113–116].

Therefore colloidal systems have been investigated under various external conditions both by experiment and simulation. Two-dimensional layers of colloids have been created [29, 33–37, 41–46], they have been confined mechanically or by laser fields [43, 46, 49, 117] and layers of colloids have been sheared observing soliton-like excitations, namely moving kinks and antikinks [118]. They have been used as a model system to study phase transitions [29–35, 119] and crystal nucleation in two-dimensional colloidal systems [37], and the crack formation in two-dimensional colloidal crystals has been studied [39]. They have been used to model the glass transition [45, 120]. Different boundary conditions [121] and the effect of incommensurate walls on colloidal crystals in two dimensions have been investigated by

simulations in which soliton formation was observed [1–3, 27].

But although colloidal systems under confinement have been extensively studied with various questions in mind, a thorough study of the basic motion of the particles and solitons and of the diffusion processes inside of colloidal crystals is still missing, and with this study we are attempting to fill this gap. We describe in our simulations the damping of oscillations of the particles due to solvent by carrying out a Langevin dynamics simulation (rather than microcanonical Molecular Dynamics), thereby ignoring hydrodynamic backflow effects, of course, but the latter should not be important for colloidal crystals in thermal equilibrium. Both perfect (defect-free) crystals and crystals containing solitons at the confining walls shall be studied.

In a crystal formed from atoms or small molecules, the dominating type of motion of all particles are small scale (somewhat damped) oscillating motions (due to thermally excited phonons); the amplitude of these motions can only be of the order of 10% of the nearest neighbor distance, or less, otherwise the crystal melts ("Lindemann criterion") [122]. In a colloidal crystal where micrometer-sized particles are suspended in a solvent, these lattice vibrations are overdamped by the random collisions with the solvent molecules, but with respect to the static mean square amplitude of particles, the behaviour is still analoguous to crystals formed from small particles.

Another important contribution to the movement within colloidal crystals is diffusion. The well-known theory of diffusion in crystals states that diffusion either takes place via vacancies or - in perfect crystals like the one we are studying here - via the formation of a hole and a corresponding interstitial particle. In this study we will show that in our model system diffusion also takes place by cooperative rotations of groups of particles.

Such cooperative rotation diffusion processes are known to play an important role in glassy materials [23]. In two-dimensional layers of crystals, such as surfaces, a variety of different diffusion mechanisms have been described: Most studies concentrate on hopping vacancies as the direct mechanism [123] or at least as the underlying principle mediating surface diffusion [124] and on the diffusion mechanism of so called "adatoms" which are atoms adsorbed on a surface [125–130] and on the questions how thermal vacancies are created and destroyed and which role the surface plays in this process [131].

But to our knowledge there are only two studies reporting on cooperative ring rotation processes: Using temperature-accelerated dynamics (TAD) [132, 133], Montalenti et al. have found evidence of such machanisms in a two-dimensional layer of crystalline atoms in a periodic potential [25] and in Cu grain boundaries [24], although they were extremely rare especially in the latter case. In this chapter we will show, that in our two-dimensional model system cooperative ring rotation phenomena

occured quite frequently and involved different numbers of particles.

In the next section we will describe details of the simulation. In Sec. 3.2 we will present our results for the motion of the particles in the case without solitons, during the equilibration into the defect structure (Sec. 3.3), and for the case where the transition has taken place. We will also investigate the motion of the solitons (Sec. 3.4). In Sec. 3.5 we will describe the diffusion mechanism which we have observed, and in Sec. 3.6 we will summarize our findings.

3.1 Details of the simulation

In this chapter, we will study the motion and diffusion of particles in a two-dimensional colloidal crystals by using the same model system as described in Sec. 1.1. So the particles are interacting via a purely repulsive potential and arrange themselves into an hexagonal crystalline lattice at the temperatures studied here. Walls are implemented in the y-direction and consist of two rows of frozen particles. As a reminder, the system geometry is shown in Fig. 3.1 again.

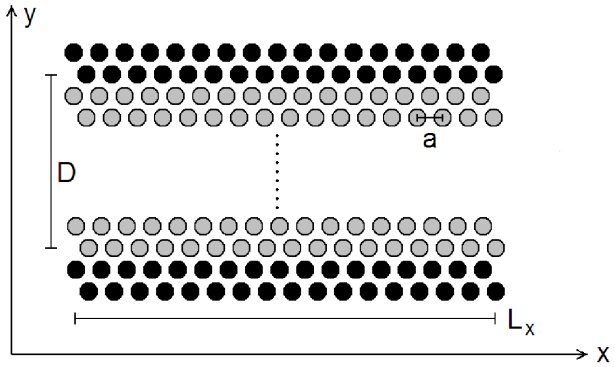

Figure 3.1: Sketch of the system geometry, showing the fixed wall particles (black spheres) and the mobile particles (gray spheres). The orientation of the coordinate axes is indicated, as well as the lattice spacing of the triangular lattice (a) and the linear dimensions L_x, D of the system.

Simulations are carried out at various values of the misfit (see definition of the misfit and its consequences for the crystalline structure in Sec. 1.2): At $\Delta = 0$ the system exhibits perfect crystalline order and is comprised of 30 rows of particles in the y-direction, while from $\Delta \approx 2.0$ onwards only the configuration consisting of 29 crystalline rows and the appropriate number of solitons is stable. Between $\Delta \approx 1.3$ and $\Delta \approx 2.0$, configurations with 29 rows as well as configurations with 30 rows are at least metastable.

The simulations are carried out using Langevin dynamics by applying the program package HooMD-blue [13, 14]. This program is designed to run on graphic cards, where due to the parallelization on the internal processing units large system

sizes can be used. Thus, most simulations were carried out using $M = 73440$ particles (including walls), i.e. 64800 mobile particles. However, graphic cards usually only use single precision, which proved to be not accurate enough for our system at temperatures $T < 1.0$ (see Appendix C). Therefore, we had to run the simulations at the lower temperatures on CPUs. As this led to a considerable increase in the computational times, we reduced the system size to $N = 3672$ particles including walls, i.e. 3240 mobile particles wherever possible when we had to run the simulations on CPUs.

The program HooMD-blue uses the well-known Velocity Verlet integration method (see also Sec. 1.3). In this integration scheme, a force $\vec{F} = -\gamma\vec{v} + \vec{F}_{rand}$ is added to the force exerted on each particle by the interaction with its neighbouring particles [60, 61]. Here, γ is a friction coefficient to be specified, $\vec{v}$ is the particle's velocity and $\vec{F}_{rand}$ is a random force with a magnitude chosen via the fluctuation-dissipation theorem to be consistent with the specified drag γ and the chosen temperature T. We used a time step of $\Delta t = 0.002$, a friction coefficient of $\gamma = 0.5$ (unless otherwise specified) and a temperature of $T = 1.0$ (unless otherwise specified). Note that our particles have mass $m = 1$, and that the time t is measured in the standard Molecular Dynamics time unit $\tau = t\sqrt{\frac{\epsilon}{m\sigma^2}}$.

All simulations were carried out below the melting temperature of $T_m = 1.35$ [1, 34, 52] for our chosen density of $\rho = 1.05$. As we have already discussed in Sec. 1.2 (compare also Fig. 1.2 shown there), the relative fluctuations are therefore –for all values of the temperature which we used here– clearly smaller than what would be expected near melting (from a Lindemann-type criterion). In the commensurate case, the confined crystal has an essentially defect-free triangular crystal structure.

3.2 Localized Motions of Particles Confined in "Cages" formed by their Neighbors

When the system starts out with 30 crystalline rows, $N = 64800$ mobile particles, and without misfit, we obtain the MSD with respect to the time difference $\mathrm{MSD}_{\text{time-diff}}$ for the particles in x- and y-direction shown in Fig. 3.2. Here, like in all graphs of this kind (unless otherwise stated), we printed out configurations after every 50 steps and averaged over 500 configurations. In the following we define one MD time unit by multiplying the number of integration steps with the time step $\Delta t = 0.002$. So one MD time unit corresponds to 500 integration steps. The starting configurations were equilibrated for $2 \cdot 10^6$ steps before the simulation runs were started. One can see an overshoot at small time scales. This is expected in a crystal as it is due to the repelling

forces which the particles experience when they are displaced from their ideal lattice position and thus come closer to their neighbouring particles. These forces act similar to a harmonic potential pinning particles to their lattice sites, therefore they cause this oscillatory behaviour in the MSD. But as the oscillation is strongly damped and modified by random kicks, only this overshoot is clearly visible. At slightly larger time scales, the MSD reaches a plateau. This plateau is also expected, because the structured walls are pinning the crystal (as a whole) to its position and do not allow any center-of-mass movement. Thus, the particles are localized near their equilibrium sites. One can also see that in y-direction the values are of the same order of magnitude as the crystal is not compressed. They do differ a bit, however, as it makes a difference whether there are fixed wall particles or periodic boundary conditions, of course.

If one studies the same MSDs at a misfit of $\Delta = 1.5$, where the transition to 29 rows has not taken place yet, the values are smaller as the system is compressed and less space is available to the particles (Fig. 3.3). Apart from this, the proximity of the transition does not show up in the MSDs.

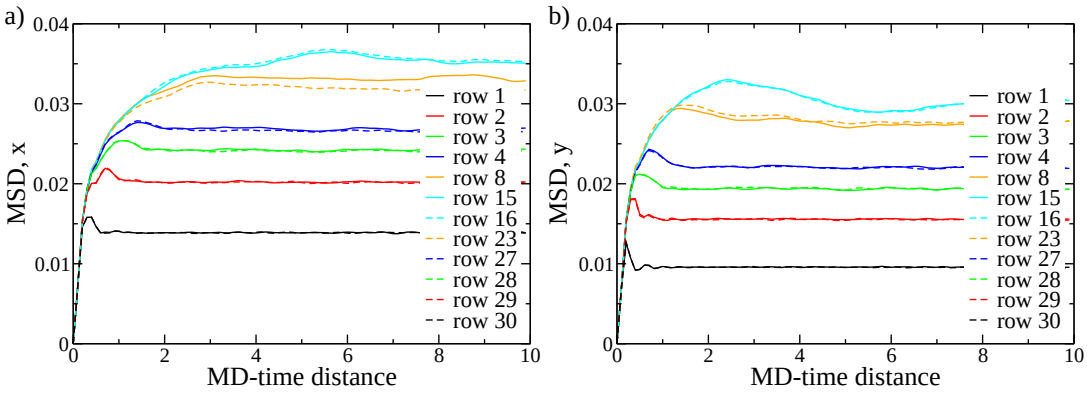

Figure 3.2: $\mathrm{MSD}_{\text{time-diff}}$ in x- (a) and y-direction (b) for a system with 30 rows without misfit. Due to the symmetry of the system, rows 1 and 30, 2 and 29 etc should on average yield the same curves. Temperature $T = 1.0$. Each MD-time unit corresponds to a difference of 500 integration steps as the time step was $\Delta t = 0.002$.

Note that the time-dependent mean-square displacements show in the inner rows (e.g. row 8 and 23, or 15 and 16, respectively) some flat maximum at time ≈ 2. While rows 15 and 16 are adjacent to each other, and hence motions of particles in these rows are strongly correlated to each other, rows 8 and 23 are rather remote from each other (they are only equivalent due to the symmetry of the system, since both corrugated walls are equivalent). Hence this particular feature of the MSD is not a consequence of insufficient averaging, but a real effect. It also is easily understand-

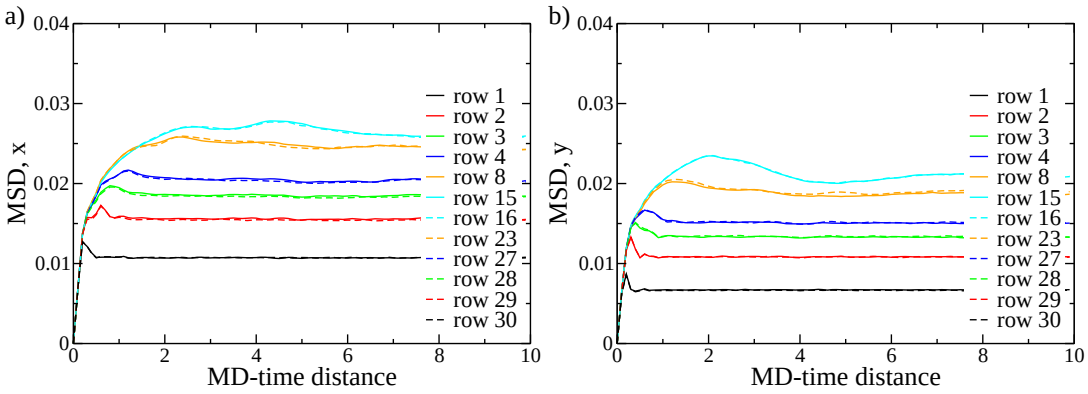

Figure 3.3: Same like Fig. 3.2, but for a system with 30 rows at a misfit of $\Delta = 1.5$, where the transition to 29 rows has not taken place yet.

able that the mean square displacements are larger in the center of the slit: due to the corrugated walls, all phonon-type excitations are constrained to have zero amplitude at the boundaries. A phonon with wavelength $\lambda/2 = D$ has then its maximum amplitude at $y = D/2$.

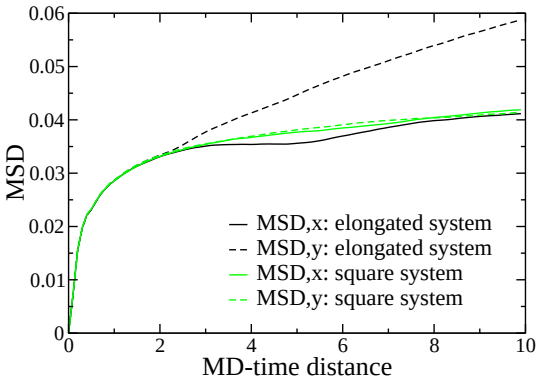

Figure 3.4: $\mathrm{MSD}_{\text{time-diff}}$ in x- and y-direction for a system with $240 \cdot 270$ particles ("square system") and for an elongated system with $2160 \cdot 30$ particles without misfit. Temperature $T = 1.0$. Each MD-time unit corresponds to a difference of 500 integration steps as the time step was $\Delta t = 0.002$.

Fig. 3.4 shows the $\mathrm{MSD}_{\text{time-diff}}$ for an uncompressed bulk system for comparison. As expected, the averaged MSDs are larger when no walls are present. Furthermore, they do not exhibit a real plateau as the center of mass is not fixed without structured walls. Additionally, this figure shows the influence of finite-size effects in connection with the shape of the system in the case where no walls are present: The "square system" behaves like a real bulk crystal where the particles are pinned to their lattice site rather strongly, while in the elongated system only the MSD in the x-direction shows this behaviour. As the number of rows is significantly smaller than the number of particles per row here, it is energetically possible for the rows to bend and assume an almost wave-like configuration, which leads to significantly larger values of the MSD in the y-direction. But of course this effect does not occur when walls stabilize

the rows.

3.3 Slow Dynamics due to Soliton Formation

If one starts out with 29 rows at a misfit of $\Delta = 2.2$ or alternatively waits long enough until the configuration which started out with 30 rows at this misfit has fully equilibrated and a regular soliton pattern has evolved, one obtains the values for the $\mathrm{MSD}_{\text{time-diff}}$ as shown in Fig. 3.5.

One can read off from Fig. 3.5, that the MSD has not reached a plateau, even at an MD-time difference of 30, for the inner rows, which means that there is some diffusion, which clearly does not involve the rows directly adjacent to the walls. This is not suprising as the rows directly adjacent to the walls retain their original number of particles and are therefore still commensurate to the walls and pinned to their position by them. Whereas the inner rows have a different number of particles now as one row has disappeared and the particles from this row have been distributed among the inner rows. Therefore they are not commensurate with the structure of the walls any more and can thus make a translational movement along the walls as the potentials created by the wall particles cannot hold them in their original positions any more. In fact, for infinite two-dimensional crystals it is well-known that the static mean-square displacement of a particle relative to its reference position in the ideal perfectly rigid crystal lattice diverges as the center of mass drifts. In the x-direction parallel to the walls we hence expect for the rows 2,...,29 which are no longer pinned by the walls that $\mathrm{MSD}(\Delta t \to \infty) \to \infty$, unlike the commensurate case of Figs. 3.2, 3.3, where the whole crystal is pinned by the boundaries, and for any finite slit thickness D we have a finite value of the $\mathrm{MSD}(\Delta t \to \infty)$ for all rows.

One can also see that generally the diffusion in row 2 and row 29 has the largest values, while the MSD is smaller again for rows further inside of the crystal, and has a minimum value for the rows directly next to the walls. This is fundamentally different from the situation shown in Fig. 3.2 and 3.3, where row 1 and row 30 also had the smallest values of the MSD, but the MSD grew larger with increasing distance from the walls instead of displaying a maximum in the rows 2 and 29 and becoming smaller again inside of the crystal. This can be explained by the influence of the solitons (in the simulations with 29 rows) which cause considerable movement in the crystal. As we will show in the following section, these solitons are present in the rows next to the rows directly at the walls, i.e. they are sitting close to the walls, thus creating the maximum of the MSD in row 2. They also cause a certain amount of disorder and movement in the rows next to them, therefore the MSD now decreases

towards the inner part of the crystal, while the MSD used to increase due to the decreasing influence of the stabilizing walls in the case without solitons. The rows directly adjacent to the walls were stabilized by the walls in both cases and thus always showed the smallest values of the MSD.

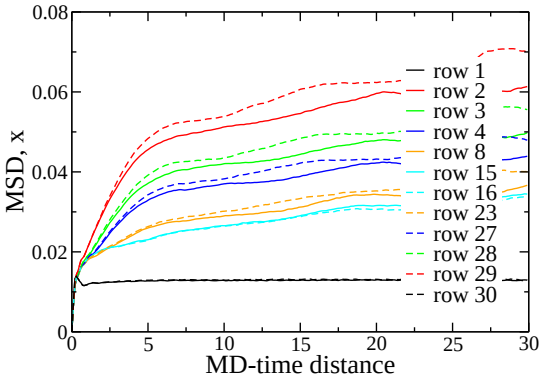

Figure 3.5: $\mathrm{MSD}_{\text{time-diff}}$ in x-direction for a system which started with 29 rows and was equilibrated at a misfit of $\Delta = 2.2$ (where 29 rows are stable). Temperature $T = 1.0$. Each MD-time unit corresponds to a difference of 500 integration steps as the time step was $\Delta t = 0.002$.

When the walls are placed closer together, creating a misfit of $\Delta = 2.2$, it takes a while until all solitons are created in this very large system. While this happens, one can watch the "MSD with respect to the time difference" grow. This is especially visible for those rows in which the solitons are created, i.e. rows number 2, 3 and 4. The effect is visible both in the x-direction and the y-direction of the MSD, although now one can see differences in the size of the MSD in x- and in y-direction. Examples of this are shown in Fig. 3.6.

While in the commensurate case characteristic times needed to equilibrate the system are of the order of a few MD time units, Fig. 3.6 reveals that the time needed to equilibrate MSD (Δt) in the incommensurate case is of the order of about 2000 MD time units (for the large system comprised of 64800 mobile particles; for smaller systems it is quicker). These large times are understandable, since the formation of the soliton staircase pattern requires the nucleation of defects moving from one boundary to the opposite boundary, as described in detail by Chui et al. [2] in the framework of Monte Carlo simulations.

Fig. 3.6 also shows that the amplitudes of the curves obtained for row 3 are larger than the ones for row 2. The curves for row 4 are qualitatively very similar, but exhibit an even larger amplitude than the ones for row 3. The fact that the amplitudes of the particles in the inner rows remain slightly larger than those in row 2 indicates that if the system is equilibrated from a 30-row-structure into a 29-row-structure and the solitons are formed at random positions, there is more disorder in the inner rows (which is typical for the case of 30 rows, compare Figs. 3.2 and 3.3), while if the system starts off with 29 rows and a corresponding "perfect" soliton pattern, there is more movement in the rows closer to the walls (see Fig. 3.5). This behaviour

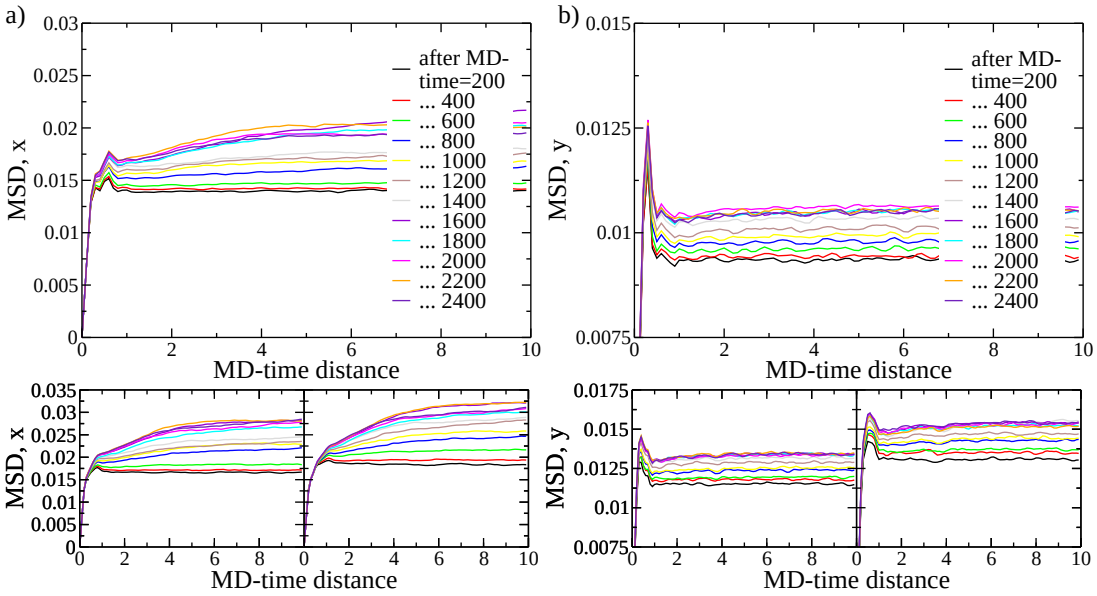

Figure 3.6: Change of the $\text{MSD}_{\text{time-diff}}$ in x-direction (a) and y-direction (b) as solitons are created. Large graphs show curves for row 2, small ones for row 3 and 4. System started out with 30 rows at a misfit of $\Delta = 2.2$ and slowly solitons are created and the structure changes into 29 rows. Temperature $T = 1.0$.

can in principle change on very long time scales as the solitons repel each other and thus push each other closer to the walls and into a more regular staircase pattern. But usually the structure forming by equilibrating a 30-row-structure into 29 rows gets stuck in a more disordered state and exhibits a less regular soliton pattern and a slightly higher stress even on long time scales.

One can also study the $\text{MSD}_{\text{time-diff}}$ for different values of the misfit Δ as shown in Fig. 3.7 for different rows. One can see that for relatively small misfits the structure with 30 rows remains stable (as Chui et al have seen in their hysteresis curves as well), but the MSD of the particles shrinks with increasing misfit since there is less space available for local motion in this compressed crystalline structure. At larger misfits (shown are $\Delta = 2.2$ and $\Delta = 2.5$) the structure has changed to 29 rows and solitons have been created, which changes the shape of the curve of the MSDs in the direction parallel to the walls due to the solitons' mobility. But it is also visible in the MSDs in the direction perpendicular to the walls: Instead of decreasing further due to the decreasing space between the walls, the MSD at $\Delta = 2.2$ is significantly larger than at $\Delta = 1.8$ (prior to the transition) and instead resemble the values at $\Delta = 1.5$ as the formation of solitons increases the mobility of the particles also in the y-direction. Of course, a further increase of the misfit reduces the MSD again, which is demonstrated

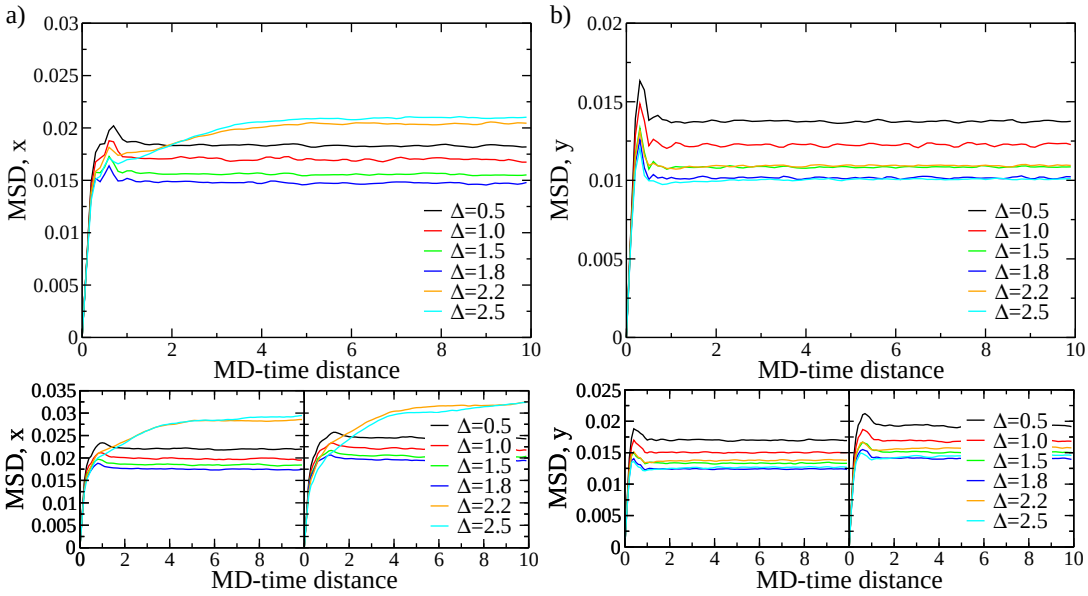

Figure 3.7: $\mathrm{MSD}_{\text{time-diff}}$ in x-direction (a) and y-direction (b) in row 2 of the system (large graphs) and row 3 and 4 (small graphs) for a system starting out with 30 rows at the indicated values of the misfit Δ. Temperature $T = 1.0$.

for the case of $\Delta = 2.5$, where the MSD in y-direction is only of the order of that at $\Delta = 1.8$ prior to the transition. Also in Fig. 3.7 the values of the MSDs are larger for row 3 than for row 2, and even larger for row 4, as we used starting configurations consisting of 30 rows at every value of the misfit.

3.4 Relaxation Dynamics of Equilibrated Soliton Structures

If one tries to calculate the $\mathrm{MSD}_{\text{time-diff}}$ of the solitons itself (which was done only in the small system with 3240 mobile particles), one has to be careful to subtract their center of mass movement. Because despite the fact that the particles itself show a very small (on the timescale we are studying here: almost invisible) center of mass movement, the soliton pattern moves around. In this movement, the soliton pattern hardly changes, i.e. the distances between the solitons remain more or less constant, but the pattern as such can easily move along the x-direction. Because after all, solitons are only those areas where some particles are closer to each other than they are on average, because some of the extra particles that stem from the row that has disap-

peared in the $n \rightarrow n-1$ transition in the number of rows now are localized there, so it only takes a few particles to make a small lateral movement and the soliton already changes its position.

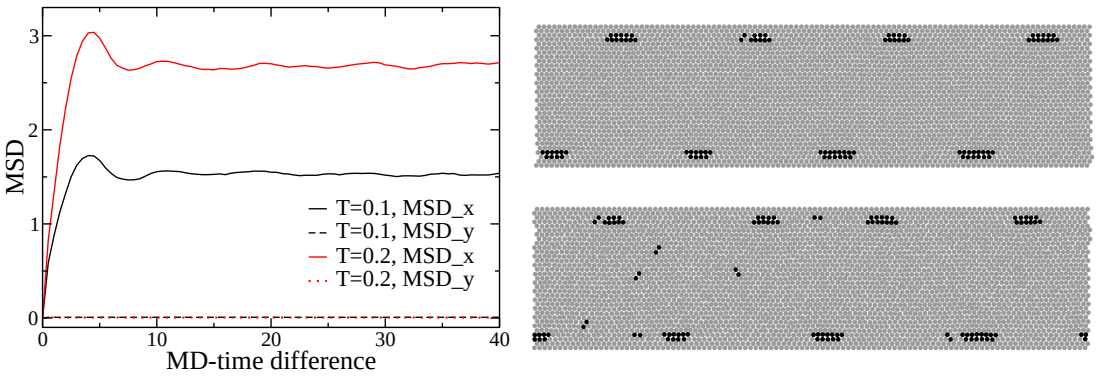

Figure 3.8: $\mathrm{MSD}_{time-diff}$ in x- and y-direction of the solitons at the indicated temperatures for simulations at $\Delta = 2.2$, averaged over the 8 solitons that appeared, and averaged over 20 runs. Please note that the center of mass diffusion of the soliton pattern as a whole has been subtracted from the solitons' movements. This center of mass diffusion of the pattern was quite large (of the order of half a distance between solitons). Simulations started with 29 rows and were equilibrated before measuring. System size is $N = 3672$ particles (including walls). Snapshots give examples of which particles are identified as solitons (black) in simulations at $\Delta = 2.2$, starting out with 29 rows, at $T = 0.1$ (upper) and at $T = 0.2$ (lower snapshot).

When one compares the amplitude of the mean square displacement of solitons shown in Fig. 3.8 with that of the individual colloidal particles (Figs. 3.2, 3.3) of the rows close to the immobile walls, several differences are worth mentioning: for individual particles, mean square displacements in x- and y-direction are of the same order of magnitude. For solitons, in contrast, mean square displacements in y-direction are completely negligible, while in x-direction they are an order of magnitude larger than the corresponding value for the colloidal particles. This is the case, because solitons strongly repel each other and therefore remain very close to the walls and thus almost immobile in the y-direction. At the same time, they can easily move in x-direction as they are regions of increased particle density, which already moves if only a few particles make a small coordinated movement in the same direction. Also the timescale for the oscillatory convergence to the plateau now is of the order of 10 MD steps, while it was of the order of 1 MD step for the particles themselves. This result is expected, recalling the estimates for the small "spring constant" that maintains the average distance between solitons [3]. It also confirms that in this particular case Monte Carlo simulations like the ones used by Chui et al in order to determine the potential and spring constant acting between the solitons yield reasonable results for the movements of the particles.

The snapshots shown in the same figure show some representative soliton configurations, where all particles which the code identifies as "possibly being part of a soliton" are marked in black. These particles were obtained with the "blocking method" described in Ref. [3] by Chui et al.: A "block" of a fixed area is moved along the rows in the x-direction in steps of the ideal next neighbour distance a (respectively in steps of a reduced nearest neighbour distance for the inner rows which contain extra particles) and the number of particles in this "block" area is counted. We chose a circular test area with a radius of $r = (1 + \epsilon_a)a$ which should contain seven particles in the ideal crystalline case (one central particle and its six nearest neighbours), ϵ_a being adjusted to the temperature: we have used $\epsilon_a = 0.07$ for $T = 0.1$ and $\epsilon_a = 0.11$ for $T = 0.2$ in order to obtain a clear picture of the solitons. Thus we were able to identify areas where particles were surrounded by either less or more than six nearest neighbours. Of course, only clusters of a certain number of these particles are actually counted as solitons, so the wrongly identified particles somewhere in the middle of the system (especially at slightly higher temperatures) do not disturb the statistics. As it is quite difficult to distinguish particles which do or do not belong to solitons for higher temperatures, only $T = 0.1$ and $T = 0.2$ were used here.

3.5 Observations of Diffusion in Simulations of Colloidal Crystals

We now return to uncompressed commensurate crystals ($\Delta = 0$), where at $T = 1.0$ the snapshots reveal in the overwhelming majority of cases a defect free triangular crystal structure (a typical example is shown in Fig. 3.9). This is not surprising as it is known that the density of vacancies and interstitials in $d = 2$ for any nonzero temperature is also nonzero in thermal equilibrium [122, 134], but very small at temperatures significantly below the melting transition [1, 51], which occurs at $T_m = 1.35$ for our system. We ask, whether in such almost ideal crystals still some diffusion of particles occurs. In principle, this question is relevant for unconfined crystals (to be simulated using periodic boundary conditions in both x- and y-direction) as well, but we focus here on diffusion in a system confined by structured walls as a by-product of our studies in the preceding section. To study this question, we consider a large system comprised of 73440 particles and long time scales. Also MSDs of the particles need to be investigated over much longer time intervals than the ones we considered before.

If one studies the MSD with respect to the starting configuration $\text{MSD}_{\text{start-conf}}$ shown in Fig. 3.10 (again for T=1.0 and for the larger system), for the case without a misfit, one gets a first idea about diffusion processes inside of the crystal: Although

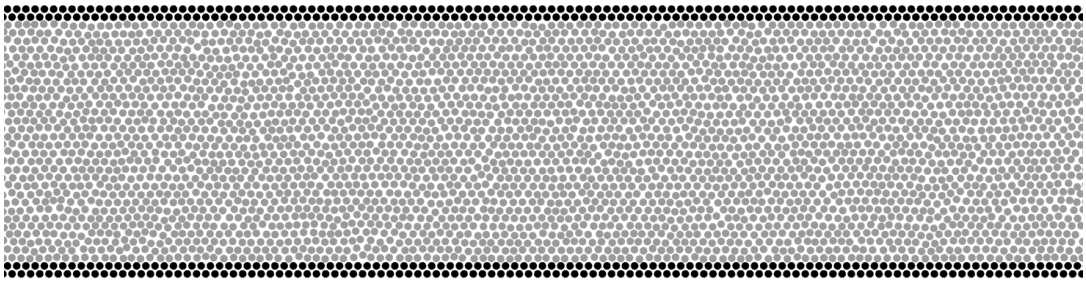

Figure 3.9: Typical snapshot of the system at $T = 1.0$ showing a basically defect free triangular crystalline structure. Black dots denote wall particles, grey dots are mobile particles.

the crystal structure is stable, there is a considerable amount of diffusion. This diffusion does not happen continuously, but every now and then larger groups of particles change their position. Although only in x-direction translational invariance is present, the diffusion of particles involves both the x- and the y-coordinate as the particles have to move from one crystalline lattice site to another one. A center-of-mass movement is excluded due to the presence of the structured walls which fix the crystal also in x-direction. And as the values of the MSD are typically quite small in this system (most particles only move by a few lattice spacings, if at all), we will study the MSD as a whole and not specifically its x- or y-component here (which would mostly differ from each other due to the orientation of the crystalline rows along the x-axis). Of course, the size of the MSDs as a whole would probably be larger in the case without walls.

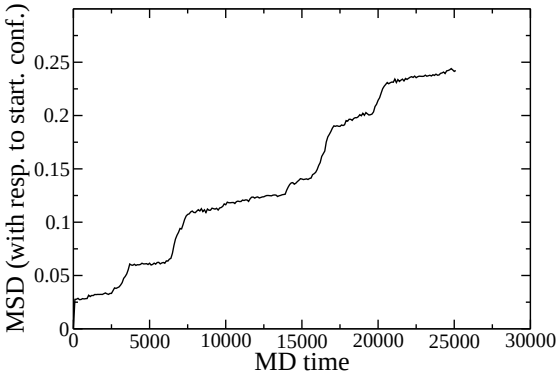

Figure 3.10: Example of a $\text{MSD}_{\text{start-conf}}$ for a system with $N = 73440$ particles (including walls), $\Delta = 0$ and 30 rows at $T = 1$. In spite of this diffusion, the structure remains crystalline.

In order to investigate this phenomenon, one can look at snapshots of the system, where all particles which are not in their initial lattice position any more, have been marked. A few typical sections of such snapshots are shown in Figs. 3.11 and 3.12. Obviously, there are a few circular or ring-like dislocations, where in a group of particles, each particle has jumped onto the lattice site of its neighboring particle, and

as the ring is closed, the motion stopped here (Fig. 3.11). In other parts of the crystal, a lot of particles have left their initial lattice site and have jumped onto some other particle's initial position instead (Fig. 3.12). The crystal is still crystalline here and shows a clear hexagonal lattice structure despite the fact that so many particles are not in their initial positions any more as one can see in the lower figure. Also the disorder present due to phonons (particles being somewhat displaced from their ideal positions in the perfectly rigid structure at temperature $T = 0$ in a coherent, collective way) can be virtually recognized.

The well-known theory of diffusion inside of crystals states that diffusion takes place through the creation of a pair of one interstitial particle sitting no longer on the "allowed" lattice sites, but moving somewhere in between them, and a hole, which it leaves behind and which can diffuse as particles from adjacent lattice sites can jump into it. The formation of such pairs of interstitials and vacancies is induced by thermal fluctuations. This mechanism is prevalent in those areas of the snapshots where a lot of particles have left their initial lattice sites and sit on different lattice sites instead. Naturally, this process involves a lot of particles as the interstitial as well as the hole perform a random walk. At the temperatures we studied here, the density of holes and interstitials is still extremely low, so the interaction of two of such pairs is excluded. Therefore the diffusion process only stops when this particular pair of vacancy and interstitial happens to be in the same position again and recombines. Despite the fact that they attract each other by being a high-pressure spot and a low-pressure-spot in the crystalline structure, within the resulting recombination times up to several thousand particles can be removed from their initial lattice site.

One snapshot showing the beginning of this "hole and interstitial"-diffusion process is given in Fig. 3.13. One can see the hole at the end on the right hand side of the wavy line of particles that have been displaced from their initial lattice sites as well as the fact that there is one extra particle for the crystalline structure at the left hand side inside of the "blob" of displaced particles. This is illustrated in the enlarged sections showing that the number of nearest neighbor particles is not equal to six for all particles around the vacancy and the interstitial: In the proximity of the vacancy we found one particle with eight neighbors and two with seven; in the region with the interstitial two particles have five neighbors and two have seven. The lower graph shows the same section of the system at a later time: here, the recombination of hole and interstitial has occurred quite soon, leaving behind a closed curve of particles that have been displaced from their initial lattice sites, but are sitting in correct (different) lattice sites again. The creation of these vacancy-interstitial pairs at $T \leq 1.0$ are still such rare events, that the interaction between two different pairs is still negligible.

But in the case of the smaller rings of particles that have been displaced from their initial lattice sites by jumping into their neighbor's position, the mechanism seems to

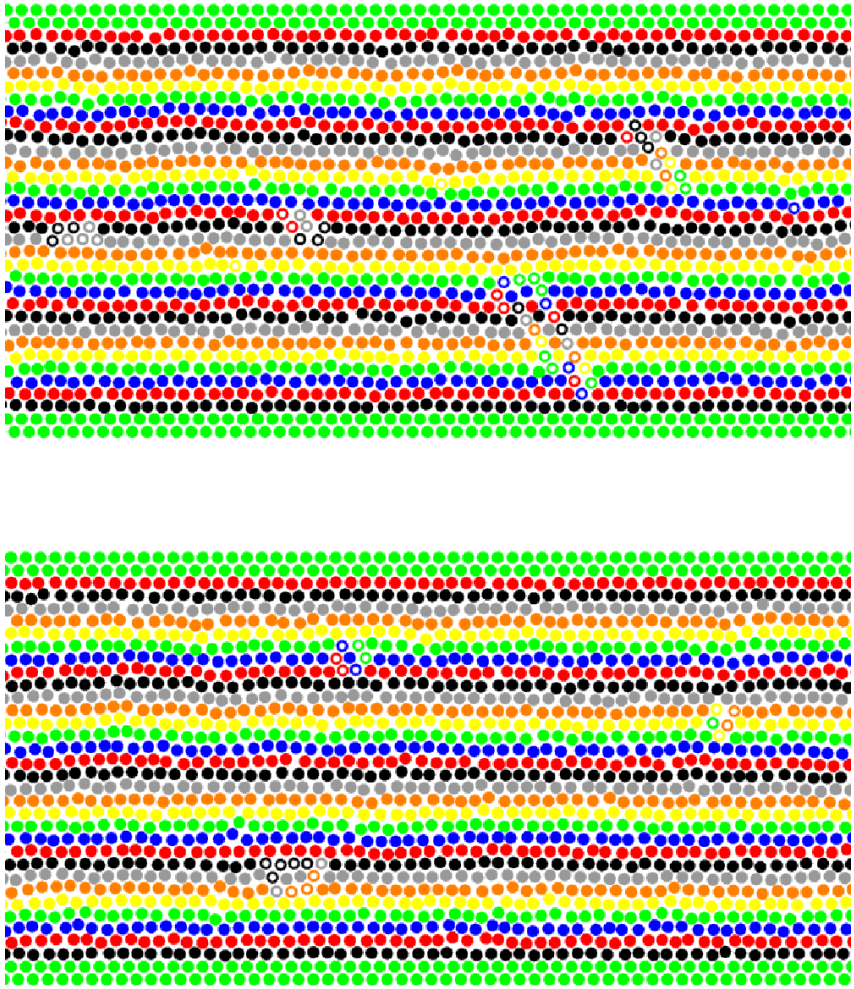

Figure 3.11: Snapshots of differently sized clusters of particles which moved away from their initial positions. A section of the system is shown, where at time zero the subsequent mobile rows are marked by different colours in the y-direction (row 1 is black, row 2 is red, rows 3 is blue, etc, from bottom to top), to indicate the particles that have left their row at a later time. The whole system consisted of $N = 73440$ particles (including walls). Simulations were carried out at $\Delta = 0$, $T = 1$ and with 30 rows. These snapshots were taken at an MD time of 4000 (relative to starting the simulation with the unequilibrated ideal crystalline configuration). Those particles, which are not in their initial position any more, are displayed as circles, all of the other particles as dots.

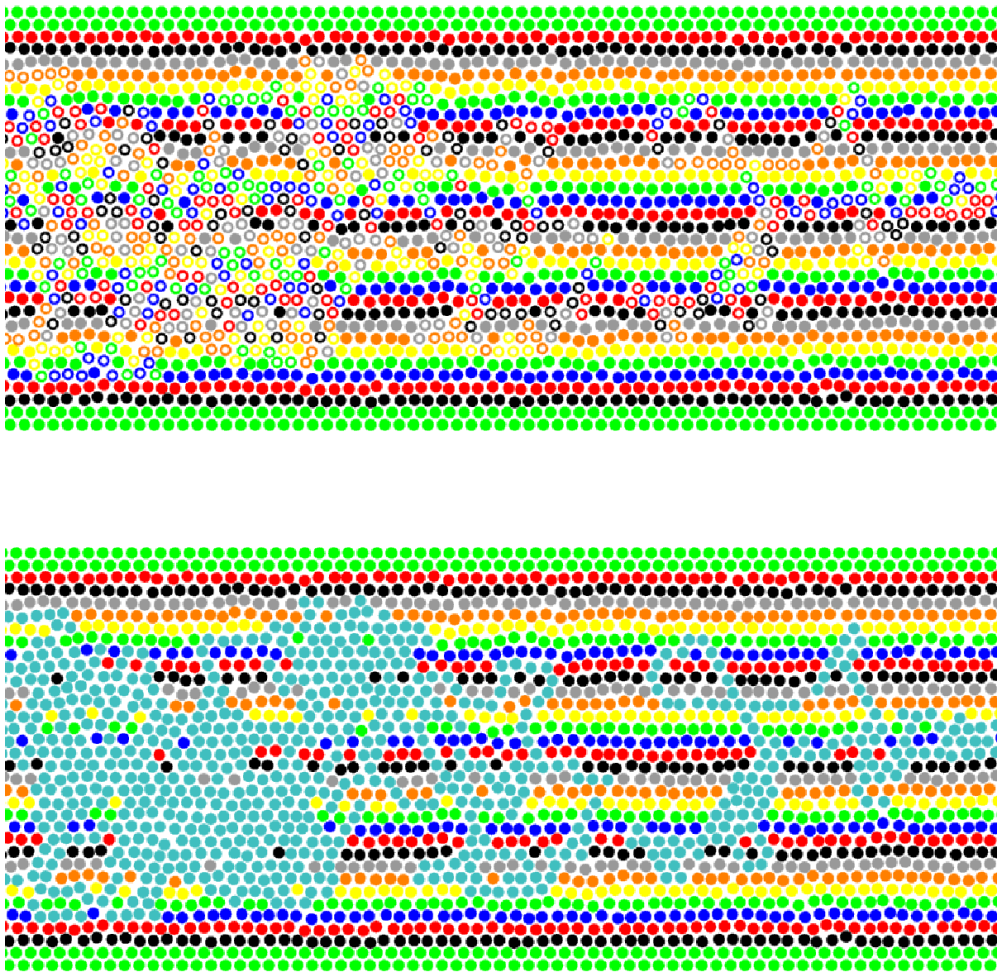

Figure 3.12: Snapshots showing the results of the "normal" diffusion process. Those particles, which are not in their initial position any more, are displayed as circles, all of the other particles as dots in the upper snapshot. Colouring scheme like in Fig. 3.11. Snapshot on the right shows the same section of the system, but displaced particles are shown in blue here, so that the crystalline structure, which is still clearly present in the system, becomes more obvious. The whole system consisted of $N = 73440$ particles (including walls), $\Delta = 0$, $T = 1$ and 30 crystalline rows.

be different: We observe the process referred to as "cooperative ring rotation process" in [20].

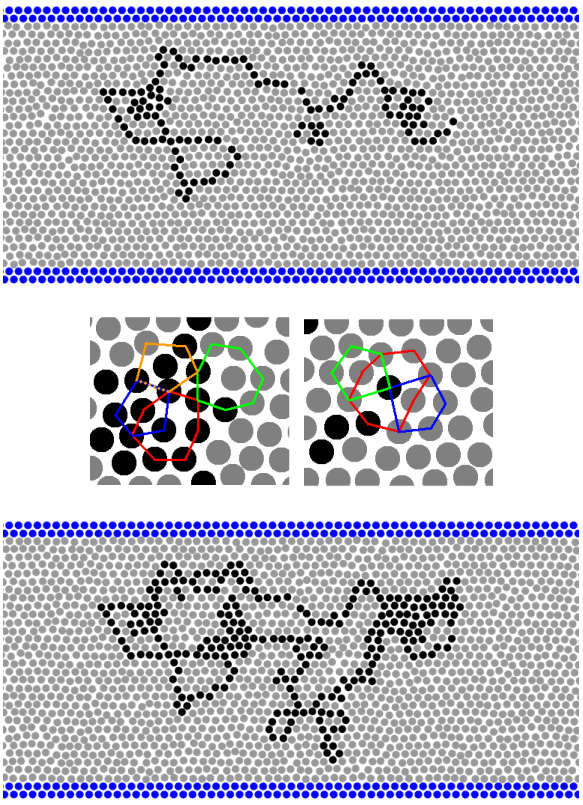

Figure 3.13: Snapshots illustrating the effect of "normal" diffusion in a simulation at $\Delta = 0$, $T = 1$, 30 rows. A section of the system is shown at two different time steps showing how such a diffusion builds up. Displaced particles are shown as black dots here, while all other particles are shown in grey). The enlarged sections in the middle panel indicate the nearest neighbor particles of those particles which have more or less than six neighbors due to the interstitial particle (left) respectively due to the vacancy (right snapshot), cf. text.

In the beginning of the research on diffusion in the 1930s and 1940s, different diffusion mechanisms were discussed [17, 18] and the idea of diffusion being carried out by groups of particles making cooperative rotations and even direct exchange between two particles was very popular. However, the Kirkendall experiment [19] showed that in metallic alloys the prevalent diffusion mechanism is via vacancies and/or interstitials. Since there has been no experimental evidence for different diffusion mechanisms, the general belief is that cooperative rotation processes play no important role (or do not even exist) in diffusion processes in three-dimensional crystals [20–22]. In two-dimensional crystals like the one we are studying here, there are only two other studies describing such cooperative rotations [24, 25]. In both of these studies by Montalenti et al. this particular diffusion mechanism has been found to be extremely rare and could only be observed by applying the rare event sampling technique of temperature-accelerated dynamics (TAD) [132, 133]. Of course, they were investigating more complex (and realistic) systems than the one we are studying here, but still it is fascinating that such cooperative rotation phenomena can also be observed in our simulations. Due to the less complex model system we used, we were even able to use system sizes and time scales on which many of these rotations

occurred, which allowed us to gather statistics of the number of particles involved in them and to compare them to the "normal" diffusion phenomena.

Investigating these cooperative rotations in detail shows that there is not one distinct particle which starts the movement by being displaced from its original position and leaving behind a hole, but that it is a joint movement of the whole group of particles which is induced by thermal fluctuations. While making this concerted rotation movement, some disorder is visible in the crystal around the ring of particles, until the ring has fully turned into its final position and all particles are sitting in lattice sites again. Fig. 3.14 illustrates this process: Initially, there seem to be larger than average fluctuations in the area of the crystal left of the ring. Note that there is no real hole or interstitial particle, there is exactly the right number of particles for this part of the crystal, they are only fluctuating strongly. This might "infect" the left particles of the ring, motivating them to fluctuate with a larger amplitude than on average and passing their momentum on to the other particles in the ring. The ring then jointly begins to turn around. In the 3rd snapshot shown one can see how the local structure around the ring has adapted to it: the ring of particles does not fit into the general crystalline structure any more as it has a different angle, but the particles around the ring have adjusted themselves to the ring and not to the rest of the crystal. Finally, the crystalline structure is restored again (which is, after all, energetically preferable) while the particles in the ring turn around further, ending in a position which is commensurate with the crystalline lattice, and the movement stops. These snapshots were taken at intervals of about 200 MD-steps, with $\Delta t = 0.002$, so the series of snapshots shown in this Fig. 3.14 covers an "MD-time" of $4 \cdot 0.4 = 1.6$ (with $\gamma = 0.5$ and at $T = 1.0$). A short movie showing this cooperative circular movement of particles is also included in the CD-Rom accompanying this thesis.

In order to quantify these diffusion phenomena, we recorded histograms showing which cluster sizes occur at which temperature: Fig. 3.15. We also show in the same graph, that the curves are independent of the friction coefficient γ as expected. The clusters with sizes between 2 and about 25 particles correspond to situations where particles have actually swapped positions. In the case of only 2 particles, which is rare, these particles have probably swapped positions during a large fluctuation while all of the other particles that took part in this fluctuation have returned to their initial positions. From 3 particles onwards, mostly cooperative circular movements have occurred. Cluster sizes of 3 and 6 particles seem to be favoured due to the hexagonal lattice structure. Larger clusters correspond to cases where a hole and an interstitial have been created and led to diffusion.

Particles were counted as being displaced if they moved more than half of the average next-neighbor distance away from their initial position. In order to exclude pure fluctuations of particles which moved back into their "own" position eventually,

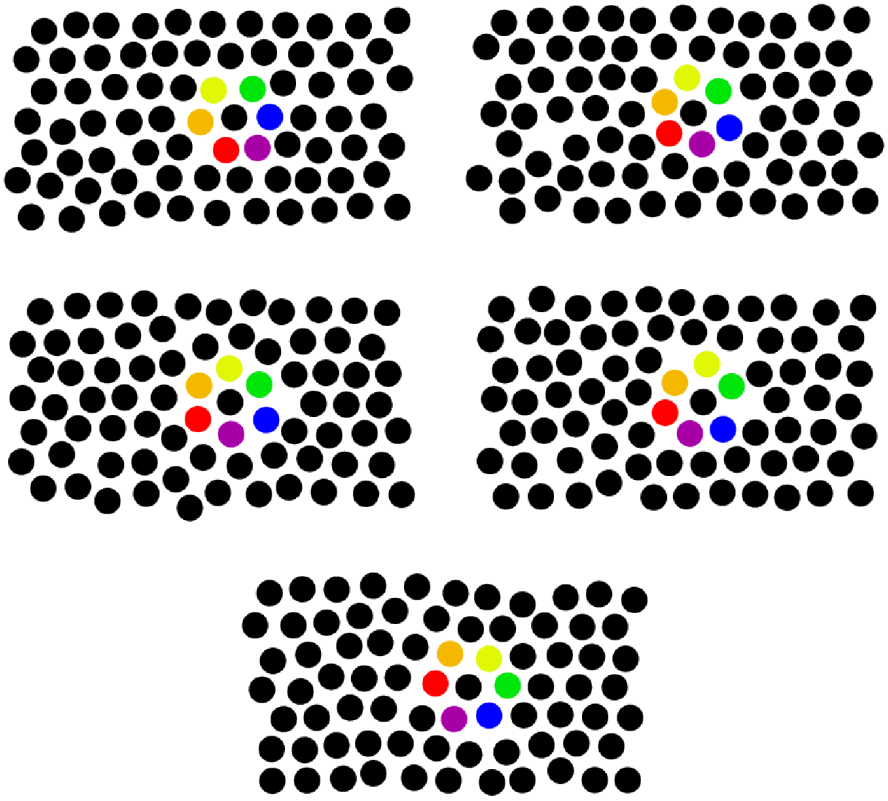

Figure 3.14: Cooperative ring rotation process shown in a series of snapshots between which an MD-time difference of 0.4 lies (chronological order from upper left to lower right). Simulation at $T = 1$, $\Delta = 0$ and with 30 rows.

displaced particles were identified in two snapshots, 10.000 MD-steps apart from each other, and only those particles which were displaced in both snapshots were counted here. 10000 MD-steps seems to be a good time interval here, as single particles easily fluctuate back into their old position on this time scale, but those which have swapped positions practically never go back into their old positions.

Using the values given in Fig. 3.15, it is possible to estimate the activation energy for ring rotation processes. Fitting the number of occurrence of rings consisting of 3 particles versus temperature with the formula $y = y_0 \cdot e^{-A/T}$, $k_B = 1$, yields an activation energy of $A = 13.8$. Fitting the corresponding curve of the number of occurences of rings consisting of 6 particles yields a slightly higher activation energy of $A = 14.1$, which is not surprising as larger rings are clearly more difficult to rotate.

In order to estimate the contribution of the cooperative ring rotation processes

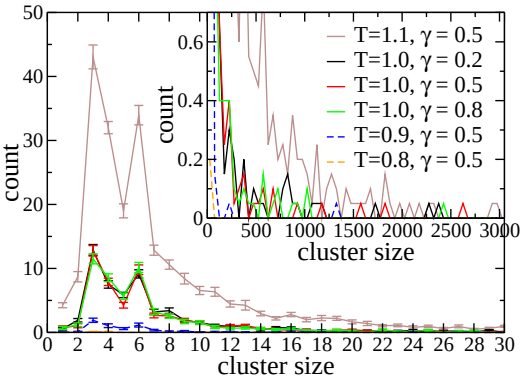

Figure 3.15: Histograms of the distribution of cluster sizes at the indicated temperatures. As expected, the curves are independent of γ (in the range of their errors). Inset shows the distribution of larger clusters; please note that the binning of the histogram is wider there. The data was taken after the simulation had run for $2 \cdot 10^6$ steps; system size was $N = 73442$ particles (including walls) and it was averaged over 20 runs.

to the diffusion constant, one can show that each particle which is not in its initial position any more, but insteads sits in one of its neighbors' lattice site, contributes $\frac{1}{N} \cdot a^2$ to the MSD, a being the crystal's lattice constant:

If $m(t) = \frac{1}{N} \sum_{i=1}^{N} [x_i(t) - x_i(0)]^2$ denotes the MSD$_{start-conf}$, let $m_0(t)$ denote the MSD of such particles which do not participate in any rotation processes (and, for simplification, also not in any other diffusion process). Let's assume that this $m_0(t) = c_0$ for all times t greater than a small time t_s in which a harmonic movement of the particles is visible (i.e. if one would plot $m_0(t)$ one would see an overshoot for very small times t and then just a straight horizontal line).

Then we can calculate the MSD $m_1(t)$ of *only* particles which do participate in a ring rotation process and each of which move onto a neighbor's lattice site in this process, thus they all move exactly one lattice constant a away from their initial lattice site and then fluctuate around this new lattice site. For this $m_1(t)$ of the N_0 particles which participate in this rotation we can write:

$$\begin{aligned} m_1(t) &= \frac{1}{N_0} \sum_{i=1}^{N_0} [x_i(t) - x_i(0)]^2 \\ &= \frac{1}{N_0} \sum_{i=1}^{N_0} [x_i(t) - x_i(T_0) + x_i(T_0) - x_i(0)]^2 \end{aligned} \tag{3.1}$$

with T_0 denoting a time where the particles have just moved onto the new lattice sites, yielding $x_i(T_0) - x_i(0) = a$ and $x_i(t) - x_i(T_0)$ being the distance between a particle and its new lattice position which is for $t - T_0 \gg t_s$ *on average* the distance which

the non-rotated particles have from their (initial) lattice positions aswell. Thus:

$$\frac{1}{N_0}\sum_{i=1}^{N_0}[x_i(t) - x_i(T_0)]^2 =$$
$$\frac{1}{N_0}\sum_{i=1}^{N_0}[x_i^2(t) - 2x_i(t)x_i(T_0) + x_i^2(T_0)] = m_0(t) = c_0 \tag{3.2}$$

Therefore we can write Eq. 3.1 as:

$$\begin{aligned} & m_1(t) \\ & = \frac{1}{N_0}\sum_{i=1}^{N_0}[x_i^2(t) - 2x_i(t)x_i(T_0) + x_i^2(T_0) \\ & + 2ax_i(t) - 2ax_i(T_0) + a^2] \\ & = m_0(t) + 2a\frac{1}{N_0}\sum_{i=1}^{N_0}[x_i(t) - x_i(T_0)] + a^2 \\ & = m_0(t) + a^2 \end{aligned} \tag{3.3}$$

as $\frac{1}{N_0}\sum_{i=1}^{N_0}[x_i(t) - x_i(T_0)] = 0$ if we average over enough particles as some particles move to the right hand side, some to the left (always measuring distances from their new lattice site $x_i(T_0)$) and thus the average should be zero.

Thus the MSD of the whole system comprised of N particles out of which N_0 participate in a rotation movement reads:

$$m(t) =$$
$$\frac{1}{N}[(N - N_0)\cdot m_0(t) + N_0\cdot(m_0(t) + a^2)] = m_0(t) + \frac{N_0}{N}a^2 \tag{3.4}$$

This can easily be checked through simulations, shown in Fig. 3.16: The difference between the averaged MSD before the particles have made a circular movement is (within the small errors) exactly by a^2 smaller than after the circular movement, when each particle sits on its neighbors' lattice site. The fluctuations are larger, though, as the MSD is calculated with respect to the "old" lattice site.

In order to get an idea about the size of the contribution of the circular movements to the MSD (and therefore to the diffusion constant), one can have a look at Fig. 3.15 again: It shows that in a typical run at T=1.0 after 2 million steps there are about 400 particles which are displaced from their initial lattice sites through circular movements, but about a few thousand which are displaced due to the "normal" diffusion

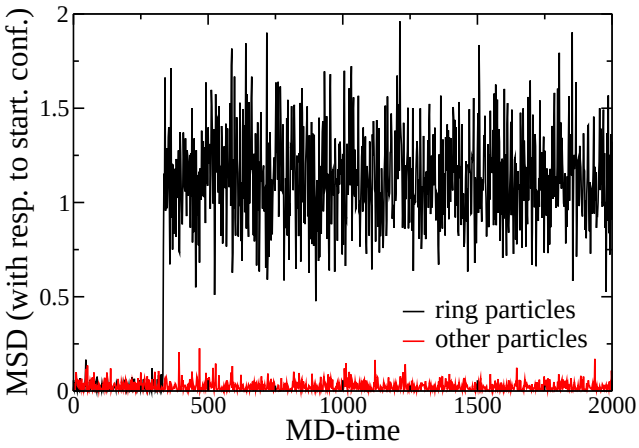

Figure 3.16: Contribution of a cooperative ring rotation process to the $\text{MSD}_{\text{start-conf}}$: Just as calculations show, the MSD of those particles which participated in the rotation process (referred to as "ring particles" in the legend) is (on average) increased by a^2, a being the lattice constant, in comparison to the MSD of particles which did not participate in the rotation process ("other particles"). Simulation at $T = 1$, without misfit. System size was $N = 73440$ particles (including walls).

mechanism of hole and interstitial. Therefore the "normal" diffusion mechanism contributes considerably more to the MSD. Actually, the contribution of a single event, where for example a ring of 6 particles makes a circular movement, cannot be seen in the MSD at all, as its contribution is just $6 \cdot \frac{1}{N} \cdot a^2$, which is smaller than the fluctuations of the MSD, at least for the large system with 64800 mobile particles. So the steep parts of the MSD shown in Fig. 3.10 are due to the "normal" diffusion processes, which involve a few hundred or even a few thousand particles and not due to such small circular movements. The small circular movements are therefore not visible in this plot.

At slightly lower temperatures, however, such large-scale diffusion processes seem to vanish (compare Fig. 3.15). Unfortunately, also circular movements become much rarer in this case.

In order to quantify the diffusion, we calculated the diffusion constant C_D by fitting the MSD (which we obtained from averaging over 20 simulation runs at temperatures $T = 0.9$, 1.0 and 1.1) with the formula $MSD_{\text{start-conf}} = y_0 + 6C_D t$. The offset y_0 was necessary, because we started out with equilibrated configurations. This yielded the values of the diffusion constant given in Table 3.1.

T	0.9	1.0	1.1
C_D	$1.90 \cdot 10^{-6}$	$5.72 \cdot 10^{-6}$	$3.05 \cdot 10^{-5}$

Table 3.1: Diffusion constants at different temperatures

Fitting these values via $C_D = C_{D,0} \cdot e^{-A/T}$, $k_B = 1$, in order to obtain an estimate

for the activation energy of the diffusion, yields $A \approx 17.7$, which is higher than for the rings consisting of 3 or 6 particles. Again, this is not surprising as the formation of a hole and an interstitial introduces more disorder into the crystal than a rotation of some particles. This also indicates that ring rotations are to be expected to occur at slightly lower temperatures than diffusion mechanisms based on holes and interstitials. And even if the circular movements do not play an important role for the overall diffusion constant in this particular system, they might do so in other systems where the range of temperatures where ring rotations do already occur, but holes are not yet created, might be larger than here.

But still it is interesting to see that there are two different diffusion mechanisms and even if the circular movements might not play a very important role for the diffusion constant in this particular system, they might do so elsewehere or under different conditions.

The MD-timescale of the circular movements of small groups of particles is between 0.4 and 2.5, i.e. with $\Delta t = 0.002$ they needed about $200 - 1200$ MD steps. Fig. 3.17 gives a rough idea of the timescale of the cooperative ring rotations and its distribution. Larger clusters seem to need more time. For comparison: A cluster which was built up by "normal" diffusion processes (but was comparably small for such a cluster) consisting of 58 displaced particles needed an MD-time of 4.8.

Larger rings of particles seem to need rather more time (see Fig. 3.17).

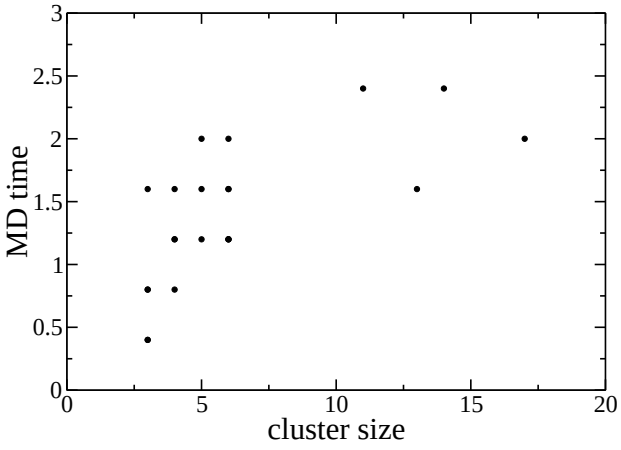

Figure 3.17: MD-time which the cooperative ring rotation needed versus cluster size. MD-time is only computed down to an accuracy of 0.4 as this already meant that snapshots had to be written out after every 50 steps. System size $N = 73442$ particles, $T = 1$, no misfit. These data points are only meant to give a rough idea of the timescale of the cooperative ring rotations.

The larger "normal" diffusion processes including a pair of a hole and an interstitial need generally more time, but usually also affect much more particles. Their timescale depends strongly on the cluster size. For example, a very small such cluster comprised of 58 particles needed an MD-time of 4.8, while clusters comprised of some thousand particles can easily need around $1 \cdot 10^6$ steps, i.e. an MD-time of $1 \cdot 10^6 \cdot 0.002 = 2000$. It varies very strongly, of course, as sometimes hole and inter-

stitial particle recombine very quickly and sometimes they do not. Typical timescales of these processes can be read off from Fig. 3.10 as the "steps" in the MSD correspond to these "normal" diffusion processes building up large clusters of displaced particles.

3.6 Concluding remarks

To conclude, we have conducted a thorough study of the different types of motion in two-dimensional colloidal crystals confined between walls, that were composed of rigid particles and that were placed at commensurate or incommensurate distances. We have observed motion on different length and time scales: in the case with commensurate walls, where the crystal is not compressed, the MSD of the particles is finite in x- as well as in y-direction, as the walls pinn the particles and prevent any movement of the center of mass. The MSD is larger for rows inside of the crystal than for rows close to the walls as the walls impose a boundary condition of zero amplitude for the phonons.

If the walls are placed closer together, thus compressing the crystal, the MSD of the particles becomes smaller as there is less space available per particle. The MSD shows no sign of the proximity of the structural transition, which occurs when the walls are placed even closer together and one of the crystalline rows disappears, which leads to the creation of solitons.

Once this structural transition has taken place, the MSD changes significantly: Now the MSD still has the smallest values for the rows directly adjacent to the walls, but has the largest values for the rows directly next to the rows adjacent to the walls, as the solitons are located there. Further inside of the crystal, the MSD decreases (instead of increasing), but is still considerably larger than in the case without solitons. Additionally, due to the incommensurability of the number of particles per row, the inner rows are no longer pinned by the potential created by the walls and the center of mass is free to move. Therefore, the MSDs of all rows except the rows directly adjacent to the walls do not reach a plateau at all any more. This structural transition needs considerably more MD time than the average equilibration time in this system.

The MSD of the solitons itself differs significantly from the MSD of the particles. It is almost negligible in the y-direction, but an order of magnitude larger than the MSD of the particles in the x-direction, as the center of the solitons can already move by a few interparticle distances if the particles involved in it only make a small coordinated movement in one direction. As the solitons are arranged in a lattice similar to a crystal and interact with each other via a harmonic potential as previous work has

shown [3], their mean square displacements also show an initial overshoot. As the "spring constant" mediating the interaction of the solitons is small, this overshoot can be seen at time differences which are again an order of magnitude larger than in the case of the mean square displacement of the particles.

We have also presented results on the diffusion processes occurring in colloidal crystals. In addition to the well-known diffusion mechanism in which a pair of a hole and an interstitial is created, diffuses and finally annihilates itself again, we have found that in this particular system cooperative ring rotation processes are common. They can involve different numbers of particles, but 3 or 6 particles are the preferred numbers due to the hexagonal lattice structure, and the diffusion occurs by a concerted and simultaneous movement of all of these particles, which move into their neighbor's lattice site.

These rotation processes do not contribute to overall diffusion as much as the hole-and-interstitial processes, but that is only due to the much smaller number of particles involved in these ring rotation processes. They do, however, occur much more frequently than the hole-and-interstitial processes. This is especially remarkable as in other systems such ring rotation events have been observed only very rarely. For instance, the study described in Ref. [25] had to be carried out using temperature-accelerated dynamics, which is a kind of rare event sampling, while in the system and at the temperatures that we studied, these events were not rare at all. Of course, this is probably due to the fact that our model is much simpler. Still, we feel that these cooperative ring rotations should not be neglected when diffusion in two-dimensional crystals and at interfaces is studied, as it is possible that they play an even more important role in other systems.

Chapter 4

Shearing the walls

The results presented in this chapter have already been published in Ref. [28]. This paper is very similar to the present chapter, on which it was based, with the exception of a few graphs and snapshots which were not shown in the paper, small changes in the introduction and some changes in the description of the details of the simulation in the present text.

In this chapter we will investigate the effect of sheared walls on a two-dimensional colloidal crystal. The effect of shear on crystallization and melting of colloidal hard-sphere suspensions has been thoroughly investigated in three-dimensional systems (e.g. [135]). In two dimensions, we are only aware of a recent study where highly charged polystyrene spheres (with radius $R = 1.95\mu m$) were driven over a periodic potential created by laser fields [118]. We expect that similar experiments could be done with other colloidal systems where particles interact with repulsive potentials, too.

The effect of shear on the homogeneous and heterogeneous nucleation of various types of colloidal suspensions [136–139], on phase separation [140] and on colloidal glasses [141] has also been addressed.

One of the important questions in this context is how the structure formation in colloidal systems can be influenced by the various tunable parameters (interaction potential, size, shape, mixtures of different kinds of particles) and by imposing external conditions like confinement, shear, compression and temperature [142]. A thorough understanding of these processes is necessary for the design of methods to create nanostructures utilizing the self-assembly of particles. The aim here is to be able to predict which pattern will form under which conditions.

Several studies using Monte Carlo computer simulations have already been carried out investigating the structure formation in colloidal crystals. Some of them have focussed on the effect of different kinds of walls [83, 143], on the impact of external fields [117] and on confinement incommensurate with the crystalline structure leading to the formation of a soliton staircase (Chapter 2 and [1–3]) in a one-component colloidal system crystallizing in a triangular lattice structure. Additional studies have investigated the melting [89], the deformation [90], the correlation between channel geometry and pattern formation [91, 144] and frustration [145] of such two-dimensional systems of purely repulsive particles under confinement. Others have considered binary mixtures which crystallize into a square lattice structure [38, 39, 146–150] and fluid systems [151]. In this chapter we will concentrate on the influence of shear on a one-component colloidal crystal with a hexagonal lattice structure. For the sake of computational efficiency, no explicit solvent is used. Both the cases when the periodicity of the confined crystal is commensurate with the periodicity of the rigid boundary and when it is incommensurate will be considered. The aim of our work is to clarify the range over which moving boundaries induce flow of particles in such a soft crystal, and to study the extent to which such nonequilibrium phenomena can still be described by local equilibrium concepts.

In the following section, we will describe details of the simulation which are specific to the case with shear. In section 4.2 we will report on the results of our simulations with sheared walls for the case where the effective periodic wall potential is commensurate with the lattice period of the crystal. We will present snapshots of the created configurations, velocity profiles and angular distributions. Then we will move to the results for the case where the lattice period is no longer commensurate with the wall potential and present the same quantities in order to compare them. As a last step, we will look at the mean square displacement of the particles in both cases. In section 4.3 we will briefly summarize the main conclusions of this work.

4.1 Details of the simulation

In the following, we will study the effect of shear on two-dimensional colloidal crystals by using the same model system as described in Ch. 1. So the particles are interacting via a purely repulsive potential and arrange themselves into an hexagonal crystalline lattice at the temperatures studied here. Shear is implemented by moving the two walls on either side of the stripe. These structured walls are moved in the x-direction with the same, constant velocity, but in opposite directions as illustrated in Fig. 4.1.

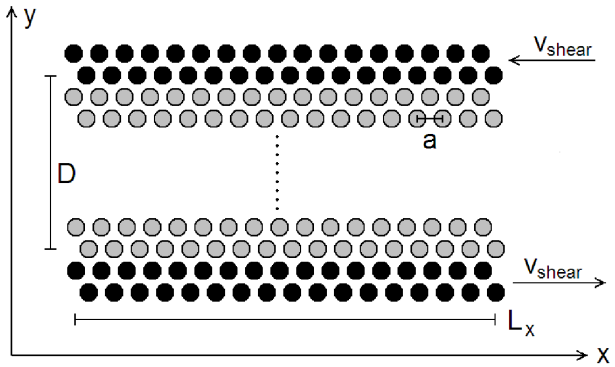

Figure 4.1: Sketch of the system geometry with the directions of the axes and the sheared wall particles. Black dots denote wall particles, grey dots freely movable particles.

Simulations are carried out at two different values of the misfit (see definition of the misfit and its consequences for the crystalline structure in Chapter 1.2): At $\Delta = 0$ the system exhibits perfect crystalline order and is comprised of 30 rows of particles in the y-direction, while at $\Delta = 2.2$ in the case without shear only the configuration consisting of 29 crystalline rows and the appropriate number of solitons is stable. We considered systems consisting of $N = 73440$ particles.

Like in Ch. 3, the simulations were carried out using the program package HooMD-blue [13, 14]. We chose a timestep of $\Delta t = 0.002$ and a friction coefficient of $\gamma = 0.5$. Because of the huge speed-up that occurs when MD simulations are run on graphic cards we initially used them as well, but experienced problems with the accumulation of systematic errors (see Appendix C). However, as the graphic card code uses single instead of double precision, we had to carry out the simulations on regular CPUs as the higher accuracy turned out to be necessary for our crystalline systems at the temperatures $T = 0.3$ and $T = 0.5$ which we used here. These temperatures are below the melting transition which would occur for this system at the chosen density of $\rho = 1.05$ (for the case without misfit) at about $T = 1.35$ [1]. Nevertheless, the Langevin thermostat only takes into account the velocities of the particles in the bulk (and not the velocity of the wall particles which are moved with constant velocity in order to introduce shear into the system). This leads to a higher effective temperature of the particles due to their interaction with the moving wall particles, because the wall particles are constantly introducing friction and thereby increasing the temperature (see Fig. 4.2). The Langevin dynamics are aiming at restalling the initial temperature, but as the wall particles move again with every new time step, more heat is added to the system, and an equilibrium between the cooling due to the Langevin thermostat and the heating due to the sheared walls is reached. This equilibrium temperature is higher than the temperature which was set in the Langevin thermostat. But this temperature increase due to the sheared walls does not only depend on the velocity of the walls, but also on the interactions of the particles with the walls. So at rather low shear velocities between $v = 0.1$ and $v = 3.5$, the effective temperature of

the system increases with increasing shear velocity, but for a very high shear velocity of $v = 50.0$, the effect of the shearing on the temperature is almost negligibly small again, because such a fast shearing has almost no effect on the particles next to it, which feel only an averaged-out wall potential in this case.

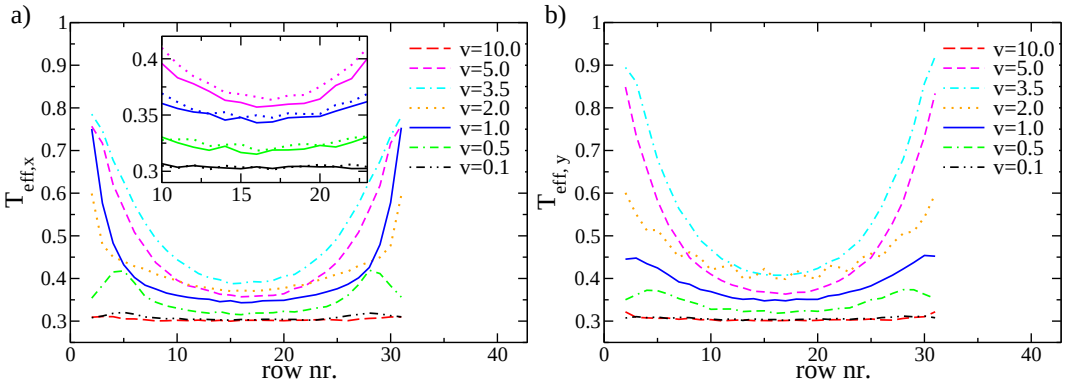

Figure 4.2: Effective temperature, calculated from the velocity distribution in x-direction (a) and y-direction (b) by fitting it via $f(v_x) = a_0 \cdot e^{(v_x - \bar{v}_x)^2/(2T_{\text{eff}})}$ (and likewise for v_y, with $\bar{v}_y = 0$). Shear velocities of the walls as indicated. Starting configuration with 30 rows without misfit ($\Delta = 0$), at $T = 0.3$. The inset in part (a) compares the effective temperatures $T_{\text{eff},x}$ (solid lines) and $T_{\text{eff},y}$ (dotted lines) for $v = 5.0$, $v = 1.0$, $v = 0.5$ and $v = 0.1$ (from top to bottom).

If we would include an explicit solvent (which would require orders of magnitude more computer resources, and hence is not attempted) it is likely that the corresponding enhancement of the effective temperature near the walls is much smaller, since the explicit solvent acts as a more efficient thermostat.

Of course, using only implicit solvent is a very simplified model and might dampen or enhance some effects which we are going to discuss in this chapter. But simulations with explicit solvent molecules are not straightforward either, as it is impossible to simulate the number of particles necessary for such simulations with standard molecular dynamics. Therefore, one needs more sophisticated approaches which integrate the motion of the solvent particles approximately like for example the multi-particle collision dynamics method of Kapral and Malevanets [152, 153]. But this would not only have required substantial implementation work, but it would also have slowed down the simulations, which would then again have required to replace our simple shared memory parallelization with a message passing one. Therefore we used only implicit solvent particles.

Since near the walls the effective temperature extracted from the x and y-components of the velocities of the particles disagree, it is clear that the "fluid layers" near the

moving walls are completely out of equilibrium, since the concept of a "local temperature" which is anisotropic does not make much sense. However, for small velocities the "temperature" profiles $T_{\text{eff},x}(y)$ and $T_{\text{eff},y}(y)$ agree within statistical errors, and the concept of a "local temperature" in the slit interior can be used. Then the observed profile of this local temperature $T_{\text{eff}}(y)$ can be interpreted as follows: due to the large friction between the fluid-like layers and the moving walls, these layers act like a source where heat is constantly pumped into the system. This heat is transported via conduction into the interior of the slit (due to the action of the thermostat, heat is removed everywhere in the slit, and a steady-state temperature profile is established). Motivated by corresponding solutions of the heat conduction equation, we can fit these local temperature profiles by $T(y) = A_0[exp(-z/\lambda)+exp(-(D-z)/\lambda)]+A_1$, where A_0, A_1 and λ are phenomenological parameters that depend on v. Unfortunately, due to the large fluctuations the fitting of three parameters is somewhat uncertain and hence we do not dwell on the velocity dependence of these parameters. It would be interesting to study how this dependence changes when the friction constant is varied, but a study of this problem would require very large computational resources and hence is beyond the scope of the present work.

We emphasize, however, that for small velocities ($v < 0.5$) the deviations of the temperature profile from a constant (which is the temperature defined by the thermostat) are almost negligible. But already for these small velocities pronounced shear banding occurs (see next section). Clearly, the non-uniform temperature profiles are not the primary cause for the structural change caused by the shear, and thus it is legitimate to disregard the nonuniformity of the temperature in the following.

4.2 Effect of shear on colloidal crystals

Without a misfit (i.e. $\Delta = 0$), where the crystal consists of 30 rows, slow shearing of the walls has a relatively large effect on the velocities of the particles. Fig. 4.3 shows velocity profiles obtained by sorting the particles into rows depending on their position in the y-direction and then calculating the average particle velocity for each row of particles. As the maximum average particle velocity is given by the shear velocity of the walls, we normalized the velocity profiles by the shear velocity. But we also show the non-normalized velocities in an inset of the graphs (fig. 4.3) as a higher absolute velocity will lead to more disorder in the crystal, while the normalized velocities indicate how strong the effect of the shearing is.

At a temperature of $T = 0.3$ and for the case of $\Delta = 0$ this results in velocity profiles (fig. 4.3a) where the two smallest shear velocities ($v = 0.1$ and $v = 0.3$)

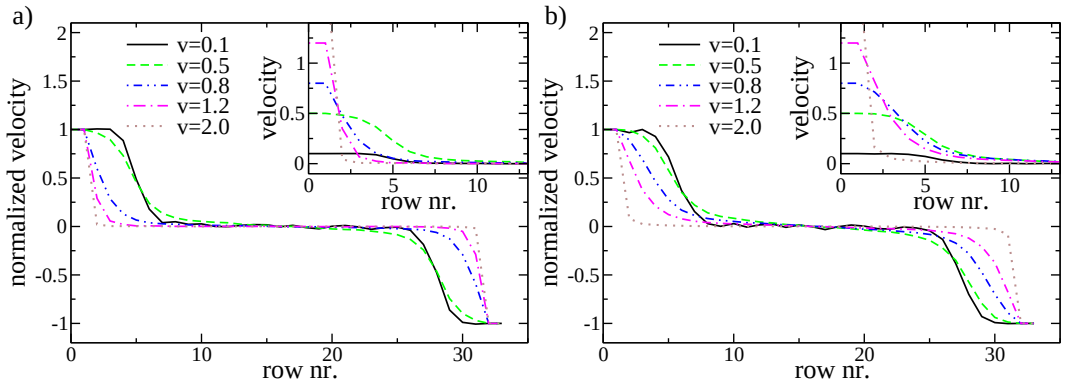

Figure 4.3: Velocity profiles, normalized by the velocity of the wall labelled as row number zero, for different shear velocities of the walls as indicated. Starting configuration with 30 rows without misfit ($\Delta = 0$), for two temperatures $T = 0.3$ (a) and $T = 0.5$ (b). Inserts show the unnormalized velocity profiles.

lead to the (relatively) largest particle velocity in the first $4 - 5$ rows closest to the walls. This means that slow shearing of the walls has the strongest effect on pulling the particles along with the walls. Of course, if one compares the absolute, non-normalized velocities inside the crystal, these velocities are larger at a shear velocity of $v = 0.3$ and $v = 0.5$, as particles next to the walls obtain a higher velocity due to the faster walls, even if a smaller percentage of the walls' velocity is transferred to the particles next to them. The higher absolute velocity also leads to more disorder inside the crystal, which then leads to a stronger influence of the shearing even on particles in the inner rows of the crystal. Thus, there is clear evidence for shear band formation, as will be discussed below.

This disorder is also reflected in the density profiles (fig. 4.4) and in the angular distributions (fig. 4.6a). The density profiles show clear peaks indicating a crystalline structure for higher shear rates, but at a shear rate of $v = 0.3$, the peaks corresponding to the inner rows of the crystal are almost non-existent any more. This can be explained by the changes in the crystalline structure discussed below.

Obviously the profiles of the velocity never resemble the (approximately) linear velocity profiles representing simple Couette flow, that one encounters when one shears simple [154] or complex [155, 156] fluids and uses a thermostat which includes hydrodynamic effects. This is mainly due to the fact that we are shearing a crystalline solid here. But the Langevin thermostat which we are using also alters the flow profiles in the liquid phase as we will show on page 94 ff.

The shearing of the walls leads (at certain shear rates) to a tilting of the crystalline

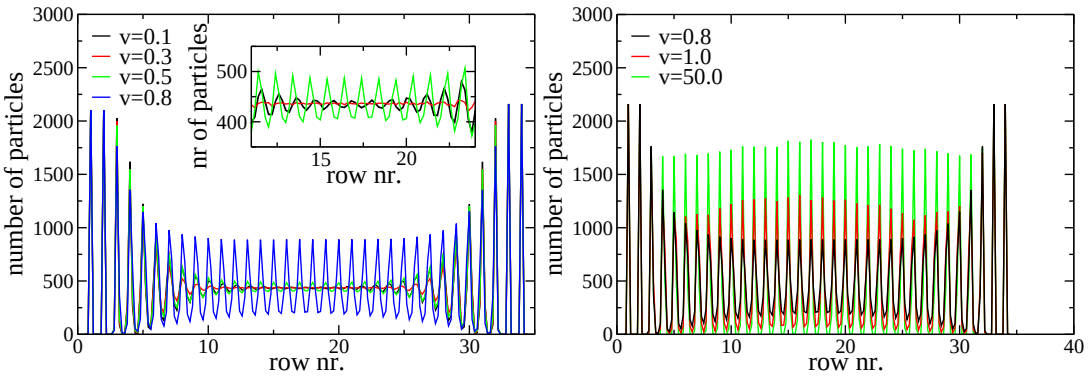

Figure 4.4: Density profiles. Simulations were carried out at a temperature of $T = 0.3$ for a system with 30 rows without a misfit ($\Delta = 0$). Shear velocities of the walls as indicated. The strongly oscillating profile represents $v = 0.8$ and was omitted in the inset of the graph on the left, where a magnified plot of the central part of the slit is shown. The normalization of the density profile $\rho(y)$ is given in terms of the total number of particles, $N = \int_0^D \rho(y)dy$.

layers and even to breaks in the crystalline structure, where parts of the crystal are oriented in a different direction from the rest. This effect is illustrated in the snapshots shown in fig. 4.5 and it is also shown in a short movie which is included in the CD-Rom accompanying this thesis. In order to analyze it quantitatively, we computed for each pair of two neighbouring particles the angle between the line connecting these two particles and the x-axis. In a perfect hexagonal lattice without misfits and without defects, this would lead to peaks at $0°$, $60°$, $120°$ and $180°$ (we did not compute any angles larger than $180°$).

At a shear velocity of $v = 0.1$, the peaks are centered around slightly larger angles due to a tilting of the crystalline layers which is induced by the shearing (fig. 4.5a and fig. 4.6). At shear velocities of $v = 0.3$, $v = 0.5$ and (less pronounced) of $v = 0.8$ the angular distribution has two peaks as the crystal breaks into several pieces and generally only the layers close to the walls are aligned with the walls (creating a peak in the angular distribution close to $60°$, $120°$ etc), while the crystalline parts inside of the crystal prefer a different orientation, thus creating the second peak in the angular distribution (fig. 4.5b and fig. 4.6). These two peaks are very distinct at $v = 0.3$, while at $v = 0.5$ there is more disorder inside of the crystal due to the higher shear velocity. Starting from $v = 0.8$, this second peak disappears again as the walls are moving too fast to have much influence on the crystalline structure any more. This is due to the fact that the fast shearing of the walls leads to an averaged out wall potential which the particles next to the wall feel, which is not able to drag particles along with the walls any more.

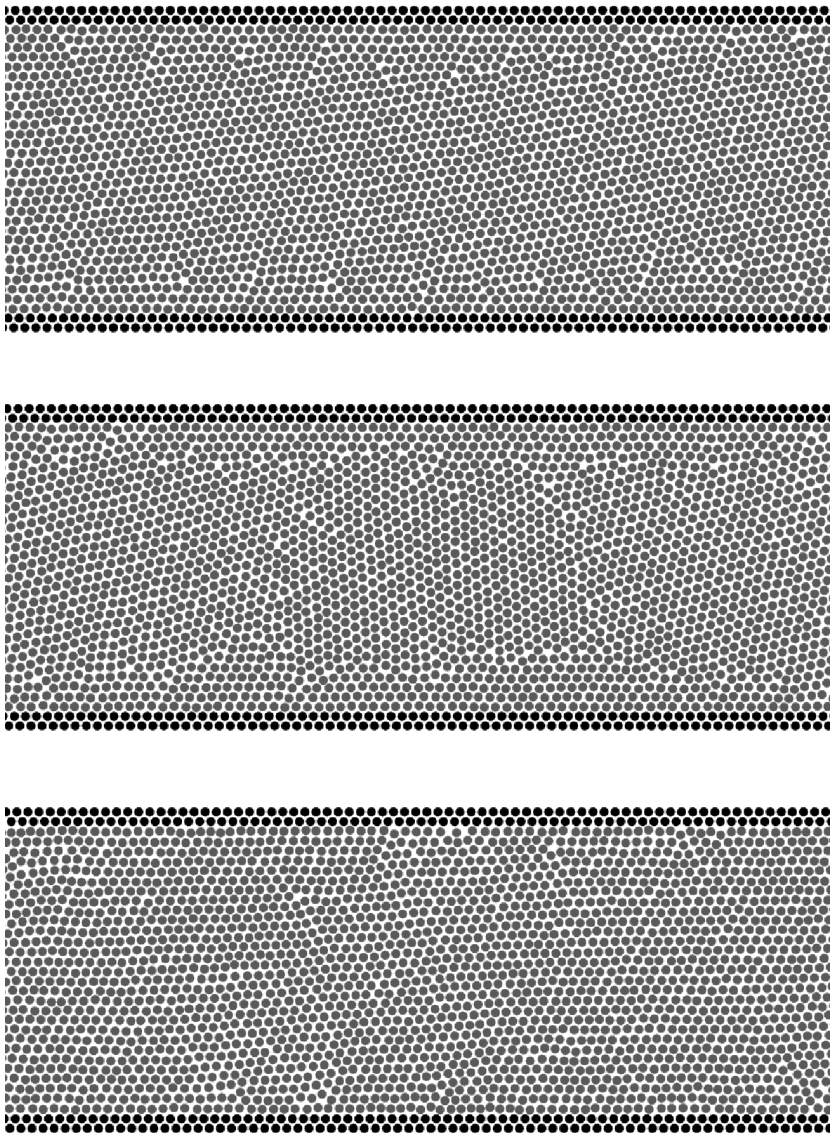

Figure 4.5: Snapshots of a section of a system with sheared walls. The starting configuration contained 30 rows and the simulation was carried out at a temperature $T = 0.3$ and without a misfit ($\Delta = 0$). The particles in the two first rows on top and the two last rows at the bottom (that are at rigidly fixed positions relative to one another and contribute the moving walls) are highlighted by black dots while the mobile particles are shown as grey dots. Shear velocities of the walls were chosen as (from top to bottom) $v = 0.1$, $v = 0.3$ and $v = 0.8$

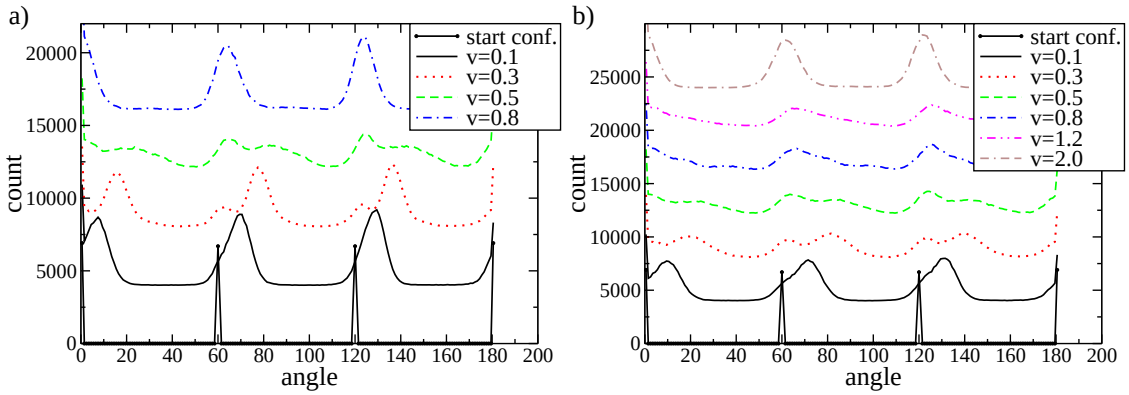

Figure 4.6: Distributions of angles between the line connecting each pair of two neighbouring particles and the x-axis. Shear velocities of the walls as indicated. The graphs for different shear velocities are shifted vertically by 4000 in order to give a better overview. Starting configuration with 30 rows without misfit ($\Delta = 0$), temperature $T = 0.3$ (a) and $T = 0.5$ (b).

It is interesting to note that the above results may be understood as follows. Firstly, at low velocities, the velocity profile shown in fig. 4.3 may be interpreted as being composed of three prominent shear bands [157], a feature of a typical non-Newtonian, shear-thinning material. The two fast moving bands lie close to the boundaries and flow in opposite directions sandwiching a central immobile region. In some respects our flowing solid therefore behaves like a moving paste, or soft-glassy matter [158] in a fashion which is complementary to that seen in the experiments of Coussot et al. [159] where a central mobile region is flanked on either side by immobile shear bands adjacent to the boundaries. As the shear rate is increased, the width of the mobile shear bands initially increases as expected. In order to verify that we indeed do have shear banding in our system, we plot the average stress as a function of shear rate in fig. 4.7. "Average stress" means here that the stress was computed for all particles in the system via the virial formula. In order to exclude any effects caused by the walls, only particles which were at least 1.5 times the cutoff distance away from the walls were taken into account for the averaging as stress profiles suggested that the stress of these particles was not influenced by the walls any more.

The resulting flow curve shows non-monotonic behavior typical of shear thinning systems. However, surprisingly, instead of obtaining a linear Newtonian region at high shear rates, the stress stabilizes to a constant signifying the presence of a shear band of vanishingly small viscosity. Referring back to the calculated velocity profiles, (see fig. 4.3) we observe that the width of the shear bands decreases with increasing velocity in this regime, so that at large velocities (shear rate), we obtain thin, highly mobile boundary layers near the walls while most of the solid is immobile. For such

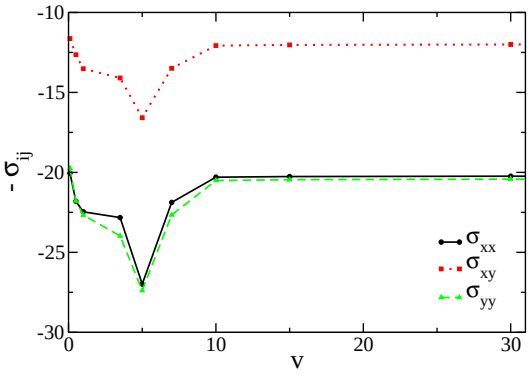

Figure 4.7: Flow curve for $T = 0.3$ and starting configurations with 29 rows at a misfit of $\Delta = 2.2$. σ_{xx}, σ_{xy} and σ_{yy} denote the respective components of the stress tensor (as defined in Eq. 1.6), while v indicates the velocity with which the walls are being moved.

velocities, the solid re-crystallizes.

Further, in order to characterize the behavior of the solid at high wall velocites, we refer to the plot of the anisotropic, local, effective temperature (obtained by fitting a Gaussian to the probability distribution of the x- and y-components of the velocity) already shown in fig. 4.2. We observe that both these effective temperatures show non-monotonic behavior, initially increasing and then decreasing as the velocity increases leading to re-crystallization. Regaining crystalline order with high drive velocities is also seen in crystals driven over random pinning potentials [160]. This implies that our system *never* shows a Newtonian regime at any flow velocity if the temperature is small enough to obtain crystallization.

But also the liquid observed above the melting transition does not exhibit a Newtonian flow profile if one uses a bulk Langevin thermostat: As the Langevin equation of motion contains friction and random noise, the shear exerted by the walls is screened by the particles in the layers close to it and does not necessarily lead to a motion of all particles in the system. Mathematically, the presence of friction and random noise in the Langevin equation leads to a modified Navier-Stokes equation. This modification arises from the fact that the Navier-Stokes equation is equivalent to Newton's equations of motion, which do not contain friction or random noise. Solving this modified Navier-Stokes equation yields the following velocity profile (in the simplified case of constant viscosity η_{app} throughout the system, which can differ from the bulk viscosity η_0 and is a reasonable approximation at relatively slow shear rates) [63, 161]:

$$u(y) = u_0 \frac{\sinh(\sqrt{\frac{\rho\gamma}{\eta_0}}y)}{\sinh(\sqrt{\frac{\rho\gamma}{\eta_0}}\frac{D}{2})} \tag{4.1}$$

where u_0 indicates the velocity of the mobile particles (as opposed to the velocity v, with which the walls are moved forward). y is defined in the range between $-\frac{D}{2}$ and $\frac{D}{2}$, $\rho = 1.05$ is the particle density and $\gamma = 0.5$ is the friction constant of the Langevin

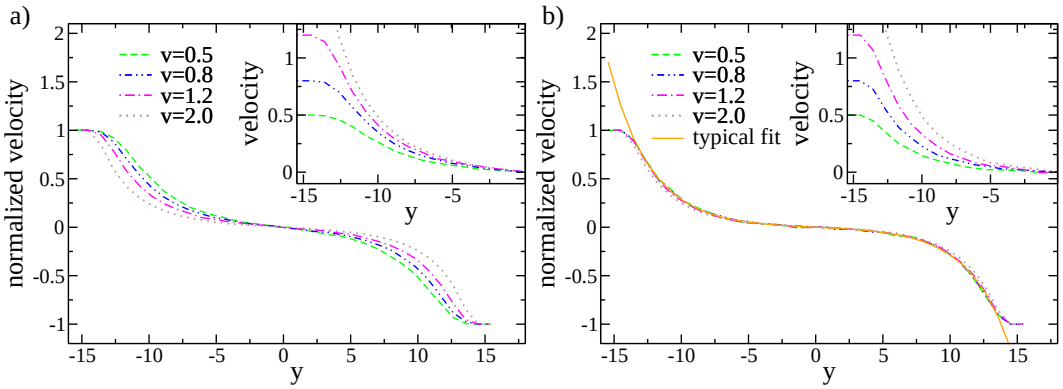

Figure 4.8: Velocity profiles for $T = 2.0$ (a) and $T = 5.0$ (b). Shear velocities of the walls as indicated. Starting configuration with 30 rows without misfit ($\Delta = 0$). For $T = 5.0$, the hyperbolic sine (Eq. 4.1) fitted to the velocity profile of $v = 0.8$ is shown as an example of the fitted curves.

thermostat as before. The variable u_0 describes the velocity of the mobile particles next to the walls and should be smaller or equal to the wall velocity.

In our system strong surface effects are present due to the corrugated nature of the walls. Thus, the shape of the velocity profiles we have obtained differs from the pure hyperbolic sine given in Eq. 4.1 in that the part close to the walls is slightly flattened (fig. 4.8). Therefore we had to omit the velocities of the particles close to the walls (we used the region between $-0.85 \cdot \frac{D}{2} \leq y \leq 0.85 \cdot \frac{D}{2}$) in order to obtain a good fit. Additionally, we had to use D in Eq. 4.1 as a fit parameter, because the effective width D_{eff} of the stripe, in which the hyperbolic sine can be observed, is smaller than the (given) whole width $D_0 = 29.0617$.

Fig. 4.8b shows a typical fit to the velocity profiles obtained at a temperature of $T = 5.0$. Normalized to the same wall velocity, the curves collapse, allowing us to average over the fitted values. Thus, we obtained a bulk viscosity of $\eta_0 = 5.372 \pm 0.066$ and an effective width of $D_{\text{eff}} = 27.76 \pm 0.17 = (0.9551 \pm 0.0058) \cdot D_0$.

Fig. 4.8a illustrates that at $T = 2.0$, which is clearly above the bulk melting temperature of $T = 1.35$, this theory does not hold yet. The curves for different wall velocities can be fitted with the same hyperbolic sine function, but yield different values for the viscosity as well as for the effective width of the system. With higher shear velocity, the viscosity decreases and the effective width of the hyperbolic sine profile increases as shown in Table 4.1. This can be explained by layering effects close to the walls – as the structured walls have the effect of crystal nuclei – and the generally still more "structured" order of the particles (in comparison to higher

temperatures like $T = 5.0$). Shearing this system leads to a melting of the structures close to the walls. Higher shear velocities therefore increase the viscosity up to a value which is comparable to the viscosity at $T = 5.0$. Likewise, the effective width which we obtained by shearing the walls with a velocity of $v = 2.0$ is comparable to the effective width we obtained at $T = 5.0$.

Table 4.1: Viscosities and effective widths obtained at a temperature of $T = 2.0$ by fitting the curves shown in Fig. 4.8a with the hyperbolic sine given in Eq. 4.1.

v	η_0	D_{eff}
0.5	7.24034	25.0108
0.8	6.25431	25.7628
1.2	5.76804	26.9726
2.0	5.31775	27.930

But as the main focus of this work is on the crystalline phase, we are returning to significantly lower temperatures again: if one compares different temperatures (but both of them clearly below the melting temperature, for example $T = 0.3$ and $T = 0.5$), it is at higher temperatures energetically easier for the crystal to split up into several domains, which can then be tilted with respect to the walls and can be oriented in different directions. Therefore the velocity profiles at temperature $T = 0.5$ have a more pronounced shape even at higher shear velocities (see fig. 4.3b). The same effect is visible in the angular distributions (fig. 4.6b): The "second peak" in the angular distributions only disappears at considerably higher shear rates than in the case of $T = 0.3$. Apart from this, all shear rates at $T = 0.5$ lead to higher average particle velocities than in the case of $T = 0.3$ as the higher temperature makes it easier for particles to move along with the walls.

A different picture arises if one introduces an incommensurability between the crystal and the walls into these simulations. As described at length in Chapter 1.1, this means that the structured walls are placed closer together. In simulations without shearing, this would lead to the creation of a soliton staircase [1] (compare Fig. 1.4). It is also already known that there is a significant hysteresis in the transition between structures with 30 rows and structures with 29 rows with the same overall number of particles. These structures with 29 rows are the energetically preferred configuration for misfits greater than about $\Delta = 1.7$, but if a simulation is started with a structure of 30 rows, it will not spontaneously change its structure to 29 rows (in simulations without shear) until about a misfit of $\Delta = 2.0$. But even at larger misfits, simulations without shear have to be equilibrated for a certain time until this transition takes place. This transition happens much faster when sheared walls are introduced into the system. For example, for a system starting with 30 rows at a misfit of $\Delta = 2.2$ and at a temperature of $T = 0.3$, the system still consisted of 30 rows after 1 million time steps in the case without sheared walls, but had already 29 rows after just 20000 time steps in the case of a simulation where the walls were sheared with a velocity of

$v = 0.5$. As will be discussed later on, at this shear velocity the structure breaks and changes again if the simulation run is continued.

In the following, we will concentrate on simulations at a misfit of $\Delta = 2.2$, which leads to a structure with 29 rows independently of whether the starting configuration contained 30 or 29 rows. It is interesting to investigate the structures which develop here as they do not contain solitons any more due to the shearing of the walls. Instead, it is now possible for the system to re-arrange its particles continually in a way that no particles have to sit on the maxima of the potentials, as there is enough disorder in the system, especially close to the walls.

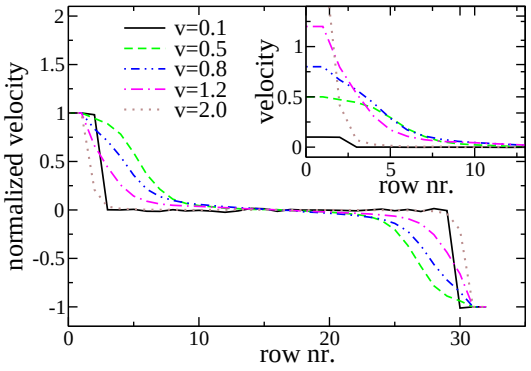

Figure 4.9: Velocity profiles, normalized by the velocity of the wall labelled as row number zero. Shear velocities of the walls as indicated. Temperature $T = 0.3$. Starting configuration with 29 rows at a misfit of $\Delta = 2.2$. Insert shows the unnormalized velocity profile.

There are several mechanisms of dealing with the different number of particles in the different rows which lead to the formation of solitons in the case without shear. At low shear rates and if the starting configuration already contains 29 rows, the row next to the walls (which contains the same number of particles as the wall rows, but less than all of the inner rows), moves along with the walls, while the inner rows remain almost without movement (fig. 4.9, curves for $v = 0.1$ and $v = 0.3$). This would in principle lead to solitons which are moved along with the walls as the rows directly adjacent to the walls still do not have the same crystalline structure like the inner rows. But as these rows are moving, the particles they contain are not always at the ideal lattice positions and therefore the solitons are strongly "smeared out".

If one starts with a structure of 30 rows at the same shear rate, the structure changes into 29 rows. Apart from equilibration effects, we obtained the same results as in the case where we started with a well-defined 29-row-structure.

At slightly higher shear velocities (around $v = 0.8$), the same effect as in the case without misfit is observed: The crystalline layers are tilted and the inner part of the crystal breaks off from the rest and changes its orientation, thus creating a rather strong flow in the layers close to the wall and less flow inside of those parts of the crystal, which have turned around. In this case, the solitons are a part of the general disorder and therefore not clearly visible any more. The change of the structures

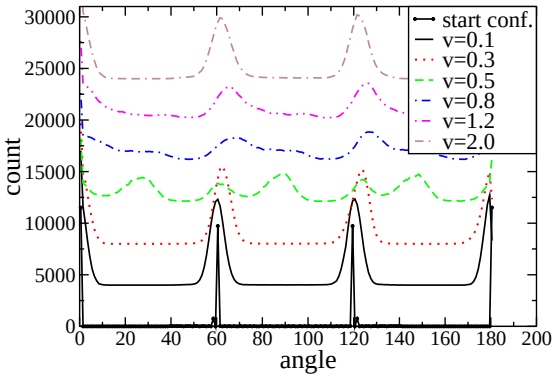

Figure 4.10: Angular distributions. Shear velocities of the walls as indicated. The graphs for different shear velocities are shifted vertically by 4000 in order to give a better overview. Starting configuration with 29 rows at a misfit of $\Delta = 2.2$. Temperature $T = 0.3$.

becomes visible in the angular distributions shown in fig. 4.10. It is also observable in the density profiles shown in fig. 4.11: Unlike in the case without misfit, at very small shear rates clear peaks in the density distribution (and peaks around $60°$, $120°$ etc in the plots of the angular distribution) indicate an ordered crystalline structure as only the rows directly adjacent to the walls move along with the walls, while the particles in the inner part of the crystal remain more or less in their ideal positions. At shear rates around $v = 0.8$ the inner part of the crystal breaks into several domains in the same way in which it does this around $v = 0.3$ in the case without misfit, which again leads to strongly smeared-out peaks in the density distribution. Thus, this effect is shifted to slightly higher shear rates due to the presence of the solitons.

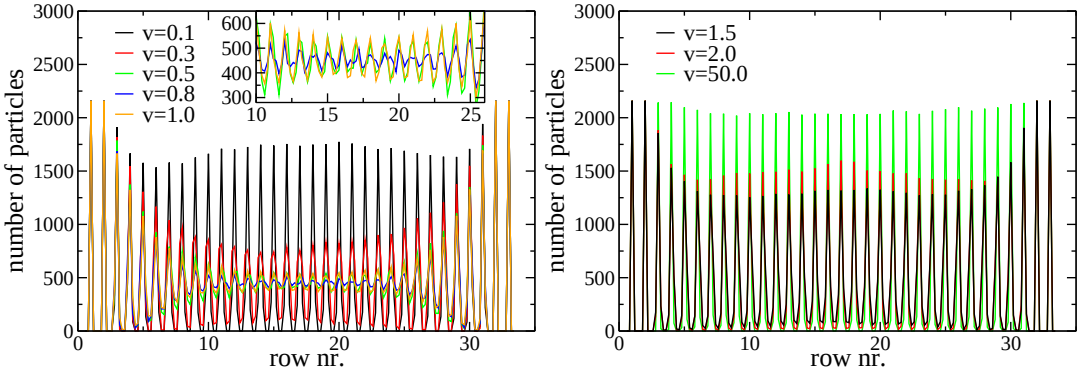

Figure 4.11: Density profiles. Simulations were carried out at a temperature of $T = 0.3$ for a system with 30 rows at a misfit of $\Delta = 2.2$. Shear velocities of the walls as indicated. The strongly oscillating profile represents $v = 0.8$ and was omitted in the inset of the graph on the left, where a magnified plot of the central part of the slit is shown. The normalization of the density profile $\rho(y)$ is given in terms of the total number of particles, $N = \int_0^D \rho(y)dy$.

This is also illustrated in the snapshots shown in fig. 4.12: At $v = 0.3$ the structure is still almost perfectly crystalline as only the outermost rows move along with the

walls. The incommensurability between the non-moving inner part of the crystal containing the extra particles and the rows directly adjacent to the walls which contain no extra particles, but move along with the walls, can only be observed by very close inspection of the two rows next to each wall, but is almost invisible in the presented snapshots. At a velocity of $v = 0.8$ the inner part of the crystal breaks into several domains, and at even higher shear velocities the crystalline structure is re-established, albeit slightly more disordered than in the case without a misfit.

At even higher shear rates, less and less particles are dragged along with the walls, decreasing the influence of the shearing on the crystalline structure again. Still, due to the shear there is enough disorder in the rows close to the walls that there are no distinguishable solitons. The fact that the density profile for $v = 50.0$ has higher peaks in the case with a misfit of $\Delta = 2.2$ (compared to the case without a misfit) is of course only due to the fact that the inner particles are arranged into 29 instead of 30 rows and therefore there are more particles per row. Please note that the x-axis is chosen as the row number. In most of the density profiles the peaks in the middle of the stripe are more pronounced than in the rows number 5, 6 and 7, as the rows very close to the walls tend to move along with the walls, while the inner rows tend to stay in their initial position, which leads to some disorder in the rows between the moving and the non-moving parts of the crystal. Only in the case where the middle of the crystal breaks into several pieces there is more disorder (and thus less pronounced peaks in the density distribution) in the middle of the crystalline stripe than anywhere else.

Here, it is interesting to study the case of very high shear velocities ($v = 50.0$) as the shearing seems to stabilize the structure with 30 rows. So, if the starting configuration contains 30 rows which contain the same number of particles in each row and therefore no solitons, this structure is stabilized by the fast moving walls.

If the starting configuration contains 29 rows and the appropriate number of extra particles in the inner rows, a different effect can be observed: As the structured walls are moving very fast, the rows directly adjacent to the walls only feel an averaged-out wall potential and are thus not stabilized in a structure with the same number of particles as the walls any longer. Therefore it becomes energetically preferable for these rows to contain the same number of particles like the inner rows, which contain extra particles. But as the number of particles in the crystal is constant, there are no particles to fill up the outer rows. Due to this, holes are created in the outer rows which take the role of additional particles. These holes can even diffuse further inside the crystal. A snapshot showing this effect is presented in fig. 4.13.

Re-running all of these simulations at the same misfit and a higher temperature ($T = 0.5$) leads to results that can be expected from the case without misfit: As there

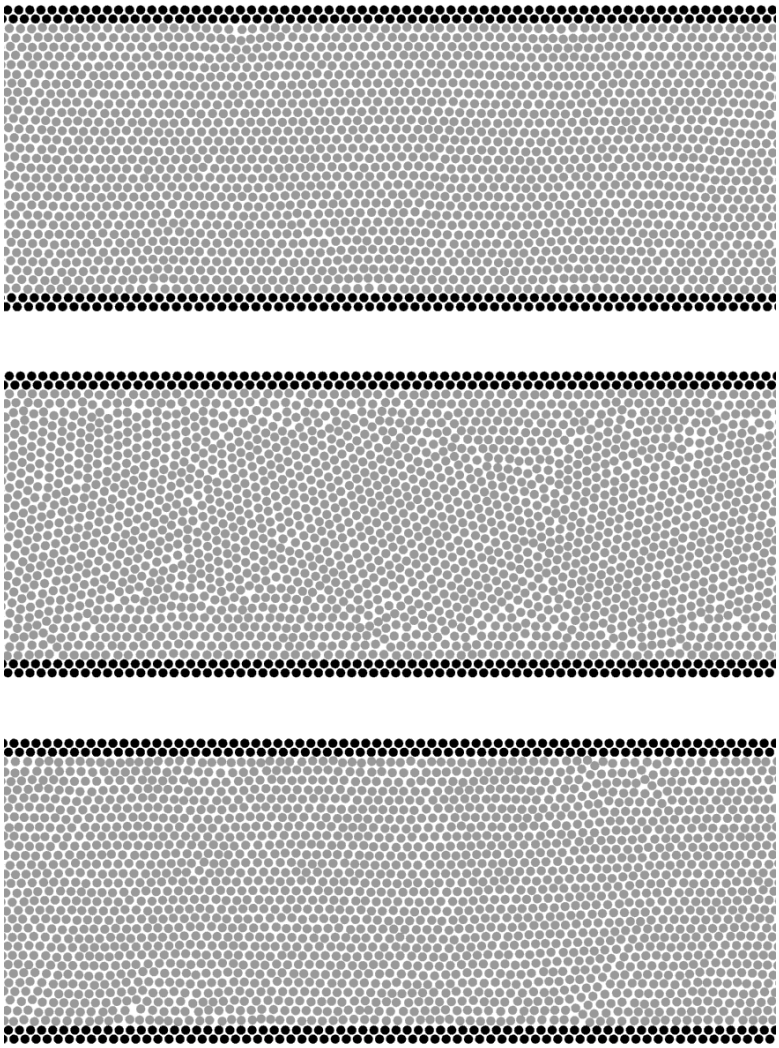

Figure 4.12: Snapshots of a section of a system with sheared walls. The starting configuration contained 29 rows and the simulation was carried out at a temperature $T = 0.3$ and at a misfit of $\Delta = 2.2$. The wall particles which are moved forward with constant velocity are highlighted by black dots while the freely moving particles are shown as grey dots. Shear velocities of the walls were chosen as (from top to bottom) $v = 0.3$, $v = 0.8$ and $v = 2.0$

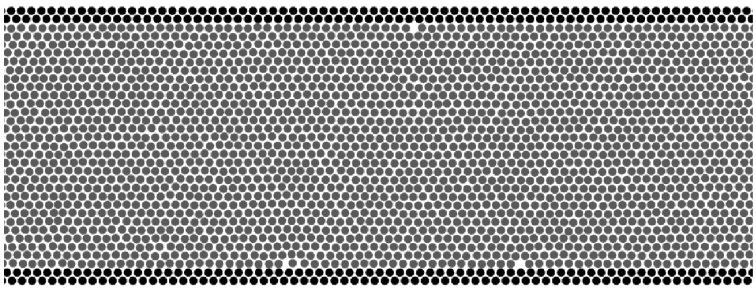

Figure 4.13: Snapshot of a section of a system with sheared walls. The starting configuration contained 29 rows and the simulation was carried out at a temperature $T = 0.3$ and a misfit of $\Delta = 2.2$. The high shear velocity of the walls ($v = 50.0$) leads to the creation of holes.

is generally more disorder in the system if the temperature is higher, the velocity profiles become more pronounced for higher shear rates. In addition, the crystal starts to split up into several domains and to change its orientation at lower shear rates already than in the case of $T = 0.3$.

Another interesting property of these systems is the time-dependence of the mean square displacement of the particles. In this chapter we consider the $\text{MSD}_{\text{time-diff}}$ only, which is defined as $MSD =< [x_i(t + t_0) - x_i(t_0)]^2 >$, where the average $< ... >$ includes an average over all particles in a row and over the initial time t_0 (see Sec. 1.1). We are only presenting results for the MSD in the x-direction parallel to the walls here.

The assignment of particles to rows is done according to the initial position of each particle at the beginning of the time interval Δt used as abscissa variable here since in the course of time particles change their rows.

As described above, in cases with a misfit of $\Delta = 2.2$ and at low shear velocities ($v = 0.1$), only the outermost row of particles moves along with the walls. This leads to an MSD as shown in fig. 4.14, where the MSD of the particles in the first row is an almost perfect quadratic curve of the form $MSD = a \cdot t^2$. As the MSD is the quadratic displacement, this means that the fit parameter $a = v^2$, v being the velocity of the particles in this row. As one can read off from the graph, the velocity of the particles in this case is almost exactly the velocity with which the walls are being sheared. The MSD of the rows next to the outermost one have significantly smaller values and a periodic shape as the particles in these rows are trying to cope with the moving walls. The MSD of the inner rows is almost constant and independent of the walls, which means that the particles just move around randomly.

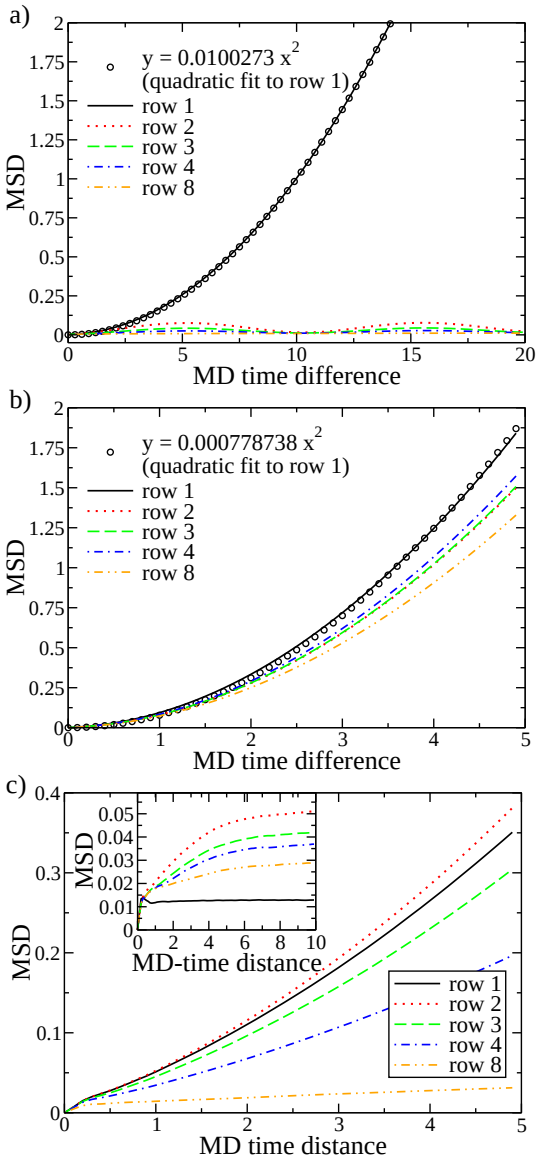

Figure 4.14: MSD (in x-direction) of the particles in different rows. The starting configuration contained 29 rows in every case and the simulation was carried out at a temperature $T = 0.3$ and a misfit of $\Delta = 2.2$. (a) The shear velocity of the walls were chosen as $v = 0.1$. The oscillation is due to the movement of the wall particles which leads to an oscillating wall potential for the particles next to the walls. (b) Shear velocity $v = 0.5$, (c) $v = 1.2$. The inset shows the MSD in the case without shearing for comparison.

At a shear velocity of $v = 0.5$ (fig. 4.14b), where the orientation of all the inner parts of the crystal changes, the MSD looks completely different: The particles in the first row are still moving more than the ones in the inner rows, but as the particles of all rows are mixing in the course of the simulation, the MSDs of different rows are getting more similar the longer the simulation runs, until finally the particles of all rows are equally distributed in the crystal and the MSD of particles stemming from different rows cannot be distinguished any more. Besides, all values of the MSDs are very large here (note the different scale of the y-axis in fig. 4.14c in comparison to the y-axes in fig. 4.14a,b).

At even higher shear velocities, where no parts of the crystal change their orientations any more, the values of the MSD are generally smaller again. As illustrated in fig. 4.14 (c), the MSD in the row directly adjacent to the walls is the second largest one and cannot be fitted with a quadratic curve of the form $MSD = a \cdot t^2$ any more. This is due to the fact that the particles' movement is not primarily the movement along with the walls any more. The MSD in the row next to this row is larger. This is due to the incommensurability of the different lattice spacings. The row directly adjacent to the walls originally contained as many particles as the walls while the inner rows contain extra particles due to the disappearance of one row because of the misfit. In the rows further inside of the crystal, the MSD is smaller as the effect of the shear and of the incommensurabilities becomes smaller.

If one compares the MSD of these simulations under shear with simulations without shear at the same misfit, the effect of the solitons becomes visible (see fig. 4.14, inset of graph c): In the case without shear, the particles in the row directly adjacent to the wall do not move much as their structure is commensurate with the walls and the walls are not moving. Therefore their MSD is the smallest one and even shows the overshoot, which one would expect to see in a crystal with harmonic potentials where the particles are swinging around their ideal lattice positions with a certain periodicity. The MSD of the rows adjacent to this one are significantly larger in this case as the solitons are located in these rows, which causes the particles to move around more. In the inner rows, the MSD becomes smaller again as there are no solitons in these rows. This is clearly different from the values of the MSD in the case with shear, where no clearly definable solitons are created and therefore all of the outer rows exhibit comparable values of the MSD as the incommensurabilities are shared between these rows and lead to a lot of movement. Besides this, the shape of the curves is different and the absolute values of the MSD are larger as the shearing leads to a small, but detectable movement along with the sheared walls, while in the case without shear no direction is preferred.

Finally, we ask the question whether there are experimental results available that shed some light on the phenomena studied by our simulations. in this context, we

draw attention to a recent study of melting and crystallization of colloidal hard-sphere suspensions under shear [135]. This work refers to a three-dimensional colloidal crystal, of course, and necessarily also includes solvent. In these experiments the crystals always melted at the highest shear rate. Again, this might be an effect of the solvent which strives to have a smooth velocity profile, while crystalline bands would probably cause a step-wise solvent velocity profile. If so, this would mean that the highest shear rates applied in our model simulations might not be accessible in a real colloidal crystal, because there the explicit solvent favours shear melting.

A further interesting experiment was performed for a system of strongly charged polystyrene spheres in water, that form a two-dimensional triangular crystal at the bottom of the container [118]. By interfering laser beams, one can expose the system to a periodic potential, which can be chosen either commensurate or incommensurate with the crystal. Translating the container with velocity v, lateral Stokes forces ($F \propto v$) are applied to all particles. It was found that in the commensurate case the motion of the layer was associated with soliton or antisoliton formation throughout the crystal. These kinks and antikinks are extended in the direction perpendicular to the direction of the velocity, creating extended compression zones [118]. Of course, this feature is different from the situation studied in the present model, where a periodic potential acts only on two parallel boundaries of a two-dimensional crystal, rather than on all particles of the crystal. Therefore soliton excitations in the present model (occuring already in the static case when the transition from n to $n-1$ rows has occured) have only a rather small extension in the direction perpendicular to the walls. It should also be noted that such kinks and antikinks are well-known concepts in the context of friction between two crystalline surfaces formed from atoms [162–164], but again then two two-dimensional lattices slide against each other, while in our case we have sliding of one-dimensional boundaries confining a two-dimensional crystalline strip. Thus, a direct application of these well-known studies is not straightforward.

4.3 Concluding remarks

In this chapter we have discussed the influence of shear on the structure of a two-dimensional colloidal crystal in confinement between parallel walls. We observed that in the case where the crystal is commensurate with the periodicity of the boundary, at slow shear velocities the layers of the crystal are tilted, while the crystal breaks into several pieces with different orientations at medium shear velocities and remains almost undisturbed at high shear velocities. We showed that the distribution of angles inside of the crystal is an important quantity and gives a good insight into the structure of the crystal, along with velocity profiles.

In the incommensurate case, however, the behaviour is slightly different, especially at low and at high shear rates. At low shear rates, only one single row of particles moves along with the walls and at high shear rates holes are created in the structure. But the breaking up into several pieces also occurs at slightly different shear velocities. This is due to the incommensurability between the periodicity of the crystal and the periodicity of the rigid boundaries, which would lead to the creation of solitons in the case without shear. Obviously, the shearing of the crystal changes this behaviour significantly.

However, we caution the reader that the observed shear banding effects could be somewhet exaggerated due to the lack of explicit solvent, as well as the enhancement of effective temperature near the walls. It is possible (but due to the lack of enormous computing resources that would be needed we cannot test this hypothesis) that all of these effects are weaker when explicit solvent is included.

Clearly, our results are somewhat qualitative. One could in principle run more simulations at different temperatures and different shear velocities in order to investigate the occuring structural transitions (e.g. from 30 to 29 rows and order-disorder-transitions) with higher precision. But this does not seem very sensible at this moment because there is no theory with which the results could be compared and because experiments with such colloidal systems are possible [33–37, 41–46, 49, 148], but typically use slightly different parameters for the particle interactions, the box sizes and the walls. Therefore a rather qualitative study makes sense in this particular case and helps to understand the complex interplay of confinement and shear and its influence on the structure formation of colloidal crystals.

Summary and Outlook

In this work we have thoroughly investigated a two-dimensional, monodisperse, crystallized colloidal system by means of computer simulations. We have considered a system confined by walls consisting of two rows of frozen particles in one direction and periodic boundary conditions in the other direction. This choice of walls stabilizes the hexagonal crystalline structure. The particles were interacting via a purely repulsive r^{-12}-potential, which was also acting between the mobile particles and the wall particles. In order to make the potential strictly short-ranged, we introduced a cutoff at roughly 2.5 times the next neighbour distance in the crystalline structure. To avoid jump discontinuities, we added a shift to the potential, and in order to make it differentiable, which is important for the computation of the stress tensor, we multiplied it with a smoothing function. We did not simulate any explicit solvent particles.

A system similar to this one is experimentally realizable [29, 33–37, 41–46], for example by using polystyrene spheres with a superparamagnetic core, which interact via a purely repulsive dipole-dipole interaction potential when exposed to a magnetic field. Such particles can be trapped at air-water-interfaces, where they can form a two-dimensional layer. Of course, such a dipole-interaction would lead to an r^{-3}-potential. But as there are no experiments available at the moment to which we could directly compare our results, we preferred to use the computationally more convenient (short ranged and therefore less time consuming to compute) r^{-12}-potential.

Compressing the crystal leads to a structural transition in the course of which one of the crystalline rows disappears. As the number of particles in the system is constant, the particles which used to sit in this row have to be distributed in the remaining rows. This leads to the development of regions in the crystal where the lattice structure is incommensurate with the walls and also with the inner part of the crystal. Such high energy regions are called solitons. Preceding work on this model system by Chui et al. has already discovered this structural transition and the associated formation of a soliton staircase [1–3].

In the first part of this thesis we are revisiting the structural transition. Chui et

al. [1–3] have already tried to locate the transition by computing the anisotropy of the stress tensor which exhibits a jump discontinuity at the value of the misfit where the structure spontaneously rearranges itself into a different number of rows. These stress curves, however, indicate a large hysteresis around the transition point, which obscures its exact location. In order to resolve it with higher precision, we have applied two different Monte Carlo methods which are able to determine the free energy of disordered phases.

The first one of these methods was the thermodynamic integration method developed by Schmid and Schilling [4, 5]. This method allowed us to determine the free energy of each phase (with 30 respectively 29 rows) separately with very good precision, taking into account that these free energies were of the order of several thousands, while the free energy difference between the two phases was only of the order of ten. Yet even better suited for our purposes was the phase switch Monte Carlo method, which directly yields the free energy differences between two given phases. This led to a considerable reduction in the necessary CPU time in comparison with the thermodynamic intergration method and still yielded the exact location of the structural transition with much higher precision. We were also able to verify that the results of both methods are in very good agreement.

Due to the efficiency of the phase switch method it was possible to continue the investigation by increasing the misfit between the walls even further and inducing another structural transition, where the number of crystalline rows is again reduced by one and even more complex soliton patterns arise.

As the phase switch method requires the knowledge of a typical reference configuration of each phase prior to the simulation, we created several candidate structures and compared their free energies to the free energy of the structure with 29 rows. We were able to determine which one of these structures was actually the stable one and which ones were only metastable. We were also able to identify that two seemingly different soliton patterns quickly transformed into each other and thus had the same free energy. It would not have been possible to guess which structure was the stable one by knowledge of the internal energies of the configurations alone, as the entropy proved to play an important role here and one of the structures with the highest internal energies actually had the lowest free energy.

There are many more model systems in soft matter, such as block copolymer mesophases, where the free energy differences between different phases are only a very small fraction of the absolute free energy of the phases. Applying a thermodynamic integration method would not only yield results of low precision in these cases, but also require wasteful amounts of computational time. Hopefully, the phase switch method will be applied to such systems more often in the future.

An interesting project in this context would be the prediction of the stable structure of some –possibly crystalline– novel material. Finding stable structures experimentally can be especially difficult if there are several metastable structures which are close in their energies and thus only transform very slowly into the stable one. Yet it is essential for applications to know whether a structure is stable on long time scales, which can be determined by calculating the respective free energies of several candidate structures with the phase switch method as we have demonstrated here.

Another interesting phenomenon which we observed in the context of this particular structural transition is an ensemble inequivalence: in NVT simulations at fixed values of the system width a two-phase coexistence cannot be observed for this particular system as there will always be one phase (with a certain number of rows) which fits better into the given width. Due to this, there is a discontinuity of the pressure associated with the transition value of the misfit, where without a precursor in form of a two-phase region instantaneously the system transforms into the other phase. In the NPT ensemble, however, the phase transition will not show this particular feature as there will be a coexistence between two phases with different system widths at every value of the pressure close to the transition pressure just like in standard phase transitions in this ensemble. Thus, the two ensembles are not equivalent here.

As a next step we have studied the dynamics of the system, in particular the motion of the particles in this two-dimensional colloidal crystal under confinement. When computing the mean square displacement of the particles in the various rows for the case without any misfit, it becomes clear that the particles in the inner rows have a larger amplitude of movement as the confining effect of the rigid walls decreases with distance.

The structural transition, which occurs when the crystal is compressed, is visible in the motion of the particles as it enhances their mobility in those areas where the solitons are present. Thus, the rows containing the solitons exhibit the largest values of the mean square displacement now, while the inner rows show less movement and the rows directly adjacent to the walls remain almost immobile due to the walls' stabilizing structure. Another consequence of the incommensurability is that it decouples the inner part of the crystal from the walls, allowing a center-of-mass movement.

We also investigated the mean square displacement of the solitons itself. As solitons are no real particles, but rather areas of increased particle density, they are much more mobile than the particles themselves. This shows up in a mean square displacement which is in the x-direction an order of magnitude larger than that of the particles. In the y-direction the solitons are rather immobile as they repel each other and sitting close to the walls is their energetically most favourable option. The mean square displacements of the solitons exhibit an overshoot –similar to that of the crystalline

particles– due to their repulsive interaction with each other which leads to a harmonic potential felt by each individual soliton. This is in good agreement with previous investigations of the soliton-soliton-interactions by Chui et al. [3].

Another interesting aspect of the particle movements in the case with fully commensurate walls are the diffusion processes. We discovered that in addition to the well-known diffusion mechanism –in the course of which a pair of a hole and an interstitial particle is created due to thermal fluctuations, both the hole and the interstitial particle diffuse through the crystal and finally recombine– cooperative rotation processes occur. These have only been described in two previous publications by Montalenti et al. [24, 25] and were observed only very rarely in their simulations.

In our model system, however, these cooperative ring rotation processes outnumbered by far the events where hole and interstitial particles were created, at the chosen temperatures around $T = 1.0$, which is far away from the melting regime around $T_m = 1.35$. Especially rings consisting of three and of six particles were common, which can be explained with the hexagonal lattice structure. In spite of this, ring rotations did not contribute to the diffusion constant as much as the "normal" diffusion processes involving vacancies and interstitials, as the ring rotations occured much more often, but involved typically only a few (up to about 25) particles, while the "normal" diffusion events involved clusters with up to a few thousand particles, depending on how fast the hole and the interstitial recombined.

The simulations investigating the motion and diffusion of the particles were carried out using Langevin dynamics, where the solvent is modeled only via the friction and the random kicks that are applied to all particles and which are also conveniently thermostating the system. Of course, this is a very simplified approach and it would be highly desirable to repeat such studies in the future with more sophisticated simulation methods involving hydrodynamics and possibly explicit solvent molecules. Furthermore one should explicitly search for cooperative diffusion phenomena also in other model systems. As they contribute little to the overall diffusion constant, they might easily have been overlooked up to now. But especially at grain boundaries they might play an important role for the rearrangement of particles and thus for the precursors of nucleation processes.

In the last part of this thesis, we investigate the effect of shear on colloidal crystals, again using Langevin Dynamics. The shear is implemented by dragging the structured walls along the system. In order to avoid shear melting, we ran these simulations at temperatures $T = 0.3$ and $T = 0.5$ well below the melting temperature of $T_m = 1.35$.

We observed that when the walls are moved slowly along the crystal, the crystalline rows become slightly tilted. The outermost rows are dragged along with the walls, but the particles in the inner rows remain in their initial positions. If the shear

rate is increased, shear banding can be observed: The rows next to the walls still move along with them, while the inner part of the crystal breaks up into several –differently orientated– domains. At even higher shear rates, this effect vanishes again as the fast movement of the walls leads to an averaged-out wall potential which can no longer affect the crystal.

If the same simulations are carried out in a system where the walls are placed closer together, shearing significantly accelerates the transition from 30 crystalline rows to 29 rows and also the shear banding can be observed at lower shear rates than in the fully commensurate case. An interesting phenomenon occurs when the compressed crystal is sheared with very high velocities: As the walls are moving so fast that they practically interact with the mobile particles like planar walls, the structure of the rows directly adjacent to the walls is no longer stabilized by the walls and instead transforms in order to match the structure of the inner rows of the crystal. As these inner rows contain the extra particles which had to be distributed when one crystalline row disappeared in the course of the structural transition, these inner rows consist of more particles than the rows directly adjacent to the walls. Thus, holes are created in the rows next to the walls in order to make up for the "missing" particles. These holes can then freely diffuse further into the crystal.

As the moving walls continuously introduce motion and thus heat into the system, which the Langevin thermostat tries to cancel by applying friction and random kicks to the movement of the mobile particles, we obtained temperature profiles for the sheared colloidal crystals which clearly indicate that the temperature was higher close to the walls than in the inner parts of the crystal, especially at very high shear velocities. This shows that Langevin dynamics alone are not sufficient for thermostating this system.

It would therefore be highly desirable to introduce hydrodynamics (for example by using the DPD thermostat [63, 64] or the Lattice Boltzmann method in the version where colloidal particles are coupled to a flow field created by the solvent particles [65]) or to use an explicit solvent. Using explicit solvent could, for example, be feasible by implementing the multi-particle collision dynamics method of Kapral and Malevanets [152, 153]. This might dampen or enhance some of the effects we observed as the solvent would develop a Newtonian flow profile, which might smoothen the velocity profiles of the crystalline particles as well. Furthermore, explicit solvent is usually an excellent thermostat and would therefore provide an almost constant temperature profile throughout the system.

Another possibility for future improvements lies in the use of graphic cards. We used the program package hooMD-blue [13, 14] for the simulations with Langevin dynamics. This program is designed to run on graphic cards and as the processing

units of graphics cards can calculate the interactions of many thousand particles in parallel, their usage usually leads to a significant decrease in computational time. Unfortunately we discovered that the accuracy of consumer graphic cards which typically only provide single precision is not high enough for our crystalline system. We therefore had to carry out most of the simulations on CPUs. In the future, however, it should be possible to use either programmes which are designed to run on graphic cards and combine the memory of several processing units on graphic cards in order to obtain higher precision for their calculation (e.g. HALMD [15]), or to buy graphic cards which use full double precision. Such graphic cards are already available, but still rather expensive.

As both CPU and GPU time become more easily available each year, it should also soon be possible to rerun all of the simulations which we have presented here not only with higher precision, but also with more realistic interparticle potentials. It would, for example, be an improvement to the system if long ranged interactions were included and an r^{-3}-potential was used in order to make our simulations more directly comparable to actual experiments with magnetized polystyrene spheres.

Appendix A

Schmid-Schilling-Method, applied to the one-dimensional Ising Model

In order to test (and fully understand) the Schmid-Schilling thermodynamic integration method ([4, 5]) for the computation of absolute free energies, we used the one-dimensional Ising model as a first model system. Here, the free energy is known exactly from analytical calculations that can be found in standard text books. For a one-dimensional Ising stripe of length L with periodic boundary conditions applied to the ends, $J = 1$, $k_B = 1$ and with zero magnetical field, the Hamiltonian reads $H_0 = -J \sum_{i=1}^{N} s_i s_{i+1}$ with $s_{N+1} = s_1$. For zero magnetical field, the Transfer Matrix method yields a free energy of:

$$\begin{aligned} F &= -T \ln(\lambda_+^N + \lambda_-^N) \\ &= -T \ln \left[e^{\beta N} (1 + e^{-2\beta})^N + e^{\beta N} (1 - e^{-2\beta})^N \right] \\ &\approx N \left[-1 - T \ln(1 + e^{-2\beta}) \right] \end{aligned} \tag{A.1}$$

where λ_+ and λ_- denote the eigenvalues of the diagonalized transfer matrix, of which the smaller one can easily be neglected when taken to the power of N, for the range of values of N and T, which are of interest here.

In order to apply the method of calculating the absolute free energy by use of a reference system, one has to create a "representative" reference configuration by equilibrating the system at a given temperature and picking a typical configuration. These spin states of the reference configuration are denoted as s_i^R.

The Hamiltonian of this reference system is given by

$$H_{\text{ref}}(\lambda) = -\lambda \sum_{i=1}^{N} s_i s_i^R \tag{A.2}$$

(note that here λ is a measure for the strength of the interaction between the particles and their "potential wells" which attempt to ensure that the particles have the spin direction s_i^R; i.e. λ is not an eigenvalue here!) and its free energy can be computed easily via the partition function Z:

$$\begin{aligned} Z_{\text{ref}}(\lambda) &= \sum_{n=0}^{N} \binom{N}{n} e^{-\beta E(n)} \\ &= \sum_{n=0}^{N} \binom{N}{n} e^{-\beta(-\lambda)(n\times 1+(N-n)\times(-1))} \\ &= e^{-\beta\lambda N} \sum_{n=0}^{N} \binom{N}{n} e^{2\beta\lambda n} \\ &= e^{-\beta\lambda N}(1+e^{2\beta\lambda})^N \\ &= (e^{-\beta\lambda}+e^{\beta\lambda})^N \\ &= (2cosh(\beta\lambda))^N \end{aligned} \tag{A.3}$$

which leads to a free energy of:

$$F_{\text{ref}}(\lambda) = -T\ln(Z_{\text{ref}}) = -TN\ln(2cosh(\beta\lambda)) \tag{A.4}$$

In order to connect this reference system to the original system, one introduces the intermediate system with its Hamiltonian

$$H_{\text{intermed}}(\lambda) = H_0 + H_{\text{ref}}(\lambda). \tag{A.5}$$

The free energy difference between this intermediate system and the reference system (whose free energy we know from (A.4)) can be calculated at a fixed value of λ by "switching on and off" the interaction described by H_0.

Two different Monte Carlo steps are necessary here: In one step the free energy difference between this system interacting via the full Hamiltonian $H_{\text{intermed}}(\lambda)$ and the same particle configuration, but interacting only via the part $H_{\text{ref}}(\lambda)$ has to be computed. The decision to switch the full Hamiltonian on or off is then made using a Metropolis criterion considering the energy change $\Delta E = H_0(s_i)$, which depends on the current spin configuration s_i. The other step, which is carried out alternating with

the first one, is a sweep over all spins, deciding whether the spins are to be flipped or not, depending on the current Hamiltonian, which is either $H_{\text{intermed}}(\lambda)$ or $H_{\text{ref}}(\lambda)$.

Thus we computed the ratio $\frac{P_{\text{on}}}{P_{\text{off}}}$, where $P_{\text{on/off}}$ is the fraction of configurations where the Hamiltonian H_0 as a part of the whole Hamiltonian $H_{\text{intermed}}(\lambda)$ is switched on ("on"), respectively where only H_{ref} is used ("off"). As the free energy is defined by $F = -T\ln(Z)$, the free energy difference between the reference system of known free energy and the intermediate system is given by

$$\begin{aligned}\Delta F_2(\lambda) &= F_{\text{intermed}}(\lambda) - F_{\text{ref}}(\lambda) \\ &= -T\ln(Z_{\text{on}}) - (-T\ln(Z_{\text{off}})) \\ &= -T\ln\frac{Z_{\text{on}}}{Z_{\text{off}}} \\ &= -T\ln\frac{P_{\text{on}}}{P_{\text{off}}}\end{aligned} \tag{A.6}$$

On the other hand, $H_{\text{intermed}}(\lambda)$ reduces to H_0 at $\lambda = 0$. Therefore, we can calculate the free energy difference between the intermediate system and the original system by thermodynamic integration over λ'. So we had to compute

$$\langle\frac{\partial H_{\text{intermed}}(\lambda')}{\partial\lambda'}\rangle = -\langle\sum_{i=1}^{N} s_i s_i^R\rangle \tag{A.7}$$

(using (A.5) and (A.2)) for a range of λ' from zero up to the fixed value of λ that we used in the case of the reference system and the intermediate system. This quantity $-\langle\sum_{i=1}^{N} s_i s_i^R\rangle$ can of course easily be obtained by simulations in the case of the one-dimensional Ising model without any further moves being neccessary except simple spin flips, using the Hamiltonian $H_{\text{intermed}}(\lambda')$ with the current choice of λ' when computing the energy change for the metropolis criterion of the spin flips.

By integrating out, we obtained the free energy difference between the intermediate system at the fixed value of ϵ and the original system:

$$\Delta F_1(\lambda) = F_{\text{intermed}}(\lambda' = 0) - F_{\text{intermed}}(\lambda) = -\int_{\lambda}^{0} d\lambda' \langle\sum_{i=1}^{N} s_i s_i^R\rangle_{\lambda'} \tag{A.8}$$

In the end, these three values were simply added up:

$$F_{\text{original system}} = F_{\text{intermed}}(\lambda' = 0) = F_{\text{ref}}(\lambda) + \Delta F_2(\lambda) + \Delta F_1(\lambda) \tag{A.9}$$

T	λ	F_{analytic}	$F_{\text{simulation}}$
3.0	1.0	-224.3110	-224.3103
3.0	2.0	-224.3110	-224.3300
5.0	1.0	-356.5076	-356.5073
5.0	2.0	-356.5076	-356.5082

Table A.1: Schmid-Schilling thermodynamic integration method, applied to a one-dimensional Ising strip of length $L = 100$ with $\Delta\lambda' = 0.01$ for the integration; and comparison to the analytical result.

We tried this method for several values of λ and of the temperature T and compared them to the analytical result (see Table A.1). In the case of $\lambda = J$, the Hamiltonians of the original and the reference system were almost identical, so they produced the same value for F, and the simulation results for ΔF_1 and ΔF_2 cancelled each other almost perfectly as expected. But of course this is a very specific case and only due to the usage of the one-dimensional Ising model.

The values for $F_{\text{simulation}}$ were calculated by averaging over 5 simulation runs for each value of T and λ, which took less than one hour of CPU time on an ordinary workstation for each choice of T and λ. Obviously, our results are in very good agreement with the theoretical prediction of (A.1). One should note that using different reference configurations leads to different values for ΔF_1, but also to different values for ΔF_2, so that the overall value for F remains the same. Of course, this is only true if both reference configurations belong to the same phase.

Only at very low temperatures problems were encountered. They arose from the fact that the probability of turning the interaction between the spins off was very low, making it difficult to obtain an accurate value of ΔF_2. Thus, in this case it would have been necessary to switch the interactions gradually on and off in several steps as was done in the case of the colloid crystals.

Appendix B

Transition matrix method: The general case

The idea behind the transition matrix reweighting method is to register the acceptance probabilities of every attempted transition between two states in the so called transition matrix $\mathbf{T}$ and to compute the weight function from this transition matrix. As it might not be obvious how the exact weight function can be extracted from the transition matrix in the general case when no simplifications are possible or wanted, it will be explained in this part of the appendix.

Let's start out with a system comprised of N states, all of these states connected by possible transitions from each state to every other state. The current state of the system can then be described by a vector with N elements. If the simulation starts out in one known state of this system, this vector would be $\mathbf{v_s} = (1, 0, 0, ..., 0)$, for example. Letting the system evolve one step further would then mean to multiply the transition matrix, which contains the transition probabilities from each state to each other state, to the vector. This yields a new state vector $\mathbf{v_1} = \mathbf{T} \cdot \mathbf{v_s}$ giving the probabilities for finding the evolved system in each one of the states. In order to get to the equilibrium properties of the system, the transition matrix would need to be applied $n \to \infty$ times to the initial vector, thus making the system independent from the starting configuration. This would then yield the equilibrium state vector $\mathbf{v}_\infty = \mathbf{T^{n\to\infty}} \cdot \mathbf{v_s}$. This vector $\mathbf{v}_\infty$ contains the information about the probabilities of all states and is therefore needed in order to create the weight function.

In order to obtain this vector, it is useful to transform the transition matrix $\mathbf{T}$ into its diagonal form, thus containing its eigenvalues as elements:

$$\mathbf{T} = \mathbf{U^{-1}} \cdot diag(\lambda_1, \lambda_2, ..., \lambda_N) \cdot \mathbf{U} \tag{B.1}$$

which simplifies the exponentiating of $\mathbf{T}$ considerably:

$$\mathbf{T^n} = \mathbf{U^{-1}} \cdot diag(\lambda_1^n, \lambda_2^n, ..., \lambda_N^n) \cdot \mathbf{U} \tag{B.2}$$

as the matrices $\mathbf{U^{-1}}$ and $\mathbf{U}$ cancel each other.

Additionally, one can split $\mathbf{v_s}$ into a sum of eigenvectors of the transition matrix $\mathbf{T}$:

$$\mathbf{v_s} = \sum_i \mathbf{v_i} \tag{B.3}$$

For these eigenvectors the well-known relation $\mathbf{T v_i} = \lambda_i \mathbf{v_i}$ holds and therefore (using B.1) also $[\mathbf{U^{-1}} \cdot diag(\lambda_1, \lambda_2, ..., \lambda_N) \cdot \mathbf{U}]\mathbf{v_i} = \lambda_i \mathbf{v_i}$, which leads to the relation:

$$\mathbf{T^n v_s} = \sum_i \mathbf{T^n v_i} = \sum_i \lambda_i^n \mathbf{v_i} \approx \lambda_{max}^n \mathbf{v_{max}} \tag{B.4}$$

as n is a very large number and therefore the contribution of the largest eigenvalue exceeds everything else. This means, that the eigenvector $\mathbf{v_{max}}$ describes the probabilities of all states of the system in the equilibrated case. Therefore the general approach is to calculate the eigenvector to the largest eigenvalue of the transition matrix in order to extract the weight function, which will then simply be given by the normalized entries of this eigenvector as they correspond directly to the probabilities of the individual states.

Appendix C

Simulations of the crystalline system on graphic cards using HooMD-blue

Molecular dynamic simulations can easily be carried out on graphic cards by using standard program packages like “HooMD-blue”, “GROMACS” and many other options. Typically, these packages are very convenient as they only require a simple script specifying the temperature, time step, the form of the potential acting between certain particles and information about which groups of particles are to be integrated with which of the given algorithms.

The use of graphic cards leads to a significant speed-up of the calculations. This is mostly due to the fact that graphic cards are very suitable for the parallelization of the calculation of the interactions between the particles as it can calculate the interactions of many particles with their respective neighbours at the same time, while a CPU can only calculate the interaction of one particle with one of its neighbours at a time. For very small systems comprised of only 3672 particles which we studied in Ch. 2 and partly also in Ch. 3, this speed-up is not very large yet, but it increases for larger systems until the capacity of the graphic card is fully used and a further increase of the system size leads to a proportionally longer simulation time. So for example when shearing a system comprised of 73440 particles, thus moving the walls with constant velocity and integrating the inner particles via Langevin dynamics, a simulation of four mio. time steps needed roughly one hour of GPU time. As opposed to this, the same simulation run needed roughly 24 days of CPU-time (respectively 4 days on 6 CPUs) when carried out on CPUs with double precision.

There is a problem, however: most consumer graphic cards can only carry out calculations in single precision up to date (the double precision capabilities of these

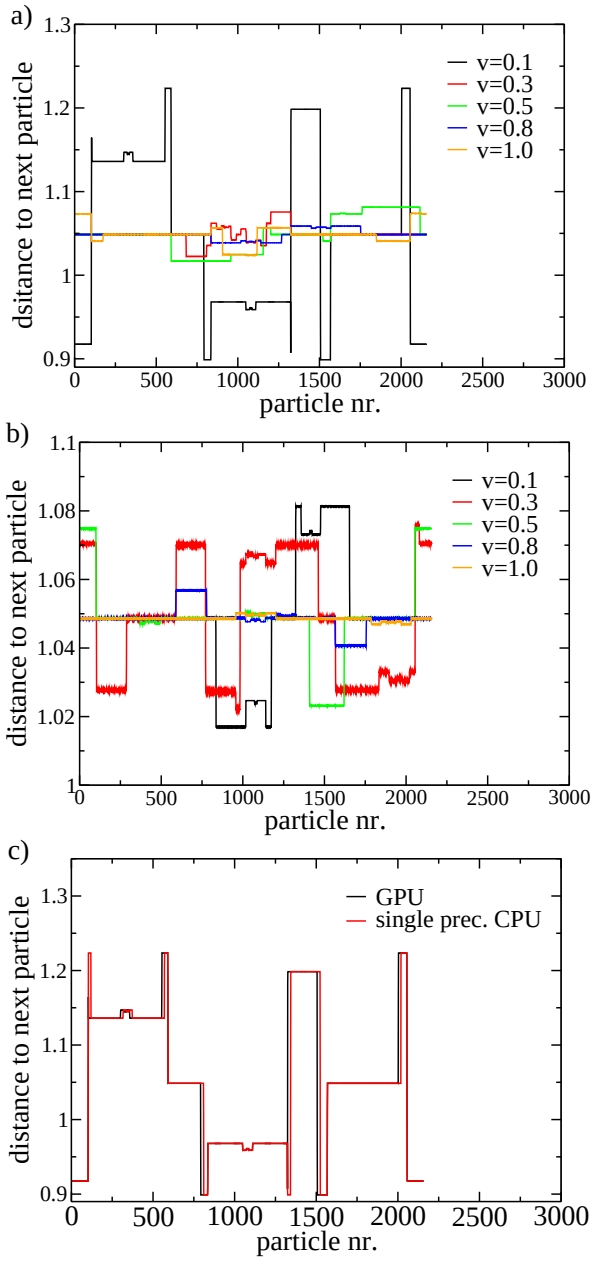

Figure C.1: Simulations of a system only consisting of 2160 wall particles, initially equidistantly distributed and moving at a constant velocity without interactions between the particles. a) Distances between the particles after 4 mio integration steps carried out on a GPU at a time step of $\Delta t = 0.002$ and different velocities of the particles. b) Same as uppermost, but with a time step of $\Delta t = 0.005$. c) Comparison between 4 mio integration steps carried out on a GPU at a time step of $\Delta t = 0.002$ and a particle velocity of $v = 0.1$ and the same simulation on a CPU using single precision.

cards are trimmed on purpose; professional graphic cards with full double precision capabilities are already available, albeit much more expensive). There are program packages like HALMD [15, 16] which utilize single precision graphic cards and use algorithms in order to build up memory units of almost double precision out of the single precision ones, but unfortunately these program packages do not provide the options yet which we needed for our simulations.

Single precision calculations proved to yield the same results as double precision ones when we ran simulations at not too low temperatures, but in order to avoid any risks, we only ran simulations at $T \geq 1.0$ on graphic cards and everything else on CPUs (and even most simulations at $T = 1.0$ were carried out on CPUs).

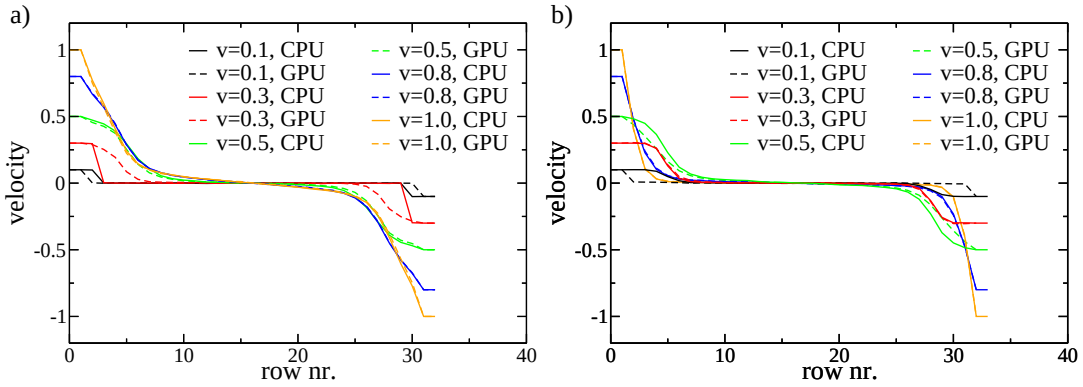

Figure C.2: Velocity profiles obtained from simulations on CPUs and GPUs. Each system was equilibrated for 3 mio. steps and each curve was averaged over 100 configurations. a) Results for the case of a misfit $\Delta = 2.2$ and a starting configuration with 29 rows. b) Results for the case without misfit and 30 rows. Shear velocities as indicated. In all cases, HooMD-blue with Langevin dynamics at a temperature $T = 0.3$ was used.

Still, we would like to illustrate here how significant the effect of low precision can be, especially for large systems which are integrated with small time steps and small velocities: If, for example, a row consisting of 2160 particles without any interactions is integrated with constant velocity and initially the same distance between all particles, one should think that these distances remain constant. This is not necessarily the case, however, as Fig. C.1 shows: As the system size in x-direction is quite large here, the coordinates range from about -1130 to $+1130$ in the x-direction, thus 4 digits are needed to code the value of the x-position in front of the decimal point. Thus only 3 of the 7 digits available in single precision are left for the part behind the decimal point. If now the time step is chosen as $\Delta t = 0.002$ and the velocity of these particles as $v = 0.1$, the particles would move a distance 0.0002 forward in x-direction per time step, which cannot be saved any more in the 3 digits available behind the decimal point.

This is not true for all particles, however, as only the particles at the ends of the stripe need 4 digits leading the decimal point to encode their position. Particles further inside of the stripe have more digits available and can be moved forward more accurately. But of course, as the particles move along the length of the system, sooner or later they all move through the area of low accuracy and the periodic boundary conditions. Thus, Fig. C.1 shows such a confusing pattern of distances between the particles.

Before we realized that the precision on GPUs is too low for running simulations containing walls which have to be integrated with constant velocity and also for running simulations of particles at low temperatures and thus with small velocities, we computed velocity profiles like the ones shown in Fig. C.2. Obviously, they are considerably different when rerun with double precision on CPUs. We therefore conclude that running simulations on graphic cards can be some orders of magnitude faster than on CPUs, but it should not be neglected that most graphic cards use only single precision, which is in some (maybe rare) cases not precise enough for the simulations that one wants to carry out.

List of Figures

List of Tables

Bibliography

[1] Y.H. Chui, S. Sengupta and K. Binder, Europhys. Lett. **83**, 58004 (2008)
SOLITON STAIRCASES AND STANDING STRAIN WAVES IN CONFINED COLLOIDAL CRYSTALS

[2] Y.H. Chui, S. Sengupta, I.K. Snook and K. Binder, J. Chem. Phys.**132**, 074701 (2010)
THE OBSERVATION OF FORMATION AND ANNIHILATION OF SOLITONS AND STANDING STRAIN WAVE SUPERSTRUCTURES IN TWO-DIMENSIONAL COLLOIDAL CRYSTAL

[3] Y.H. Chui, S. Sengupta, I.K. Snook and K. Binder, Phys. Rev. E **81**, 020403(R) (2010)
EFFECTIVE INTERACTIONS AND MELTING OF A ONE-DIMENSIONAL DEFECT LATTICE WITHIN A TWO-DIMENSIONAL CONFINED COLLOIDAL SOLID

[4] T. Schilling and F. Schmid, J. Chem. Phys. **131**, 231102 (2009)
COMPUTING ABSOLUTE FREE ENERGIES OF DISORDERED STRUCTURES BY MOLECULAR SIMULATION

[5] F. Schmid and T. Schilling, Physics Procedia **4**, 131 (2010)
A METHOD TO COMPUTE ABSOLUTE FREE ENERGIES OR ENTHALPIES OF FLUIDS

[6] A.D. Bruce, N.B. Wilding and G.J. Ackland, Phys. Rev. Lett. **79**, 3002 (1997)
FREE ENERGY OF CRYSTALLINE SOLIDS: A LATTICE-SWITCH MONTE CARLO METHOD

[7] N.B. Wilding and A.D. Bruce, Phys. Rev. Lett. **85**, 5138 (2000)
FREEZING BY MONTE CARLO PHASE SWITCH

[8] A.D. Bruce, A.N. Jackson, G.J. Ackland and N.B. Wilding, Phys. Rev. E **61**, 906 (2000)
LATTICE-SWITCH MONTE CARLO METHOD

[9] A.N. Jackson, A.D. Bruce and G.J. Ackland, Phys. Rev. E **65**, 036710 (2002)
LATTICE-SWITCH MONTE CARLO METHOD: APPLICATION TO SOFT POTENTIALS

[10] J.R. Errington, J. Chem. Phys. **120**, 3130 (2004)
SOLID-LIQUID PHASE COEXISTENCE OF THE LENNARD-JONES SYSTEM THROUGH PHASE-SWITCH MONTE CARLO SIMULATION

[11] G.C. McNeil-Watson and N.B. Wilding, J. Chem. Phys. **124**, 064504 (2006)
FREEZING LINE OF THE LENNARD-JONES FLUID: A PHASE SWITCH MONTE CARLO STUDY

[12] N.B. Wilding, J. Chem. Phys. **130**, 104103 (2009)
SOLID-LIQUID COEXISTENCE OF POLYDISPERSE FLUIDS VIA SIMULATION

[13] HOOMD-blue web page: *http://codeblue.umich.edu/hoomd-blue*

[14] J.A. Anderson, C.D. Lorenz and A. Travesset, *J. Comp. Phys.* **227**, 5342 (2008)
GENERAL PURPOSE MOLECULAR DYNAMICS SIMULATIONS FULLY IMPLEMENTED ON GRAPHICS PROCESSING UNITS

[15] HALMD web page: *http://halmd.org/index.html*

[16] P.H. Colberg and F. Höfling, Comp. Phys. Comm. **182**, 1120 (2011)
HIGHLY ACCELERATED SIMULATIONS OF GLASSY DYNAMICS USING GPUS: CAVEATS ON LIMITED FLOATING-POINT PRECISION

[17] C. Zener, Acta Cryst. **3**, 346 (1950)
RING DIFFUSION IN METALS

[18] A.S. Nowick, Annu. Rev. Mater. Sci. **26**, 1 (1996)
THE GOLDEN AGE OF CRYSTAL DEFECTS

[19] A.D. Smigelskasand E.O. Kirkendall, Trans. AIME **171**, 130 (1947)
ZINC DIFFUSION IN ALPHA BRASS

[20] G.E. Murch, p. 192 in:
PHASE TRANSFORMATIONS IN MATERIALS
Wiley VCH, Weinheim, 2001, Ed.: G. Kostorz

[21] D. Lazarus, p. XII (Foreword) in:
DIFFUSION IN CRYSTALLINE SOLIDS
Academic Press, Orlando (Florida), 1984, Eds.: G.E. Murch and A.S. Nowick

[22] W. Frank, U. Gösele and H. Mehrer, p. 66 in:
DIFFUSION IN CRYSTALLINE SOLIDS
Academic Press, Orlando (Florida), 1984, Eds.: G.E. Murch and A.S. Nowick

[23] F. Faupel and K. Rätzke, p. 267 in:
DIFFUSION IN CONDENSED MATTER
Springer, Berlin, 2005, Eds.: P. Heitjans and J. Kärger

[24] M.R. Sorensen, Y. Mishin and A.F. Voter, Phys. Rev. B **62**, 3658 (2000)
DIFFUSION MECHANISMS IN CU GRAIN BOUNDARIES

[25] F. Montalenti, A.F. Voter and R. Ferrando, Phys. Rev. B **66**, 205404 (2002)
SPONTANEOUS ATOMIC SHUFFLE IN FLAT TERRACES: AG(100)

[26] D. Wilms, P. Virnau, I.K. Snook and K. Binder, in preparation

[27] D. Wilms, N.B. Wilding and K. Binder, Phys. Rev. E **85**, 056703 (2012)
TRANSITIONS BETWEEN IMPERFECTLY ORDERED CRYSTALLINE STRUCTURES: A PHASE SWITCH MONTE CARLO STUDY

[28] D. Wilms, P. Virnau, S. Sengupta and K. Binder, Phys. Rev. E **85**, 061406 (2012)
LANGEVIN DYNAMICS SIMULATIONS OF A 2-DIMENSIONAL COLLOIDAL CRYSTAL UNDER CONFINEMENT AND SHEAR

[29] Q.H. Wei, C. Bechinger, D. Rudhardt, and P. Leiderer, Phys. Rev. Lett. **81**, 2606 (1998)
EXPERIMENTAL STUDY OF LASER-INDUCED MELTING IN TWO-DIMENSIONAL COLLOIDS

[30] N.A. Clark, B.J. Ackerson and A.J. Hurd, Phys. Rev. Lett. **50**, 1459 (1983)
MULITDETECTOR SCATTERING AS A PROBE OF LOCAL-STRUCTURE IN DISORDERED PHASES

[31] C. Bechinger, Q.W. Wei and P. Leiderer, J. Phys.: Condens. Matter **12**, A425 (2000)
REENTRANT MELTING OF TWO-DIMENSIONAL COLLOIDAL SYSTEMS

[32] C. Bechinger, M. Brunner and P. Leiderer, Phys. Rev. Lett. **86**, 930 (2001)
PHASE BEHAVIOR OF TWO-DIMENSIONAL COLLOIDAL SYSTEMS IN THE PRESENCE OF PERIODIC LIGHT FIELDS

[33] K. Zahn, R. Lenke and G. Maret, Phys. Rev. Lett. **82**, 2721 (1999)
TWO-STAGE MELTING OF PARAMAGNETIC COLLOIDAL CRYSTALS IN TWO DIMENSIONS

[34] K. Zahn and G. Maret, Phys. Rev. Lett. **85**, 3656 (2000)
DYNAMIC CRITERIA FOR MELTING IN TWO DIMENSIONS

[35] C. Eisenmann, P. Keim, U. Gasser and G. Maret, J. Phys.: Condens. Matter **16**, S4095 (2004)
MELTING OF ANISOTROPIC COLLOIDAL CRYSTALS IN TWO DIMENSIONS

[36] K. Zahn, A. Wille, G. Maret, S. Sengupta and P. Nielaba, Phys. Rev. Lett. **90**, 155506 (2003)
ELASTIC PROPERTIES OF 2D COLLOIDAL CRYSTALS FROM VIDEO MICROSCOPY

[37] L. Assoud, F. Ebert, P. Keim, R. Messina, G. Maret and H. Löwen, J. Phys.: Condens. Matter **21**, 464114 (2009)
CRYSTAL NUCLEI AND STRUCTURAL CORRELATIONS IN TWO-DIMENSIONAL COLLOIDAL MIXTURES: EXPERIMENT VERSUS SIMULATION

[38] S. Medina
DIPLOMARBEIT
Johannes-Gutenberg-Universität Mainz (2010)

[39] S. Medina, P. Virnau and K. Binder, J. Phys.: Condensed Matter **23**, 035105 (2011)
CONFINED BINARY TWO-DIMENSIONAL COLLOIDAL CRYSTALS: MONTE CARLO SIMULATION OF CRACK FORMATION

[40] D. Wilms, S. Deutschlaender, U. Siems, K. Franzrahe, P. Henseler, P. Keim, N. Schwierz, P. Virnau, K. Binder, G. Maret and P. Nielaba, J. Phys.: Condens. Matter (accepted, 2012)
EFFECTS OF CONFINEMENT AND EXTERNAL FIELDS ON STRUCTURE AND TRANSPORT IN COLLOIDAL DISPERSIONS IN REDUCED DIMENSIONALITY

[41] K. Zahn, J.M. Mendez-Alcaraz, and G. Maret, Phys. Rev. Lett. **79**, 175 (1997)
HYDRODYNAMIC INTERACTIONS MAY ENHANCE THE SELF-DIFFUSION OF COLLOIDAL PARTICLES

[42] H. König, R. Hund, K. Zahn and G. Maret, Eur. Phys. J.E**18**, 287 (2005)
EXPERIMENTAL REALIZATION OF A MODEL GLASS FORMER IN 2D

[43] M. Koppl, P. Henseler, A. Erbe, P. Nielaba and P. Leiderer, Phys. Rev. Lett. **97**, 208302 (2006)
LAYER REDUCTION IN DRIVEN 2D-COLLOIDAL SYSTEMS THROUGH MICROCHANNELS

[44] F. Ebert, P. Dillmann, G. Maret and P. Keim, Rev. Sci. Instr. **80**, 083902 (2009)
THE EXPERIMENTAL REALIZATION OF A TWO-DIMENSIONAL COLLOIDAL MODEL SYSTEM

[45] F. Ebert, G. Maret and P. Keim, Eur. Phys. J. E **29**, 311 (2009)
PARTIAL CLUSTERING PREVENTS GLOBAL CRYSTALLIZATION IN A BINARY 2D COLLOIDAL GLASS FORMER

[46] P. Henseler, A. Erbe, M. Koppl, P. Leiderer and P. Nielaba, Phys. Rev. E**81**, 041402 (2010)
DENSITY REDUCTION AND DIFFUSION IN DRIVEN TWO-DIMENSIONAL COLLOIDAL SYSTEMS THROUGH MICROCHANNELS

[47] H. Löwen *J. Phys.: Condens. Matter* **13** R415 (2001)
COLLOIDAL SOFT MATTER UNDER EXTERNAL CONTROL

[48] C. Likos *Phys. Rep.* **348** 267 (2001)
EFFECTIVE INTERACTIONS IN SOFT CONDENSED MATTER PHYSICS

[49] A. Chowdhury, B.J. Ackerson and N.A. Clark, Phys. Rev. Lett. **55**, 833 (1985)
LASER-INDUCED FREEZING

[50] W.G. Hoover, M. Ross, K.W. Johnson, D. Henderso, J.A. Barker and B.C. Brown, J. Chem. Phys. **52**, 4931 (1970)
SOFT-SPHERE EQUATION OF STATE

[51] K. Bagchi, H.C. Andersen, and W. Swope, Phys. Rev. E **53**, 3794 (1996)
OBSERVATION OF A TWO-STAGE MELTING TRANSITION IN TWO DIMENSIONS

[52] H.N.W. Lekkerkerker, p. 53 in:
OBSERVATION, PREDICTION AND SIMULATION OF PHASE TRANSITIONS IN COMPLEX FLUIDS
Kluwer, Dordrecht, 1995, Ed.: M. Baus

[53] D.R. Squire, A.C. Holt and W.G. Hoover, Physica **42**, 388 (1969)
ISOTHERMAL ELASTIC CONSTANTS FOR ARGON. THEORY AND MONTE CARLO CALCULATIONS

[54] D.P. Landau and K. Binder, Cambridge Univ. Press, Cambridge, 2009, 3rd ed.
A GUIDE TO MONTE CARLO SIMULATIONS IN STATISTICAL PHYSICS

[55] J. Hansen and I.R. McDonald, Academic Press, San Diego, 2000
THEORY OF SIMPLE LIQUIDS

[56] J. Villain, p. 222 in:
ORDERING IN STRONGLY FLUCTUATING CONDENSED MATTER SYSTEMS
Plenum, New York, 1980, Ed.: T. Riste

[57] M. Braun and Y.S. Kivshar, Springer, Berlin, 2004
THE FRENKEL-KONTOROVA MODEL: CONCEPTS, METHODS, AND APPLICATIONS

[58] D. Frenkel and B. Smit, Academic, San Diego, 2002
UNDERSTANDING MOLECULAR SIMULATION: FROM ALGORITHMS TO APPLICATIONS

[59] L. Verlet, Phys. Rev. **159**, 98 (1967)
COMPUTER "EXPERIMENTS" ON CLASSICAL FLUIDS. I. THERMODYNAMICAL PROPERTIES OF LENNARD-JONES MOLECULES

[60] M.P. Allen and D.J. Tildesley, Oxford University Press, reprint (1989)
COMPUTER SIMULATION OF LIQUIDS

[61] D.J. Evans and G.P. Morriss, Cambridge University Press, 2nd edition (2008)
STATISTICAL MECHANICS OF NONEQUILIBRIUM LIQUIDS

[62] I.K. Snook, Elsevier, Amsterdam (2007)
THE LANGEVIN AND GENERALIZED LANGEVIN APPROACH TO THE DYNAMICS OF ATOMIC, POLYMERIC AND COLLOIDAL SYSTEMS

[63] T. Soddemann, B. Dünweg and K. Kremer, Phys. Rev. E **68**, 046702 (2003)
DISSIPATIVE PARTICLE DYNAMICS: A USEFUL THERMOSTAT FOR EQUILIBRIUM AND NONEQUILIBRIUM MOLECULAR DYNAMICS SIMULATIONS

[64] R.D. Groot and P.B. Warren, J. Chem. Phys. **107**, 4423 (1997)
DISSIPATIVE PARTICLE DYNAMICS: BRIDGING THE GAP BETWEEN ATOMISTIC AND MESOSCOPIC SIMULATION

[65] B. Dünweg and A.J.C. Ladd, p.89 in:
ADVANCES IN POLYMER SCIENCE
Springer, Berlin, 2009, Eds.: C. Holm and K. Kremer

[66] M. Metropolis, A.W. Rosenbluth, M.N. Rosenbluth, A.H. Teller and E. teller, J. Chem. Phys. **21**, 1087 (1953)
EQUATION OF STATE CALCULATIONS BY FAST COMPUTING MACHINES

[67] B.A. Berg and T. Neuhaus, Phys. Rev. Lett. **68**, 9 (1992)
MULTICANONICAL ENSEMBLE - A NEW APPROACH TO SIMULATE 1ST-ORDER PHASE-TRANSITIONS

and: B.A. Berg, Int. J. Mod. Phys. C. **4**, 249 (1993)
MULTICACONICAL MONTE-CARLO SIMULATIONS

[68] N.B. Wilding, Phys. Rev. E **52**, 602 (1995)
CRITICAL-POINT AND COEXISTENCE-CURVE PROPERTIES OF THE LENNARD-JONES FLUID – A FINITE-SIZE-SCALING STUDY

[69] F.G. Wang and D.P. Landau, Phys. Rev. Lett. **86**, 2050 (2001)
EFFICIENT, MULTIPLE-RANGE RANDOM WALK ALGORITHM TO CALCULATE THE DENSITY OF STATES

[70] P. Virnau and M. Müller, J. Chem. Phys. **120**, 10925 (2004)
CALCULATION OF FREE ENERGY THROUGH SUCCESSIVE UMBRELLA SAMPLING

[71] G. Decker and J.B. Schlenoff (eds.), Wiley-VCH, Weinheim, 2002
MULTILAYER THIN FILMS: SEQUENTIAL ASSEMBLY OF NANOCOMPOSITE MATERIALS

[72] E.L. Wolf, Wiley-VCH, Weinheim, 2002
NANOPHYSICS AD NANOTECHNOLOGY

[73] Y. Champion and H.J. Fecht (eds.), Wiley-VCH, Weinheim, 2004
NANO-ARCHITECTURED AND NANO-STRUCTURED MATERIALS

[74] C.N.R. Rao, A. Müller, and A.K. Cheetham (eds.), Wiley-VCH, Weinheim, 2004
THE CHEMISTRY OF NANOMATERIALS

[75] R. Kelsall, I.W. Hamley, and M. Geoghegan (eds.), Wiley-VCH, Weinheim, 2005
NANOSCALE SCIENCE AND TECHNOLOGY

[76] C. Chipot and A. Pohorille (eds.), Springer, Berlin, 2007
FREE ENERGY CALCULATIONS. THEORY AND APPLICATIONS IN CHEMISTRY AND BIOLOGY

[77] A.D. Bruce and N.B. Wilding, Adv. Chem. Phys. **127**, 1 (2003)
COMPUTATIONAL STRATEGIES FOR MAPPING EQUILIBRIUM PHASE DIAGRAMS

[78] N.B. Wilding, p. 39 in:
COMPUTER SIMULATIONS IN CONDENSED MATTER: FROM MATERIALS TO CHEMICAL BIOLOGY, VOL. 1
Springer, Berlin, 2006, Eds.: M. Ferrario, G. Ciccotti, and K. Binder

[79] M. Müller and J.J. de Pablo, p. 67 in:
COMPUTER SIMULATIONS IN CONDENSED MATTER: FROM MATERIALS TO CHEMICAL BIOLOGY, VOL. 1
Springer, Berlin, 2006, Eds.: M. Ferrario, G. Ciccotti, and K. Binder

[80] J.G. Kirkwood, J. Chem. Phys. **3**, 300 (1935)
STATISTICAL MECHANICS OF FLUID MIXTURES

[81] K. Binder, Z. Phys. B**45**, 61 (1981)
MONTE-CARLO STUDY OF ENTROPY FOR FACE-CENTERED CUBIC ISING ANTIFERROMAGNETS

[82] D. Frenkel and A.J.C. Ladd, J. Chem. Phys. **81**, 3188 (1984)
NEW MONTE-CARLO METHOD TO COMPUTE THE FREE-ENERGY OF ARBITRARY SOLIDS - APPLICATION TO THE FCC AND HCP PHASES OF HARD-SPHERES

[83] A. Ricci, P. Nielaba, S. Sengupta, and K. Binder, Phys. Rev. E **75**, 011405 (2007)
ORDERING OF TWO-DIMENSIONAL CRYSTALS CONFINED IN STRIPS OF FINITE WIDTH

[84] K. Binder, Y.-H. Chui, P. Nielaba, A. Ricci, and S. Sengupta, p.1 in:
NANOPHENOMENA AT SURFACES: FUNDAMENTALS OF EXOTIC CONDENSED MATTER PROPERTIES
Springer, Berlin, 2011, Ed.: M. Michailov

[85] Y.-J. Lai and L. I, Phys. Rev. E**64**, 015601(R) (2001)
DEFECTS AND PARTICLE MOTIONS IN THE NONUNIFORM MELTING OF A TWO-DIMENSIONAL COULOMB CLUSTER

[86] L.W. Teng, P.S. Tu and L. I, Phys. Rev. Lett. **90**, 245004 (2003)
MICROSCOPIC OBSERVATION OF CONFINEMENT-INDUCED LAYERING AND SLOW DYNAMICS OF DUSTY-PLASMA LIQUIDS IN NARROW CHANNELS

[87] R.A. Segalman, A. Hexemer and E.J. Kramer, Phys. Rev. Lett. **91**, 196101 (2003)
EDGE EFFECTS ON THE ORDER AND FREEZING OF A 2D ARRAY OF BLOCK COPOLYMER SPHERES

[88] N. Kokubo, R. Besseling and P.H. Kes, Phys. Rev. B **69**, 064504 (2004)
DYNAMIC ORDERING AND FRUSTRATION OF CONFINED VORTEX ROWS STUDIED BY MODE-LOCKING EXPERIMENTS

[89] G. Piacente, I.V. Schweigert, J.J. Betouras and F.M. Peeters, Phys. Rev. B **69**, 045324 (2004)
GENERIC PROPERTIES OF A QUASI-ONE-DIMENSIONAL CLASSICAL WIGNER CRYSTAL

[90] D. Chaudhuri and S. Sengupta, Phys. Rev. Lett. **93**, 115702 (2004)
CONSTRAINED DEFORMATION OF A CONFINED SOLID: ANOMALOUS FAILURE BY NUCLEATION OF SMECTIC BANDS

[91] R. Haghgooie and P.S. Doyle, Phys. Rev. E **70**, 061408 (2004)
STRUCTURAL ANALYSIS OF A DIPOLE SYSTEM IN TWO-DIMENSIONAL CHANNELS

[92] L.G. MacDowell, V.K. Shen and J.R. Errington, J. Chem. Phys. **125**, 034705 (2006)
NUCLEATION AND CAVITATION OF SPHERICAL, CYLINDRICAL, AND SLAB-LIKE DROPLETS AND BUBBLES IN SMALL SYSTEMS
and: L.G. MacDowell, P. Virnau, M. Müller and K. Binder, J. Chem. Phys. **120**, 5293 (2004)
THE EVAPORATION/CONDENSATION TRANSITION OF LIQUID DROPLETS

[93] D. Deb, A. Winkler, P. Virnau and K. Binder, J. Chem. Phys. **136**, 134710 (2012)
SIMULATION OF FLUID-SOLID COEXISTENCE IN FINITE VOLUMES: A METHOD TO STUDY THE PROPERTIES OF WALL-ATTACHED CRYSTALLINE NUCLEI

[94] G.R. Smith and A.D. Bruce, J. Phys. A **28**, 6623 (1995)
A STUDY OF THE MULTI-CANONICAL MONTE CARLO METHOD

[95] J.S. Wang, T.K. Tay and R.H. Swendsen, Phys. Rev. Lett. **82**, 476 (1999)
TRANSITION MATRIX MONTE CARLO REWEIGHTING AND DYNAMICS

[96] J.S. Wang and R.H. Swendsen, J. Stat. Phys. **106**, 245 (2002)
TRANSITION MATRIX MONTE CARLO METHOD

[97] R.J. Speedy, Mol. Phys. **80**, 1105 (1993)
THE ENTROPY OF A GLASS

[98] D. Deb, D. Wilms, A. Winkler, P. Virnau and K. Binder, Int. J. Mod. Phys. C. (2012, in press)
METHODS TO COMPUTE PRESSURE AND WALL TENSION IN FLUIDS CONTAINING HARD PARTICLES

[99] A. Milchev, V. Yamakov and K. Binder, Phys. Chem. Chem. Phys. **1**, 2083 (1999)
ESCAPE TRANSITION OF A POLYMER CHAIN: PHENOMENOLOGICAL THEORY AND MONTE CARLO SIMULATIONS

[100] A. Milchev, V. Yamakov and K. Binder, Europhys. Lett. **47**, 675 (1999)
ESCAPE TRANSITION OF A COMPRESSED POLYMER MUSHROOM UNDER GOOD SOLVENT CONDITIONS

[101] A.M. Skvortsov, L.I. Klushin and F.A.M. Leermakers, Europhys. Lett. **58**, 292 (2002)
EXACTLY SOLVED POLYMER MODELS WITH CONFORMATIONAL ESCAPE TRANSITIONS OF A COIL-TO-FLOWER TYPE

[102] L.I. Klushin, A.M. Skvortsov and F.A.M. Leermakers, Phys. Rev. E**69**, 061101 (2004)
PARTITION FUNCTION, METASTABILITY, AND KINETICS OF THE ESCAPE TRANSITION FOR AN IDEAL CHAIN

[103] A.M. Skvortsov, L.I. Klushin and F.A.M. Leermakers, J. Chem. Phys. **126**, 024905 (2007)
NEGATIVE COMPRESSIBILITY AND NONEQUIVALENCE OF TWO STATISTICAL ENSEMBLES IN THE ESCAPE TRANSITION OF A POLYMER CHAIN

[104] D.I. Dimitrov, L.I. Klushin A.M. Skvortsov, A. Milchev and K. Binder, Eur. Phys. J. E**29**, 9 (2009)
THE ESCAPE TRANSITION OF A POLYMER: A UNIQUE CASE OF NONEQUIVALENCE BETWEEN STATISTICAL ENSEMBLES

[105] L.I. Klushin and A.M. Skvortsov, J. Phys. A: Math. Theor. **44**, 473001 (2011)
UNCONVENTIONAL PHASE TRANSITIONS IN A CONSTRAINED SINGLE POLYMER CHAIN

[106] M. Kikuchi and K. Binder, Europhys. Lett. **21**, 427 (1993)
MONTE-CARLO STUDY OF THIN-FILMS OF THE SYMMETRICAL DIBLOCK-COPOLYMER MELT

[107] D.G. Walton, G.J. Kellogg, A.M. Mayes, P. Lambooy and T.P. Russell, Macromolecules **27**, 6225 (1994)
A FREE-ENERGY MODEL FOR CONFINED DIBLOCK COPOLYMERS

[108] P. Lambooy, T.P. Russell, G.J. Kellogg A.M. Mayes, P.D. Gallagher, and S.K. Satija, Phys. Rev. Lett. **72**, 2899 (1994)
OBSERVED FRUSTRATION IN CONFINED BLOCK-COPOLYMERS

[109] K. Binder, Adv. Polym. Sci. **138**, 1 (1999)
PHASE TRANSITIONS OF POLYMER BLENDS AND BLOCK COPOLYMER MELTS IN THIN FILMS

[110] D. Ausserre, V.A. Raghunathan and M. Maaloum, J. Phys. II (France) **3**, 1485 (1993)
STATIC WETTING BEHAVIOUR OF DIBLOCK COPOLYMERS

[111] D. Deb, D. Wilms, A. Winkler, P. Virnau and K. Binder, Int. J. Mod. Phys.: Conference Series, accepted (2012)
METHODS TO COMPUTE PRESSURE AND WALL TENSION IN FLUIDS CONTAINING HARD PARTICLES

[112] D. Deb, D. Wilms, A. Winkler, P. Virnau and K. Binder in:
NIC PROCEEDINGS 2012
MONTE CARLO SIMULATION STUDIES OF INTERFACIAL FREE ENERGIES IN COLLOIDAL SUSPENSIONS
Jülich, Forschungszentrum Jülich 2012

[113] W.C. Poon and P.N. Pusey, p. 3 in:
OBSERVATION, PREDICTION AND SIMULATION OF PHASE TRANSITIONS IN COMPLEX FLUIDS
Kluwer, Dordrecht, 1995, Ed: M. Baus

[114] T. Palberg, *Curr. Opin. Colloid Interface Sci.* **2**, 607 (1997)
COLLOIDAL CRYSTALLIZATION DYNAMICS

[115] H. Löwen, *J. Phys.: Condens. Matter* **13**, R415 (2001)
COLLOIDAL SOFT MATTER UNDER EXTERNAL CONTROL

[116] Eds.: H. Löwen and C.N. Likos
COLLOIDAL DISPERSIONS IN EXTERNAL FIELDS
Special Issue of *J. Phys.: Condens. Matter* **16**, No. 38 (2004)

[117] K. Franzrahe, P. Nielaba, A. Ricci, K. Binder, S. Sengupta, P. Keim and G. Maret *J. Phys.: Condens. Matter* **20** 404218 (2008)
FIELD-INDUCED ORDERING PHENOMENA AND NON-LOCAL ELASTIC COMPLIANCE IN TWO-DIMENSIONAL COLLOIDAL CRYSTALS

[118] T. Bohlein, J. Mikhael and C. Bechinger *Nature Mat.* **11** 126 (2012)
OBSERVATION OF KINKS AND ANTIKINKS IN COLLOIDAL MONOLAYERS DRIVEN ACROSS ORDERED SURFACES

[119] D.M. Herlach, I. Klassen, P. Wette and D. Holland-Moritz, *J. Phys.: Condens. Matter* **22**, 153101 (2010)
COLLOIDS AS MODEL SYSTEMS FOR METALS AND ALLOYS: A CASE STUDY OF CRYSTALLIZATION

[120] J.J. Crassous, M. Siebenbürger, M. Ballauff, M. Drechsler, D. Hajnal, O. Henrich and M. Fuchs, *J. Chem. Phys.* **128**, 204902 (2008)
SHEAR STRESSES OF COLLOIDAL DISPERSIONS AT THE GLASS TRANSITION IN EQUILIBRIUM AND IN FLOW

[121] R. Haghgooie and P.S. Doyle, *Phys. Rev. E* **72**, 011405 (2005)
STRUCTURE AND DYNAMICS OF REPULSIVE MAGNETORHEOLOGICAL COLLOIDS IN TWO-DIMENSIONAL CHANNELS

[122] P.M. Chaikin and T.C. Lubensky, Cambridge Univ. Press, Cambridge, 1995
PRINCIPLES OF CONDENSED MATTER PHYSICS

[123] M.L. Grant, B.S. Swartzentruber, N.C. Bartelt and J.B. Hannon, Phys. Rev. Lett **86**, 4588 (2001)
DIFFUSION KINETICS IN THE PD/CU(001) SURFACE ALLOY

[124] R. van Gastel, E. Somfai, S.B. van Albada, W. van Saarloos and J.W.M. Frenken, Phys. Rev. Lett. **86**, 1562 (2001)
NOTHING MOVES A SURFACE: VACANCY MEDIATED SURFACE DIFFUSION

[125] P.J. Feibelman, Phys. Rev. Lett. **65**, 729 (1990)
DIFFUSION PATH FOR AN AL ADATOM ON AL(001)

[126] Z.-P. Shi, Z. Zhang, A.K. Swan and J.F. Wendelken, Phys. Rev. Lett. **76**, 4927 (1996)
DIMER SHEARING AS A NOVEL MECHANISM FOR CLUSTER DIFFUSION AND DISSOCIATION ON METAL (100) SURFACES

[127] T.R. Linderoth, S. Horch, L. Petersen, S. Helveg, E. Laegsgaard, I. Stensgaard and F. Besenbacher, Phys. Rev. Lett. **82**, 1494 (1999)
NOVEL MECHANISM FOR DIFFUSION OF ONE-DIMENSIONAL CLUSTERS: PT/PT(110)-(1×2)

[128] F. Montalenti and R. Ferrando, Phys. Rev. Lett. **82**, 1498 (1999)
LEAPFROG DIFFUSION MECHANISM FOR ONE-DIMENSIONAL CHAINS ON MISSING-ROW RECONSTRUCTED SURFACES

[129] J.M. Cohen, Surface Science Letters **306**, L545 (1994)
LONG RANGE ADATOM DIFFUSION MECHANISM ON FCC (100) EAM MODELED MATERIALS

[130] T. Ala-Nissila, R. Ferrando and S.C. Ying, Advances in Physics **51**, 949 (2002)
COLLECTIVE AND SINGLE PARTICLE DIFFUSION ON SURFACES

[131] K. F. McCarty, J.A. Nobel and N.C. Bartelt, Nature **412**, 622 (2001)
VACANCIES IN SOLIDS AND THE STABILITY OF SURFACE MORPHOLOGY

[132] M.R. Sorensen and A.F. Voter, J. Chem. Phys. **112**, 9599 (2000)
TEMPERATURE-ACCELERATED DYNAMICS FOR SIMULATION OF INFREQUENT EVENTS

[133] F. Montalenti and A.F. Voter, J. Chem. Phys. **116**, 4819 (2002)
EXPLOITING PAST VISITS OR MINIMUM-BARRIER KNOWLEDGE TO GAIN FURTHER BOOST IN THE TEMPERATURE-ACCELERATED DYNAMICS METHOD

[134] D.R. Nelson, p.1 in:
PHASE TRANSITIONS AND CRITICAL PHENOMENA, VOL. 7
Academic, London, 1983, Eds.: C. Domb and J.L. Lebowitz

[135] Y.L. Wu, D. Derks, A. van Blaaderen and A. Imhof *Proc. Nat. Acad. Sci.* **106** 10564 (2009)
MELTING AND CRYSTALLIZATION OF COLLOIDAL HARD-SPHERE SUSPENSIONS UNDER SHEAR

[136] M. Stieger, P. Lindner and W. Richtering *J. Phys.: Condens. Matter* **16** S3861 (2004)
STRUCTURE FORMATION IN THERMORESPONSIVE MICROGEL SUSPENSIONS UNDER SHEAR FLOW

[137] R. Blaak, S. Auer, D. Frenkel and H. Löwen *J. Phys.: Condens. Matter* **16** S3873 (2004)
HOMOGENEOUS NUCLEATION OF COLLOIDAL MELTS UNDER THE INFLUENCE OF SHEARING FIELDS

[138] R. Blaak, S. Auer, D. Frenkel and H. Löwen *Phys. Rev. Lett.* **93** 068303 (2004)
CRYSTAL NUCLEATION OF COLLOIDAL SUSPENSIONS UNDER SHEAR

[139] A. Stipp, R. Biehl, T. Preis, J.N. Liu, A.B. Fontecha, H.J. Schöpe and T. Palberg *J. Phys.: Condens. Matter* **16** S3885 (2004)
HETEROGENEOUS NUCLEATION OF COLLOIDAL MELTS UNDER THE INFLUENCE OF SHEARING FIELDS

[140] M. Stieger, P. Lindner and W. Richtering *e-Polymers* 046 (2004)
SMALL-ANGLE NEUTRON SCATTERING STUDY OF SHEAR-INDUCED PHASE SEPARATION IN AQUEOUS POLY(N-ISOPROPYLACRYLAMIDE) SOLUTIONS

[141] G. Petekidis, D. Vlassopoulos and P.N. Pusey *J. Phys.: Condens. Matter* **16** S3955 (2004)
YIELDING AND FLOW OF SHEARED COLLOIDAL GLASSES

[142] H. Löwen and C.N. Likos (eds.) *J. Phys.: Condens. Matter* **16** Special Issue (2004)
COLLOIDAL DISPERSIONS IN EXTERNAL FIELDS, BONN-BAD GODESBERG (29 MARCH TO 1 APRIL 2004)

[143] A. Ricci, P. Nielaba, S. Sengupta and K. Binder *Phys. Rev. E* **74** 010404(R) (2006)
LACK OF LONG-RANGE ORDER IN CONFINED TWO-DIMENSIONAL MODEL COLLOIDAL CRYSTALS

[144] D. Chaudhuri and S. Sengupta *J. Chem. Phys.* **128** 194702 (2008)
ANOMALOUS STRUCTURAL AND MECHANICAL PROPERTIES OF SOLIDS CONFINED IN QUASI-ONE-DIMENSIONAL STRIPS

[145] Y. Han, Y. Shokef, A.M. Alsayed, P. Yunker, T.C. Lubensky and A.G. Yodh *Nature* **456** 898 (2008)
GEOMETRIC FRUSTRATION IN BUCKLED COLLOIDAL MONOLAYERS

[146] C.N. Likos and C.L. Henley *Phil. Mag. B* **68** 85 (1993)
COMPLEX ALLOY PHASES FOR BINARY HARD-DISK MIXTURES

[147] L. Assoud, R. Messina and H. Löwen *EPL* **80** 48001 (2007)
STABLE CRYSTALLINE LATTICES IN TWO-DIMENSIONAL BINARY MIXTURES OF DIPOLAR PARTICLES

[148] F. Ebert, P. Keim and G. Maret *Eur. Phys. J. E* **26** 161 (2008)
LOCAL CRYSTALLINE ORDER IN A 2D COLLOIDAL GLASS FORMER

[149] P. Nielaba, K. Binder, D. Chaudhuri, K. Franzrahe, P. Henseler, M. Lohrer, A. Ricci, S. Sengupta and W. Strepp *J. Phys.: Condens. Matter* **16** S4115 (2004)
ELASTIC PROPERTIES, STRUCTURES AND PHASE TRANSITIONS IN MODEL COLLOIDS

[150] K. Franzrahe and P. Nielaba *Phys. Rev. E* **76** 061503 (2007)
ENTROPY VERSUS ENERGY: THE PHASE BEHAVIOR OF A HARD-DISK MIXTURE IN A PERIODIC EXTERNAL POTENTIAL

[151] A. Imperio and L. Reatto *J. Phys.: Condens. Matter* **16** S3769 (2004)
A BIDIMENSIONAL FLUID SYSTEM WITH COMPETING INTERACTIONS: SPONTANEOUS AND INDUCED PATTERN FORMATION

[152] A. Malevanets and R. Kapral R, J. Chem. Phys **112**, 7260 (2000)
SOLUTE MOLECULAR DYNAMICS IN A MESOSCALE SOLVENT

[153] M. Ripoll, K. Mussawisade, R.G. Winkler and G. Gompper, Phys. Rev. E **72**, 016701 (2005)
DYNAMIC REGIMES OF FLUIDS SIMULATED BY MULTIPARTICLE-COLLISION DYNAMICS

[154] R. Khare, J. dePablo and A. Yethiraj *J. Chem. Phys.* **107** 2589 (1997)
MOLECULAR SIMULATION AND CONTINUUM MECHANICS STUDY OF SIMPLE FLUIDS IN NON-ISOTHERMAL PLANAR COUETTE FLOWS

[155] C. Pastorino, K. Binder and M. Müller *Macromolecules* **42** 401 (2009)
COARSE-GRAINED DESCRIPTION OF A BRUSH-MELT INTERFACE IN EQUILIBRIUM AND UNDER FLOW

[156] C. Pastorino, T. Kreer, M. Müller and K. Binder *Phys. Rev. E* **76** 026706 (2007)
COMPARISON OF DISSIPATIVE PARTICLE DYNAMICS AND LANGEVIN THERMOSTATS FOR OUT-OF-EQUILIBRIUM SIMULATIONS OF POLYMERIC SYSTEMS

[157] P.D. Olmsted *Rheol Acta* **47** 283 (2008)
PERSPECTIVES ON SHEAR BANDING IN COMPLEX FLUIDS
and references therein

[158] P. Sollich, F. Lequeux, P. Hébraud and M.E. Cates *Phys. Rev. Lett.* **78** 2020 (1997)
RHEOLOGY OF SOFT GLASSY MATERIALS

[159] P. Coussot, J.S. Raynaud, F. Bertrand, P. Moucheront, J.P. Guilbaud, H.T. Huynh, S. Jarny and D. Lesueur *Phys. Rev. Lett.* **88** 218301 (2002)
COEXISTENCE OF LIQUID AND SOLID PHASES IN FLOWING SOFT-GLASSY MATERIALS

[160] A. Sengupta, S. Sengupta and G.I. Menon *Phys. Rev. B* **75** 180201(R) (2007)
DRIVEN DISORDERED PERIODIC MEDIA WITH AN UNDERLYING STRUCTURAL PHASE TRANSITION
and A. Sengupta, S. Sengupta and G.I. Menon *Phys. Rev. B* **81** 144521 (2010)
DRIVEN DISORDERED POLYMORPHIC SOLIDS: PHASES AND PHASE TRANSITIONS, DYNAMICAL COEXISTENCE AND PEAK EFFECT ANOMALIES

[161] T. Kreer, M.H. Müser, K. Binder and J. Klein *Langmuir* **17** 7804 (2001)
FRICTIONAL DRAG MECHANISMS BETWEEN POLYMER-BEARING SURFACES

[162] O.M. Braun and Y.S. Kivshar *Phys. Rep.* **306** 1 (1998)
NONLINEAR DYNAMICS OF THE FRENKEL-KONTOROVA MODEL

[163] J. Tekic, O.M. Braun and B.B. Hu *Phys. Rev. E* **71** 026104 (2005)
DYNAMIC PHASES IN THE TWO-DIMENSIONAL UNDERDAMPED DRIVEN FRENKEL-KONTOROVA MODEL

[164] G.S. Verhoeven, M. Dienwiebel and J.W.M. Frenken *Phys. Rev. B* **70** 165418 (2004)
MODEL CALCULATIONS OF SUPERLUBRICITY OF GRAPHITE

[165] J.D. Weeks, D. Chandler and H.C, Andersen, J. Chem. Phys. **54**, 5237 (1971)
ROLE OF REPULSIVE FORCES IN DETERMINING EQUILIBRIUM STRUCTURE OF SIMPLE LIQUIDS